Solubility of Triglycerides in Water Using an Extended Surfactant

Dissertation Presented for the Degree

of Doctor of Natural Science

(Dr. rer. nat.)

University of Regensburg

Natural Science Faculty IV

Chemistry and Pharmacy

Angelika Klaus

Regensburg 2011

Official Registration   02.02.2011

Defense: 04.03.2011

Ph. D. Supervisor: Prof. Dr. Werner Kunz

Adjudicators: Prof. Dr. Werner Kunz

                        Prof. Dr. Gordon J. T. Tiddy

                        Prof. Dr. Jörg Daub

Chair: Prof. em. Dr. Dr. h.c. Josef Barthel

Meinen geliebten Eltern

Manfred und Stefanie

Preface

This PhD thesis was carried out at the Institute of Physical and Theoretical Chemistry, Faculty of Natural Science IV, University of Regensburg, between October 2007 and January 2011, under the supervision of Prof. Dr. W. Kunz. This work would not have been possible without the great support from many people. Therefore, I want to express my profound gratitude to the following, who contributed to the completion of my dissertation:

First of all, I would like to express my deepest gratitude to my supervisor, Prof. Dr. W. Kunz, for giving me the opportunity to carry out this thesis at the Institute of Physical and Theoretical Chemistry, for his commitment to guide me through my research, for this interesting subject, the invaluable discussions we shared, and the financial support provided in order to complete my thesis.

My sincere gratification goes to Prof. Dr. Gordon J. T. Tiddy for the countless time he has spent supporting me on this subject. I cannot thank him enough for his expertise, knowledge, and for the many great scientific discussions. His contributions are highly valued and regard with my utmost respect.

Dr. Didier Touraud is gratefully acknowledged for finding this excellent surfactant for me to work with, while supporting me with many experimental ideas.

Special thanks to Dr. George Smith from the Huntsman Corporation (Texas, USA) for providing the extended surfactant whenever it was needed. He has been of great help with his valuable insights to questions concerning the extended surfactants. Without this surfactant, this thesis would not have been possible.

Prof. Dr. Conxita Solans (CSIC, Barcelona, Spain) is gratefully acknowledged for her enlightening thoughts on nano-emulsions, and her tremendous support.

iv

ments throughout the scope of this work.

Furthermore, I am gratefully thankful to Christine Thoms (Maus) for truly being my best friend and a caring person with extraordinary support, both personally and professionally. To Florian Pevny and Dr. Clement Padie, I am delighted and thankful for the company they have both provided me during the numerous lunches filled with endless laughter. Sincere thanks to Dr. Franziska Weichelt for her thoughtfulness and support towards the second half of this thesis.

Of course, to my loving parents, Manfred and Stefanie Klaus, and my brother, Thomas Klaus, for their indescribable support and love they have always given me throughout my lifetime endeavors.

Last, but not least, my sincere gratitude goes to my boyfriend, Peter Suh, for his incredible encouragement and reinforcement not only throughout the progress of this thesis, but ever since the moment I met him. From the bottom of my heart, I thank you.

Contents

Introduction

The solubilization of high amounts of triglycerides in water using only small amounts of additives has been a challenge for scientists for many decades.

In 1948, P.A. Winsor showed that the oil and water solubilization capacity of microemulsion systems can be improved by increasing the surfactant-oil and surfactant-water interactions. An optimum solubilization may be found when the oil and water interactions are equal, which can be achieved by either increasing the hydrophobicity of the surfactant tail or the hydrophilicity of the surfactant head-group.[1] This was confirmed experimentally by J. M. Blakeway in the early 1980th, who introduced the fundamental concept inserting block copolymers in a non-ionic emulsifier to enhance the solubility of fat soluble perfume oils.[2]

The idea of using lipophilic linker molecules, to effectively extend the length of the hydrophobic surfactant tail further into the oil phase without loosing water solubility of the surfactant, was initiated by Graciaa et al. about 17 years ago.[3, 4] Subsequently, to compensate the increased hydrophobicity of the lipophilic linker, the concept of the hydrophilic linker was proposed to further improve the solubilization capacity of such systems.[5–7] The hydrophilic linker adsorbs at the oil-water interface and enhances the surfactant-water interaction. It has been shown that the combination of both hydrophilic and hydrophobic linkers acts as a "pseudo-surfactant". Thereby, the amount of surfactant necessary for oil solubilization in middle phase microemulsions is reduced.[8, 9]

Recently, there has been a growing interest in a new kind of surfactant, which exhibits both lipophilic and hydrophilic linkers. These so-called extended surfactants contain polypropylene oxide or copolymers of polypropylene-polyethylene oxide groups between the alkyl chain and the hydrophilic head-group. These linkers

are groups of intermediate polarity. Due to this unique structure, the surfactant is able to extend the hydrophobic part of the surfactant deeper into the oil phase.[3–5, 10]

During the last decades, many attempts were made to form microemulsions with high amounts of vegetable oils without the addition of an alcohol or a co-oil; however, without success. The reason for these difficulties is the complex structure of the triglyceride molecule. Triglycerides are esters of fatty acids combined with glycerol. The long and bulky alkyl chains lead to a highly hydrophobic molecule, while the ester regions inside the molecule cause high polarity. The combination of both results in a poor solubilization of these substances by surfactants. Therefore, extended surfactants are not only found to fill the gap between conventional anionic and non-ionic surfactants, but are also the most promising candidates to solubilize high amounts of triglycerides or vegetable oils in the continuous aqueous phase of microemulsions, requiring low surfactant concentrations.

Over the last years, several papers have demonstrated the advantages of extended surfactants to enhance the oil solubilization of microemulsions with highly hydrophobic oils, triglycerides, and vegetable oils.[4, 10–13]

The goal of this thesis is to solubilize high amounts of vegetable oils in water with low concentrations of additives. The desired oil to surfactant ratio is of 2:1. Therefore, the extended surfactant X-AES, containing a C_{12-14} alkyl chain, an average of 16 propylene oxide groups, an average of two ethylene oxide groups and a sulfate head group (C_{12-14}-$(PO)_{16}$-$(EO)_2$-SO_4Na), is chosen. Due to its exceptional structure and the properties of extended surfactants described previously, this surfactant is the most promising candidate to accomplish the difficult task.

First, the binary surfactant-water system will be discussed over the whole concentration range (Section 3.1). At the beginning of this thesis, only limited information about the properties of extended surfactants and their behavior in water was available in literature. Such characteristics are CMC values, the optimum salinity and the optimum interfacial tension, or cloud point measurements. All the mentioned parameters are relevant for the formation of microemulsions with highly hydropho-

bic oils, triglycerides, or vegetable oil. However, the phase behavior of an extended surfactant in water was never studied in detail before; although it is of high importance to understand the phase transition mechanism required for the solubilization of triglycerides in water.

Secondly, the influence of electrolytes on the phase behavior of the chosen extended surfactant in water will be presented (Section 3.2). A specific feature of an extended surfactant with an anionic head-group in aqueous solution is the appearance of a cloud point. This cloud point decreases with decreasing number of propylene oxide groups.[10] However, adding various electrolytes to the surfactant-water mixture can change the cloud point of the solution drastically. Depending on the salt, it may be decreased or increased. A more detailed description of the effect of salts on surfactant solutions is given in Section 1.5.

Finally, the effect of different salts on the phase behavior of a mixture containing the extended surfactant X-AES, a hydrotrope (sodium xylene sulfonate, SXS), rapeseed oil, and water will be examined. The obtained information is then used to constantly increase the amount of oil to obtain the optimum formulation (Section 3.3 and 3.4). Different studies ranging from phase diagram determination, various scattering methods, nuclear magnetic resonance, or imaging techniques are performed to maximize the information about the systems studied, their structures (size and shape), and the mechanism of the phase transitions.

Chapter 1

Fundamentals

1.1 Surfactants

1.1.1 General Aspects

The term surfactant is a blend for **surf**ace **act**ive **a**ge**nt** which literally means active at the surface. Surfactants are amphiphiles, which derives from the Greek word amphi ("both", "double", or "from both sides") and the word philos ("friendship" or "affinity"). Amphiphilic molecules consist of at least two parts, a hydrophobic (tail) and a hydrophilic group (head) (Figure 1.1).

Hydrophilic
head-group
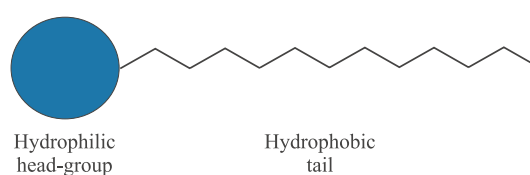
Hydrophobic
tail

Figure 1.1: Surfactant molecule monomer.

Thus, a surfactant molecule contains both a water soluble and a water insoluble component. When dissolved in water, the insoluble hydrophobic group extends out of the bulk water phase, either into the air or, if mixed with oil, into the oil phase. The water soluble head-group, on the other hand, remains in the water phase. The driving force for a surfactant molecule to adsorb at the interface is to lower the free energy of the phase boundary.[14–17]

1.1.2   Classification of Surfactants

Surfactants are primary classified by the charge of the polar head-group, which can be anionic, cationic, non-ionic, or zwitterionic. Furthermore, the hydrophobic part of the molecule can be linear or branched and generally has an alkyl chain length in the range of 8-18 carbon atoms. The degree of chain branching, the length of the chain, and the position and nature of the polar head-group are all parameters, which affect the physicochemical properties of the surfactant.[14–16]
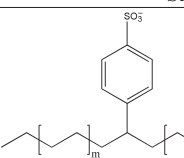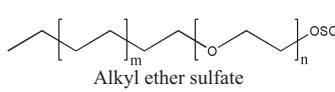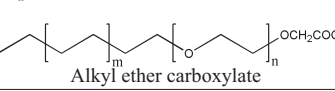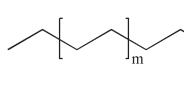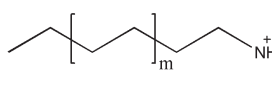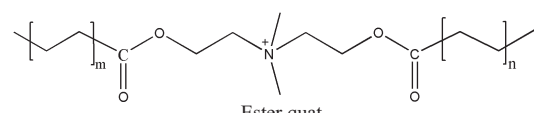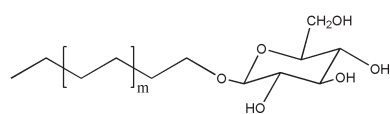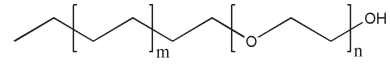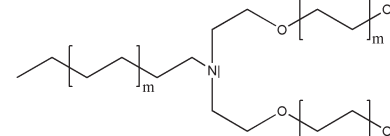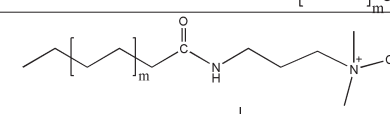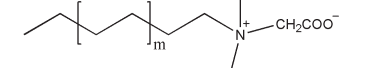
Surfactant class	Structure examples
Anionic Surfactants	Alkyl ether sulfate Alkylbenzene sulfonate Alkyl ether carboxylate
Cationic Surfactants	Alkyl quat Fatty amine salt Ester quat
Non-ionic Surfactants	Alkyl glycoside Fatty alcohol ethoxylate Fatty amine ethoxylate
Zwitterionic Surfactants	Amidobetaine Betaine

Figure 1.2: Examples of structures of some representative surfactants for each class.

Anionic Surfactants

As the name implies, anionic surfactants consist of an anionic head-group, e.g. a sulfate, a sulphonate, a carboxylate, or a phosphate (Figure 1.2). The counterion is usually a quaternary ammonium group or an alkaline metal, like sodium or potassium. Anionic amphiphiles are the most commonly used surfactants. The main reasons for their popularity are the simpleness and the low costs of manufacture. They are mainly used for detergent formulations, such as in laundry products, dish washing liquids, shampoos, etc.[14–16]

Non-Ionic Surfactants

Non-ionic surfactants are the second-largest used class of surfactants. The surfactant head-group bears neither a positive nor a negative charge. The vast majority of non-ionic surfactants consist of a polyether with oxyethylene (EO) units as polar head-group obtained by the polymerization of ethylene oxide (Figure 1.2). A typical number of oxyethylene groups is between three and ten (some surfactants often possess much more oxyethylene units). Non-ionic surfactants are often used for powder or liquid detergents and their application can be found in a wide industrial field.[14–16]

A characteristic feature of non-ionic surfactants in aqueous solution is the phase separation with increasing temperature. This temperature is referred to as the "cloud point" or "cloud temperature". In a temperature-concentration phase diagram of a non-ionic surfactant in water it may also be described as the lower consolute temperature.[14, 18, 19] The cloud point depends strongly on the hydrophobic chain length and the number of oxyethylene groups. The oxygen atoms of the oxyethylene (EO) chain establish hydrogen bonds with the water molecules, resulting in a high water solubility of the EO groups. However, hydrogen bonding is a temperature sensitive phenomenon and thus, at the cloud point the degree of hydration of the hydrophilic surfactant part is just insufficient to solubilize the remaining alkyl chain. The surfactant is no longer entirely soluble in water at this temperature and phase separation into a surfactant-rich and a surfactant-poor phase occurs.[14] This

phenomenon can be strongly influenced by the addition of various additives to the aqueous surfactant solution, which will be described in detail in Section 1.5.[20, 21] In addition, a cloud point can also be observed for anionic, cationic, or zwitterionic surfactants, if the electrostatic interactions are screened or when the surfactant contains oxyethylene groups.[22–24]

Cationic Surfactants

Cationic surfactants usually contain a positive charged nitrogen atom. Amines as well as quaternary ammonium-based surfactants are common (Figure 1.2). However, amines only function as a surfactant in the protonated state and therefore, are pH sensitive. In contrary, quaternary ammonium groups (so-called "quats") do not depend on the pH. Cationic surfactants usually have a counterion of the halogen type, like chloride or bromide. Due to difficulties in synthesis, cationic surfactants are generally more expensive than anionic surfactants. These kind of amphiphiles are the third-largest used surfactant class and usually utilized for fabric softeners, in laundry detergents (mostly to improve the packing of the anionic surfactant molecules), or in all-purpose household cleaners (due to their property of being disinfectant).[14–16]

Zwitterionic Surfactants

These surfactants exhibit both a cationic and an anionic charge (Figure 1.2). The cationic part is mostly an ammonium group, whereas the anionic part may vary (e.g. carboxylate, sulfate, or sulfonate). These surfactants are strongly pH dependent, which affects their properties. Due to their high price, they are the smallest class of surfactants that are used in the industry. These kinds of surfactants are very mild, show very low eye and skin irritation and consequently, are often used for formulations of shampoos and personal care products.[14–16]

In addition, several new classes of surfactants have been reported in the literature, such as polymeric surfactants or surface active polymers. These amphiphiles will not be discussed in detail in this work and the interested reader is referred to

the following references [14–17]. However, extended surfactants will be discussed in detail below, since these class of amphiphiles built the main part of this thesis.

Extended Surfactants

In 1948, it was already shown by P. A. Winsor that the oil and water solubilization capacity of a microemulsion can be improved by increasing the surfactant-oil and surfactant-water interaction. Furthermore, it is possible to have both a micellar or reverse micellar solution with low viscosity containing high amounts of oil or water.[1] An optimum solubilization can be found when the oil and water interactions are equal. There are two possibilities to effectively enhance the oil and water interactions by either increasing the hydrophilicity of the head-group or the hydrophobicity of the tail group of a surfactant. In the early 1980th, J.M. Blakeway had the idea of inserting block copolymers in a non-ionic emulsifier to enhance the solubility of fat soluble perfume oils.[2]
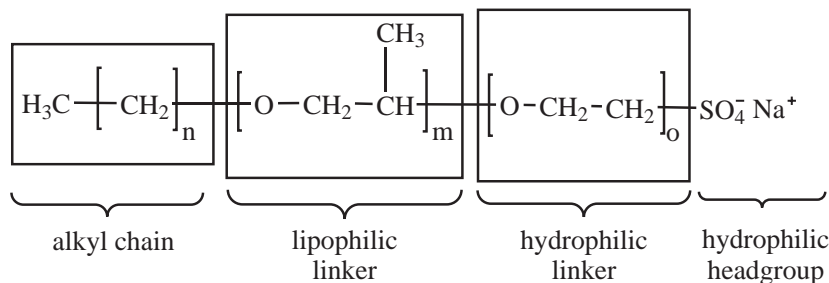
Figure 1.3: Typical structure of an anionic extended surfactant with a sulfate head-group.

Recently, there has been increased interest in a new kind of surfactant class, so-called extended surfactants. These amphiphiles contain intermediate polarity groups, such as polypropylene oxide or polypropylene-polyethylene oxide, between the hydrophobic alkyl chain and the hydrophilic head-group.[4] These intermediate groups are called linker. The idea of using lipophilic linker molecules to effectively extend the length of the hydrophobic tail into the oil phase without loosing water solubility of the surfactant was initiated by Graciaa *et al.* about 17 years ago.[3, 5] Studies by Miñana-Perez *et al.*,[10] Salager *et al.*,[3–5, 10] and Witthayapanyanon

et al. [25–27] showed that the presence of a very lipophilic amphiphilic additive improves the solubilization of oils substantially. However, depending on the oil and on the nature of the linker, a proper length of the lipophilic linker is necessary.[11, 28–30] This lipophilic linker is a hydrocarbon chain with a relatively small polar group. It is able to extend the hydrophobic part of the surfactant deeper in the oil phase near the interface.

These extended surfactants (Figure 1.3), alkyl-polypropylene-oxide ether sulfates, are found to fill the gap between conventional anionic and non-ionic surfactants and are the most promising candidates to solubilize a high content of vegetable oil in the continuous aqueous phase of microemulsions.

Salager has suggested that the polypropylene-oxide group (PO) forms an intermediate zone between the hydrocarbon and aqueous regions, which has a thickness of approximately 40-50 Å. In comparison to a dodecyl chain length of 15-25 Å, this is a significant extension. It needs to be mentioned that the polyethylene oxide groups (EO) are usually inserted to facilitate the final sulfonation, which cannot be carried out on the propylene oxide end.[10]

Some characterization of extended surfactants has been reported by Witthayapanyanon *et al.*, who determined the optimum salinity (S^*) [10] and the optimum dynamic interfacial tension (IFT^*) with various kinds of oils.[25] Salager *et al.* were the first to examine the solubilization of various oils in water using extended surfactants.[10, 25, 26] Cloud point measurements on 10 wt% surfactant solutions were also performed by Salager *et al.*, where the cloud point decreases with increasing PO content. Note that polyoxyethylene non-ionic surfactants exhibit cloud points where a (more concentrated) micellar solution coexists with a very dilute aqueous solution above a critical temperature. It is very rare for such a phenomenon to occur with ionic surfactants in the absence of added inorganic electrolyte.[4, 10] To rationalize the research for microemulsions, Salager *et al.* have developed the hydrophilic-lipophilic deviation (HLD) method.[31, 32] The key parameters are σ and σ/K; σ relates to the hydrophobicity of the surfactant tail and is called the surfactant characteristic parameter, while σ/K is a parameter that depends on the hydrophilicity of the surfactant head-group. Witthayapanyanon *et al.* have reported

a substantial body of research on this method for microemulsion formation with extended surfactants, where σ and σ/K were determined.[26] All the experiments were aimed at obtaining an optimum formulation of oils in water.[4, 10–13, 25, 27, 33]

1.1.3 Surfactant Self-Assembly

A) Low Surfactant Concentrations - Surfactant Micellization

a) Critical Micellar Concentration

Surfactant self-assembly leads to a large range of different structures. At very low concentrations, for example, surfactant monomers exist in an aqueous solution. These monomers adsorb at the air-water interface with the hydrophobic groups extending out into the air and the hydrophilic head-group inside the aqueous solution. Once the air-water interface is covered with monomers, the surfactant molecules start to form aggregates called micelles. These micelles appear at a well-defined concentration, which is known as the critical micellar concentration (CMC) and is the most important characteristic of a surfactant. The critical micellar concentration can be measured, for example, by surface tension. However, a very large number of physicochemical properties are also sensitive to the surfactant micellization, and a few examples are shown in Figure 1.4.[14–17]
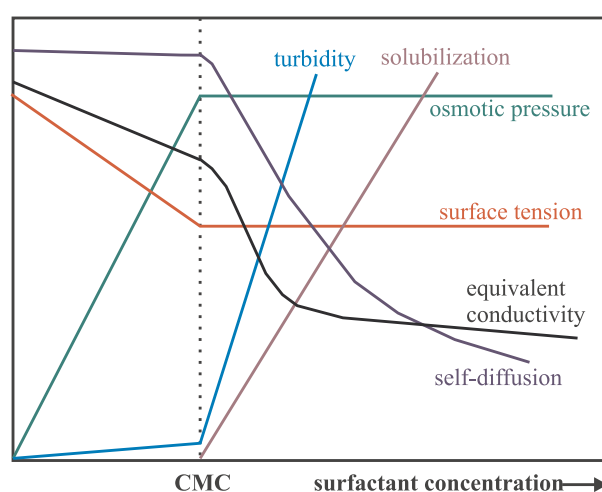
Figure 1.4: Schematic representation of the concentration dependence of some physical properties for solutions of a micelle-forming surfactant.
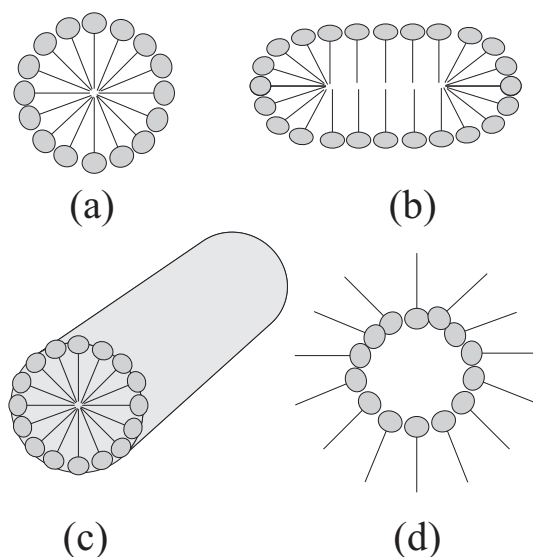
Figure 1.5: Surfactant self-assembly: (a) normal spherical micelles; (b) disc-like micelles; (c) rod-like micelles; (d) reverse micelles.

Micelles usually have a large, but finite lifetime with a monomer-micelle exchange rate of 10^3-10^6 s and micelle breakdown/formation rates between 10^{-1}-10^2 s.[17] A micelle is a very mobile and disordered aggregate because of a rapid and continuous exchange of the monomers with the bulk solution. It consists of at least 10-20 monomers. However, depending on the surfactant, its structure, and the temperature, the aggregation number (the number of molecules presented in a micelle) can be larger, for example between 50 and 100 for SDS (sodium dodecyl sulfate) and $C_{12}(EO)_8$ (octaethyleneglycoldodecyl ether), respectively. In the case of a polar solvent as continuous phase, normal micelles are formed with their head-groups in the polar region and the tails inside the micelle core (Figure 1.5a). In contrary, reverse micelles arise in non-polar solutions with the head-groups inside the micelle core and the tails extending into the hydrophobic solution (Figure 1.5d).[14–17]

The CMC of a surfactant depends strongly on the nature and the purity of the surfactant. Even the slightest amount of impurities can change the properties of the surfactant and hence, the measured CMC value. The addition of one CH_2 group to the alkyl chain decreases the CMC by a factor of two for ionic and by a factor of three for non-ionic surfactants. Furthermore, the CMC of non-ionic surfactants is much lower than the corresponding one for ionic surfactants and increases slightly

with increasing polar head-group (increasing ethylene oxide number). Cationic surfactants usually have a slightly higher CMC than anionic surfactants. Additionally, the valency of the head-group is significant for the CMC. Monovalent inorganic counterions give approximately the same CMC values, while increasing the valency to two gives a reduction of the CMC by roughly a factor of four.[14–17]

b) The Hydrophobic Effect

Micelle formation arises from the hydrophobic effect, which describes the interaction between a non-polar solute and water. Introducing a hydrocarbon in water at ambient temperatures is always associated with negative entropy and an enthalpy of about zero. This results in a large and positive free energy. The first contribution arises from the "ordering" of the water molecules around the solute. Water molecules, which are next to a non-polar solute (vicinal water), cannot establish hydrogen bonds to the solute. Hence, they have fewer conformations available than "free" water molecules. This effect is associated with a negative entropy. Furthermore, it provides a negative enthalpy because the vicinal water molecules establish stronger hydrogen bonds to the "free" water.

On the other hand, the hydrophobic effect arises from the energy, which is necessary to form a cavity into the water. This cavity needs to be large enough to accommodate the non-polar solute, which then starts to aggregate. The required energy for this contribution is large due to the high cohesion in water arising from the hydrogen-bonding connectivity on the one hand and the small size of water molecules compared to, e.g. alkanes on the other hand. Thus, an important consequence is that the magnitude of the hydrophobic effect is proportional to the area of hydrophobic contact between the water and the solute.[17, 34–36]

c) Micellar Shape for Liquid Crystal Formation

The shape of the micelles provides information about the different liquid crystalline phases formed. Therefore, the packing constraint concept was developed,[17, 37, 38] which gives information about the three major types of micelle shape (spheres, rods, and discs). A simple description of the relationship between the micelle and the

molecular shape is given by this theory. The most important molecular parameters, necessary for this concept, are the volume (v) of the alkyl chain, the cross-sectional area (a) of the surfactant molecule and the maximum length of the alkyl chain (the all-trans length, l_t). For a spherical micelle with a hydrophobic core volume V_{mic}, a radius r, and a surface area A_{mic}, the aggregation number N_s can be expressed as:

$$N_s = \frac{A_{mic}}{a} = \frac{4\pi r^2}{a}; \qquad (1.1)$$

$$N_s = \frac{V_{mic}}{v} = \frac{\frac{4}{3}\pi r^3}{v}. \qquad (1.2)$$

Furthermore, the aggregation numbers must be equal and the following relationship is obtained:

$$a = 3\frac{v}{r}(sphere). \qquad (1.3)$$

The same considerations are made for rod-like and disc-like shapes resulting in:

$$a = 2\frac{v}{r}(rod); \qquad (1.4)$$

$$a = \frac{v}{r}(disc). \qquad (1.5)$$

However, as the radius r cannot be larger than l_t the lowest possible value of a is given by:

$$a = 3\frac{v}{l_t}(sphere); \qquad (1.6)$$

$$a = 2\frac{v}{l_t}(rod); \qquad (1.7)$$

$$a = \frac{v}{l_t}(disc). \qquad (1.8)$$

Depending on the alkyl chain length and the size of the head-group, a surfactant can pack into spheres, rods, or discs (Figure 1.5). Surfactants with large head-groups usually form spherical micelles, smaller head-groups give rod-like micelles and even smaller head-groups rather form discs. Furthermore, entropy prefers the formation of the smallest possible aggregates and thus, spheres over rods and rods over discs. Due

to the fact that both the length and the volume increase by a constant increment, an increase in the length of the alkyl chain should not change the shape of the micelle. However, it is often observed that short-chain surfactants form spheres, while longer-chain surfactants form rod-like micelles. This probably arises from the influence of surface roughness on micelle shape and aggregation numbers.

B) Higher Surfactant Concentrations - Surfactant Liquid Crystals

With increasing surfactant concentration liquid crystal phases may be formed.[14, 17] At a certain concentration of the amphiphile the disordered micellar solution forms an ordered state, if the surfactant is sufficiently soluble. Starting from the micellar shape, which strongly depends on the properties of the surfactant, various liquid crystalline phases can be found. Therefore, micelles are the building blocks of most self-assembly structures. A general scheme for the formation is given as followed:[17]

Small polar head-group: disc-like micelles → lamellar phase

Medium polar head-group: rod-like micelles → hexagonal phase → (V_1/intermediate phase) → lamellar phase

Large polar head-group: spherical micelles → cubic phase → hexagonal phase → (V_1/intermediate phase) → lamellar phase

Liquid crystals (LC) are a state of matter with properties between those of solid crystals and those of liquids. For instance, a liquid crystal may be low viscous (as a liquid), while its molecules may be oriented like in a solid. There are various types of LC phases, which can be distinguished by their different optical properties (such as birefringence).[39, 40]

Liquid crystals can be divided into two main subclasses, thermotropic and lyotropic. Thermotropic samples exhibit liquid crystal phase transitions within a pure substance as the temperature is changed. Lyotropic samples on the other hand, exhibit liquid crystalline phase transition as a function of temperature and concentration. Figure 1.6 shows all possible mesophases, which can appear with increasing surfactant concentration in water as a function of temperature.
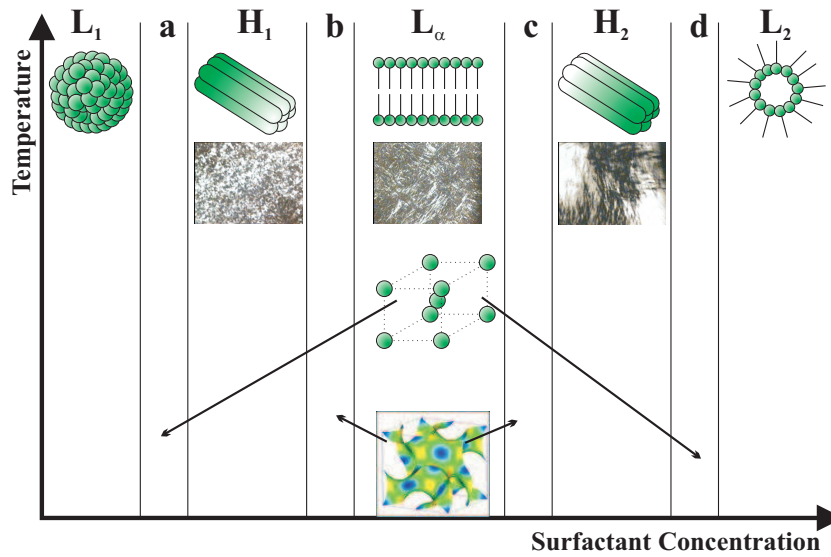
Figure 1.6:   Schematic phase diagram of a binary surfactant-water system.   The following mesophases can be observed: a micellar solution L_1, a hexagonal phase H_1, a lamellar phase L_α, a reverse hexagonal phase H_2, and a reverse micellar solution L_2. a-d can be cubic phases, with a and d being I phases and b and c V phases.

a) Lamellar Phase (L_α)

The lamellar phase (L_α), which is also known as the neat (soap) phase, is the most common mesophase. It is build up of bilayers of surfactant molecules alternating with water layers. The thickness of the bilayer can vary between 1.0-1.9 times of the all-trans length, depending on the surfactant head-group area. The thickness of the water layers on the other hand, can vary over wide ranges, which also depends on the surfactant. In addition, the L_α phase exhibits a quite low viscosity.

This mesophase can be determined using a wide range of different methods. For example, characteristic optical textures, such as "oily streaks" or "Maltese crosses", are observed under a polarizing optical microscope (see Figure 1.6).[39, 40] Due to the alternating structure of the layers, sharp reflections are obtained when small angle scattering is applied. However, more information about the characterization will be given in Section 1.6. A schematic representation of a lamellar phase and its possible position in a phase diagram is given in Figure 1.6.[14, 17, 41, 42]

b) Hexagonal Phases (H_1, H_2)

The hexagonal phase (H) is built up of rod-like micelles, which are arranged in infinite long circular aggregates packed in a hexagonal lattice. Each rod-like micelle is surrounded by six other micelles (Figure 1.6). The radius of the cross-section is in the same order of magnitude as the all-trans alkyl chain length. Two kinds of hexagonal phases exist, the "normal" (H_1) and the "reverse" (H_2) phase. The H_1 phase is water continuous (also known as the "middle" (soap) phase) and the H_2 phase is alkyl-chain-continuous.

Due to the distinct optical textures of the hexagonal phase (normal and reverse) in comparison to the lamellar phase, optical microscopy can be used again for the analysis (Figure 1.6).[39, 40] Also, small angle scattering methods are common to determine the hexagonal phase and a more detailed description will be given in Section 1.6. Both hexagonal phases (H_1 and H_2) exhibit a higher viscosity than the lamellar phase.[14, 17, 41, 42]

c) Cubic Phases (I_1, I_2, V_1, V_2)

Cubic phases are optically isotropic and highly viscous mesophases, with many different locations in the phase diagram (Figure 1.6). The structures formed are based on one of many possible cubic lattices (the primitive, face-centered, or body-centered). There exist phases labeled with an "I" located between a hexagonal phase and a micellar solution (discrete cubic phase, normal and reverse, I_1 and I_2, a and d in Figure 1.6), which consist of small spherical micelles. In addition, bicontinuous structures can occur where the surfactant molecules form aggregates, which consist of a porous connected structure in three dimensions. These phases are labeled with a "V" and are located between the lamellar and the hexagonal phase (also normal and reverse, V_1 and V_2, b and c in Figure 1.6). The cubic phases can be characterized by means of small angle X-ray scattering. Depending on the structure of the cubic phases, the reflections appear in different ratios (which will be described in Section 1.6). Due to its isotropy, it is difficult to detect cubic phases by optical microscopy. However, air bubbles within a cubic phase appear asymmetric under the microscope

and are an indication for the high viscosity of the cubic phase.[14, 17, 41–47]

In addition, more mesophases can occur known as gel phases (L_β), nematic phases, or intermediate phases, which are discussed in detail elsewhere.[14, 17]

1.2   Surface Active Additives

1.2.1   Hydrotropes

Hydrotropes are mild compounds similar to surfactants consisting of a hydrophilic and a hydrophobic part. The hydrophobic part is generally very small/short, which results in a high water solubility of these molecules. However, it is too small to cause self-aggregation and therefore, no CMC can be found as for surfactant molecules. Hydrotropes usually are short-chain non-ionics ($C_x EO_y$) or consist of two essential parts, an anionic (head) group and a hydrophobic (aromatic) ring system. Typical examples for hydrotropes are sodium xylene sulfonate (SXS), sodium cumene sulfonate (SCS), sodium benzoate, sodium salicyate, or sodium p-toluenesulfonate (Figure 1.7).[48, 49] Also, cationic and non-ionic (aromatic) hydrotropes can be found.
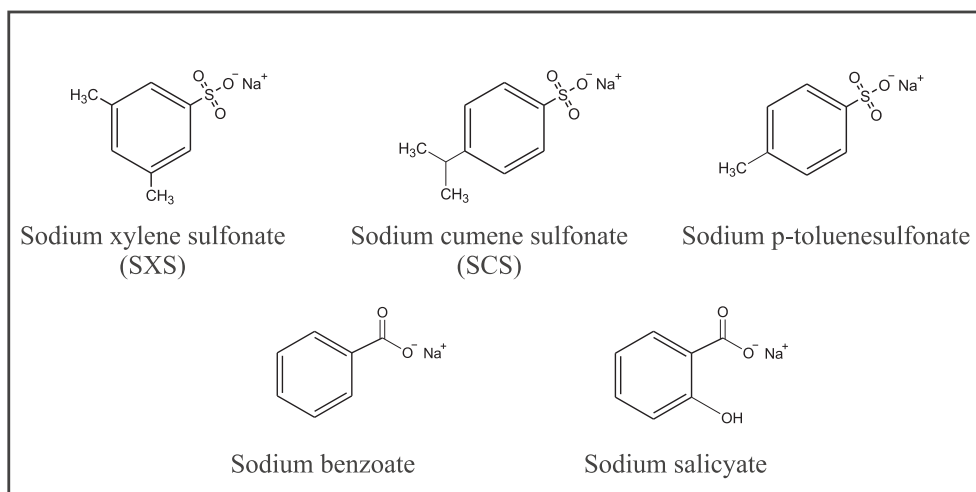
Figure 1.7: Structures of different hydrotropes.

The term *hydrotropy*, originated by Neuberg in 1916, describes an increase in solubility of a sparingly soluble compound in aqueous solution.[50] However, not only the solubility behavior (e.g. cloud point) is changed in presence of hydrotropes, but also the micellar characteristics (like CMC, aggregation number) as well as the adsorption at the interface for a surface active agent can be altered.[17, 49, 51] Several mechanism have been proposed to explain the effect of hydrotropes. One hypothesis describes the formation of a "complex" with the solute (e.g. the surfactant), resulting in a higher aqueous solubility. Another mechanism suggests that hydrotropes behave as a "salting-in" additive, which will be explained in Section 1.5.[17, 52, 53] Hydrotropes are well known to avoid the formation of liquid crystalline phases, resulting from their ability to decrease the surfactant-surfactant interaction.[54] Hydrotropes find applications in many industrial fields, such as in separation processes or to increase the cloud points of detergent solutions.[17, 49]

1.2.2 Co-Surfactants

Co-surfactants are also molecules that are similar to surfactants. However, they are insufficiently hydrophilic to form micelles or to self-aggregate in aqueous solution. It is well known that co-surfactants participate between the surfactant molecules inside the micelles. This partitioning strongly depends on the strength of the co-surfactant head-group. Weakly polar groups, for example, can occupy the micelle interior or stay at the surface of the micelle. Thus, they can affect the curvature of the micelle and the internal energy. The short hydrophobic alkyl chain and the hydrophilic head-group enhance the interaction between the surfactant monolayers at the interface. Usually, low molecular weight alcohols or short chain amphiphiles are used as co-surfactants. These molecules are often utilized for the formation of microemulsions to reduce the amount of surfactant.[14–17, 55]

1.3 Natural Fats and Oils

Most natural fats and oils from vegetable and animal sources are well recognized as essential nutrients in human diet. These substances supply energy, provide essential
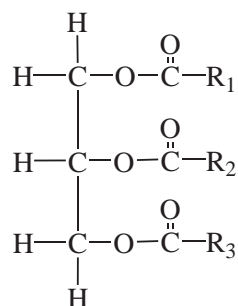
Figure 1.8: Structure of a triglyceride consisting of a glycerol and three fatty acids (R$_1$-R$_3$).

fatty acids, support structural aspects of the body, and serve as carriers of oil soluble vitamins. Natural oils and fats are mainly constructed by building blocks, which are called triglycerides (or triacylglycerol, triacylglyceride). Triglycerides are triesters of one glycerol with three fatty acids (Figure 1.8).[56, 57]

The chain length of the fatty acids can vary; however, the most common lengths are 16, 18, or 20 carbon atoms. Natural fatty acids found in plants or animals are typically composed of even numbers of carbon atoms, which is due to the way these molecules are bio-synthesized. According to their degree of saturation fatty acids can generally be classified in three main groups - saturated, monounsaturated, and polyunsaturated fatty acids. Depending on the proportion and the position of the fatty acid in the glycerol molecule, the physical and chemical properties of the oils can be influenced. The most common fatty acids in triglycerides are palmitic acid (C16:0, the first number gives the amount of carbon atoms in a fatty acid and the second number the degree of un-saturation), stearic acid (C18:0), oleic acid (C18:1), linoleic acid (C18:2), and linolenic acid (C18:3). The structures are shown in Figure 1.9.[58–60]

In addition, fatty acids like capric acid (C10:0), lauric acid (C12:0), or myristic acid (C14:0) can also be found. Fatty acids in the range of 12-18 carbon atoms, and especially those from natural origin, are important for the manufacture of soaps and personal care products.

Incomplete esterification of the glycerol can lead to mono- or diglycerides. These molecules occur naturally in crude animal fats and vegetable oils. However, mono-glycerides are present in much lower quantities than diglycerides and are often used
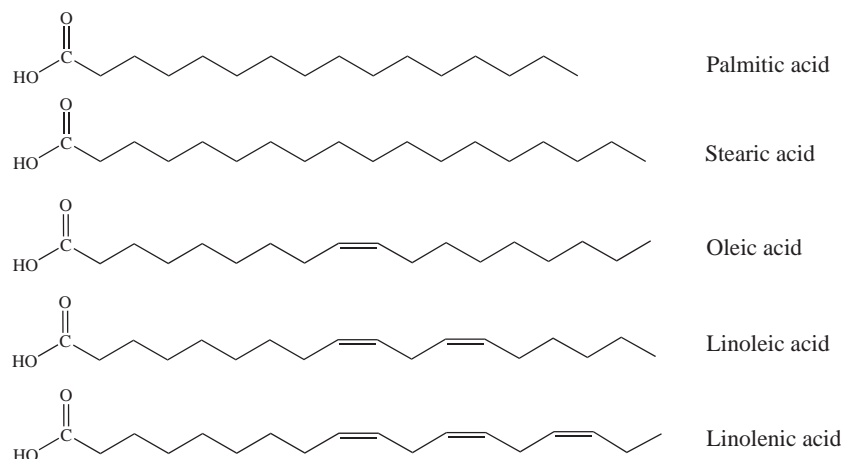
Figure 1.9: Structures of the most common fatty acids found in triglycerides.

as emulsifiers.[61]

Vegetable oils are very hydrophobic, room-temperature liquid substances, and as the name implies, are originated from plants (e.g. corn, soy, peanut, or rapeseed). The relatively low melting point arises from the degree of unsaturation; the more unsaturated the fatty acids the lower the melting point. Rapeseed oil, for example, is a light yellow to brownish liquid and is one of the most important edible vegetable oils. It mainly consists of oleic acid (50-70%), linoleic acid (15-25%), and linolenic acid (5-15%). In addition, fatty acids like palmitic acid, stearic acid, gadoleic acid (20:1), and erucic acid (22:1) can be found.[59, 62, 63]

Vegetable oils and their derivatives are renewable, biodegradable substances, a good replacement for petroleum-based ingredients, and less harmful to the environment as compared to mineral oil.[58, 64–66] It is well known that it is more difficult to solubilize triglycerides into microemulsions than hydrocarbons or alkyl mono-esters.[64] This is due to the very complex structure of the triglycerides. It was shown by Xenakis *et al.* that vegetable oils containing unsaturated fatty acids present a local structural organization forming a "backbone" of a few nanometers. He suggested that bulk edible oils contain small quantities of water as well as a variety of water soluble and polar surface active minor components. In addition, he postulated a colloidal structure of the oil from both experimental and theoretical insights.[61]

Today, it is still a challenge to solubilize high amounts of vegetable oils in water; although, a lot of work has been done in this field.[4, 10, 11, 13, 27, 67–70] Triglyc-

eride based microemulsions are used in many applications such as in pharmaceutics, cosmetics, detergency, or agrochemical formulations.

1.4   Emulsions

1.4.1   General Aspects

A mixture of two or more immiscible components is called an emulsion. These systems consist of a dispersed and a continuous phase and a boundary between these two phases (the interface). Without the addition of an amphiphile, emulsions appear turbid (or white) due to the large droplets scattering the light that passes through the sample. Emulsions are very unstable systems and do not form spontaneously. Energy, like shaking, stirring, or heating, is required to initially form the emulsion. To increase the stability of water-oil mixtures, emulsifiers (e.g. surfactants) are usually added to the solutions. The amphiphiles adsorb at the interface, resulting in a drastic change of the characteristics of the interfaces. Oil-in-water (O/W) or water-in-oil (W/O) emulsions may be formed, depending on which phase is the continuous phase.

There are five terms describing the instability process of an emulsion, which are breaking, coalescence, creaming, Ostwald ripening, and flocculation. A schematic representation of all four terms is given in Figure 1.10.[55, 71–73]

Additionally to an amphiphile, other substances can be added to the solution to effectively increase the stability of the system. Such additives can be electrolytes, polymers, particles, or co-surfactants. These molecules adsorb also at the interface, as emulsifiers or surfactants do, and increase the stability of the system. Depending on the way of preparation and the compounds added to the emulsion, solutions can be obtained with a stability of days, months, or even years. Emulsions are well known for many decades in daily products, such as milk, vinaigrette, several cosmetic, or food products. Furthermore, emulsions are interesting for a lot of applications like in the chemical, pharmaceutical, or medical field.[55, 74]

In addition, multiple emulsions exist, which are composed of droplets of one liquid
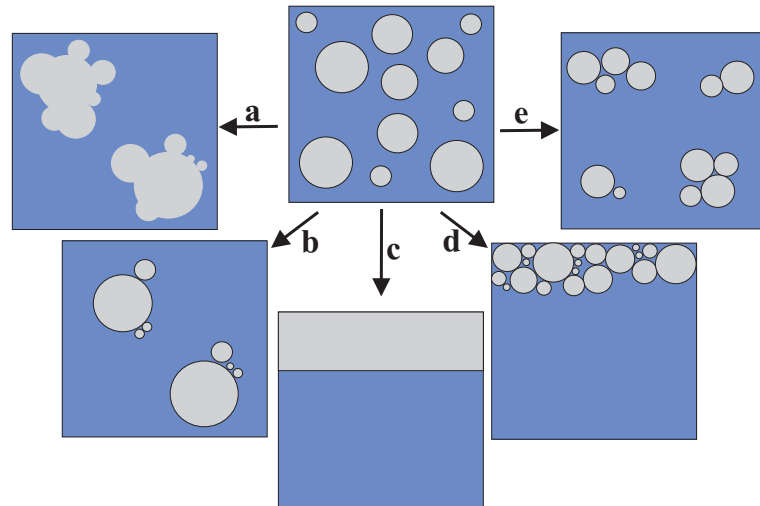
Figure 1.10: Emulsion instability can arise from (a) coalescence, (b) Ostwald ripening, (c) breaking of the emulsion, (d) creaming, (e) flocculation, .

dispersed in a larger droplet of a second liquid and finally dispersed in a continuous phase (consisting of the first liquid, Figure 1.11). Such systems can consist of W/O/W (water-in-oil-in-water) dispersions or O/W/O (oil-in-water-in-oil). Even higher multiplicities are possible, like O/W/O/W systems. However, because multiple emulsions have a variety of phases and interfaces, they appear even more unstable than common emulsions.[55, 75–77]
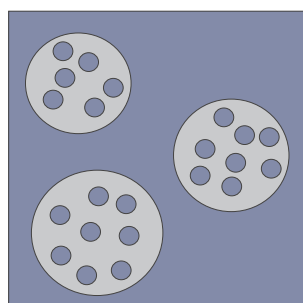
Figure 1.11: Example for a multiple emulsion consisting of water (blue) and oil (light grey).

Due to their unique structure, multiple emulsions are of practical interest for potential applications in drug delivery, emergency drug overdose treatment, wastewater treatment, and separation technology.[55, 71, 72]

1.4.2   Nano-Emulsions

Emulsions with a droplet size between 20 and 200 nm are often referred to as nano-emulsions, mini-emulsions, or ultrafine emulsions. Due to the characteristic size of the droplets, nano-emulsions appear transparent or translucent.[78–80] They usually possess stability against sedimentation or creaming due to the Brownian motion and thus, the diffusion rates are higher than the sedimentation (or creaming) rates induced by the gravity force. These properties make nano-emulsions of interest for a lot of fundamental studies and industrial applications, such as in the chemical, pharmaceutical, or food technology field. O/W and W/O nano-emulsions have been investigated over the last years and reviewed thoroughly.[78–85]

Nano-emulsions are non-equilibrium systems (thermodynamically unstable) with high kinetic stability. Consequently, these emulsions are not formed spontaneously and thus, energy input is required. Furthermore, they tend to phase separate into the continuous phases.

The phase inversion temperature (PIT) method introduced by Shinoda and Saito [86] is the most common method for the preparation of nano-emulsions. It is based on the solubility changes of oxyethylene (EO) surfactants as a function of temperature. Due to the dehydration of the EO group, these surfactants become more hydrophobic with increasing temperature (the mechanism was already described for non-ionic surfactants in Section 1.1.2). Usually, an oil swollen solution (O/W) coexisting with excess oil is observed at low temperatures, while a water swollen reverse solution (W/O) with excess water is observed at higher temperatures (arising from the change in curvature with increasing temperature). At intermediate temperatures the curvature becomes almost zero and a bicontinuous or lamellar structure (with both excess water and oil) is obtained. The PIT emulsification method takes advantage of the extremely low interfacial tensions achieved at this intermediate temperature. By heating and cooling the system rapidly, kinetically stable emulsions with very small droplet sizes can be obtained.[78, 86, 87]

The destabilization of nano-emulsions is mainly driven by Ostwald ripening or molecular diffusion. These effects arise from the polydispersity and the difference in solubility between the small and larger droplets. However, nano-emulsions can remain

stable for several hours, days, or even years, depending on their preparation and the droplet size.[78, 79]

1.4.3 Microemulsions

The first microemulsions were described in 1948 by Hoar and Schulman.[88] It was also Schulman, who introduced the term microemulsion.[89] However, a more recent definition for these kinds of solutions was given by Daniellsson and Lindmann.[90] Microemulsions are, in contrary to emulsions or nano-emulsions, thermodynamically stable and usually formed spontaneously (without any energy input required). They appear as an isotropic transparent mixture of at least three components (hydrophile, hydrophobe and an amphiphile) with an approximate radius between 2-20 nm. Depending on the volume fraction, O/W (low oil volume) and W/O (high oil volume) microemulsions are possible structures, as described for (nano-)emulsions. The micelles can exhibit different shapes, like spheres, discs, rods, or a bicontinuous structure.[14, 17, 91–93]

Winsor introduced in 1948 four types of possible equilibria found for a water-oil-surfactant (+ co-surfactant) system and a schematic representation is given in Figure 1.12. A Winsor I phase describes a two phase region of an aqueous micellar system (bottom phase) in equilibrium with an almost pure oil phase (top phase). Winsor II is the contrary to Winsor I with an oil continuous micellar system (top phase) in equilibrium with almost pure water phase (bottom phase). The third equilibrium, Winsor III, is a three phase system consisting of an almost pure water (bottom) and oil (top) phase in equilibrium with a surfactant-rich middle phase. The last type, Winsor IV, is a single phase of water, oil, and surfactant describing a normal, a reverse, or a bicontinuous microemulsion.[1]

 Due to their excellent properties, like high capacity to solubilize water and oil, low interfacial tension, and spontaneous formation, microemulsions are desirable in numerous applications, including cosmetics, food technology, drug delivery systems, soil remediation, or cleaning technology. However, the disadvantage is that much surfactant is required for the formation of microemulsions.

Microemulsion systems containing aliphatic or aromatic hydrocarbons have been

Winsor I   Winsor II   Winsor III   Winsor IV
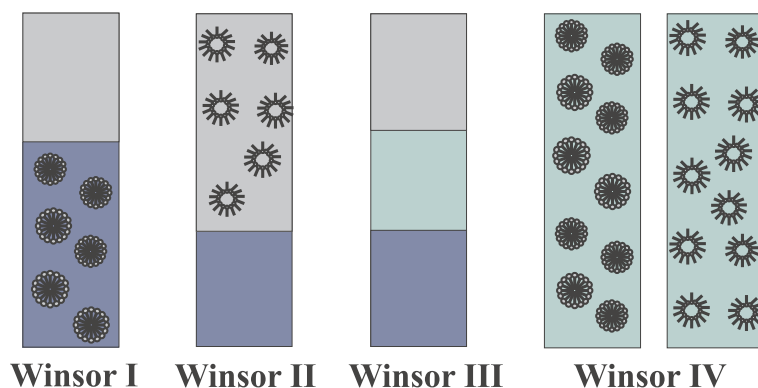
Figure 1.12: Schematic representation of the different Winsor phases, which might occur for a water-oil-surfactant (+ co-surfactant) system. For Winsor IV, a bicontinuous microemulsion is also a possible structure. The light gray indicates the oil phase, the blue the water phase and the light green indicates the microemulsion.

studied in detail and many data on compositions, properties and structures are reported.[17, 91, 94–96] However, as mentioned previously, triglycerides do not solubilize well into a microemulsion. It is observed that oils with a high molecular weight form microemulsions far less than their low molecular weight homologues. Especially, the formation of microemulsions with triglycerides (vegetable oil) at ambient conditions and without the addition of co-surfactants is most challenging.[4, 10–13, 64–66, 97–100]

1.5   Effects of Salts

1.5.1   General Aspects

The effect of electrolytes is omnipresent in all scientific fields. It is well known that ions play an essential role in a wide range of biological and physicochemical phenomena. The complexation of ions in cells, for example, is essential for the activity of biomolecules, like enzymes and drugs. Ions have a strong effect on the conformation and activity of proteins and nucleic acids and regulate the electrostatic potentials, conductance, and permeability of cell membranes. In chemistry, ions play an important role on the rates of chemical reactions or the cloud points of surfactant solutions.[101–105]

The effect of ions on surfactants strongly depends on the nature of the surfactant molecules. Anions, for example, have a strong effect on non-ionic surfactants or polymers. The solubility of non-ionic surfactants (containing ether groups) with temperature is limited by the dehydration of the EO groups (see Section 1.1.2). This cloud point of a non-ionic surfactant in water can be increased by the addition of chaotropic salts or decreased after adding kosmotropic salts to the solution. Anions are known to decrease the CMC's of non-ionic surfactants or to increase the attractive interactions between non-ionic micelles.[106–111] In addition, electrolytes have a strong influence on the phase behavior of ionic surfactants.[112]

1.5.2 The Hofmeister Series

Cations

$N(CH_3)_4^+$ NH_4^+ Cs^+ Rb^+ K^+ Na^+ Li^+ Mg^{2+} Ca^{2+}

SO_4^{2-} HPO_4^{2-} OAc^- cit^- OH^- Cl^- Br^- NO_3^- ClO_3^- BF_4^- I^- ClO_4^- SCN^- PF_6^-

Anions

kosmotropic		chaotropic
surface tension ↑		surface tension ↓
harder to make cavity		easier to make cavity
solublity hydrocarbons ↓		solublity hydrocarbons ↑
salt out (aggregate)		salt in (solubilize)
protein denaturation ↓		protein denaturation ↑
protein stability ↑		protein stability ↓
weakly hydrated soft cations of low charge density		strongly hydrated hard cations of high charge density
strongly hydrated hard anions of high charge density		weakly hydrated soft anions of low charge density

Figure 1.13: Hofmeister series of the cations and anions and the most important properties.[113]

The effect of salts on the solubility of proteins in water was first studied by F. Hofmeister, a pharmacologist, in 1888.[114, 115] He discovered that some ions precipitate proteins in water ("salting-out", kosmotrope) and certain ions support their solubilization ("salting-in", chaotrope). The "Hofmeister series" (also called

lyotropic series) gives a typical order of cations and anions and is illustrated in Figure 1.13. All ions to the left of the series tend to "salt-out", while all ions to the right side of the series (Figure 1.13) tend to "salt-in".[113–117] A borderline between "salting-in and -out" is often drawn at the chloride ion for anions and the sodium ion for cations. Comparing the effect of cations with the effect of anions, the series for cations goes from soft and weakly hydrated (left side in Figure 1.13) to hard and strongly hydrated (right side in Figure 1.13) and oppositely for anions. However, in general, the effect of cations is less pronounced than of anions. This is due to the fact that anions have stronger interactions with water as compared to cations (with the same size and absolute charge density). This effect is only valid when water-ion interactions are dominant. However, the effect of cations can be in the same order of magnitude as the effect of anions, if direct ion-ion interactions or ion-charged head-group interactions are dominant. In addition, the ion effects are only valid for inorganic salts and different for long-chain quaternary ammonium salts.[101, 106, 113] Ions to the left of the series increase the surface tension of solvents and decrease the solubility of non-polar molecules and thus, remain strongly hydrated in the bulk ("salting-out"). On the other hand, ions to the right of the series decrease the surface tension of solvents and increase the solubility of non-polar molecules and hence, adsorb at the interface ("salting-in").[101, 113]

The effect of salts correlates with the charge densities of the electrolytes, which means the ratio between the charge and the ion radius. Small anions, for example, tend to "salt-out", have small polarizabilities, and are expected to have low dispersion interactions and therefore, strengthen the hydrophobic interaction. In addition, these ions have a high electric field at short distances and tend to loose their water of hydration with great difficulties. In contrast, large anions tend to "salt-in", have large polarizabilities, strong dispersion interactions and thus, weaken the hydrophobic effect.[106, 113] Additionally, their electric field is weak and the hydration shell can be removed easily. "Salting-out" anions tend to compete for water at various interfaces, which results in a dehydration of the surface. "Salting-in" anions may loose their hydration shell and tend to serve themselves as solvating species at an interface. Extensive studies have shown that the counterion has a strong influence on

the thermodynamics and aggregation properties of surfactants.[113, 118–120] The differences in the cation effects appear less significant than those seen with the anions.

The properties of ions strongly depend on the environment and in particular on the counterions or the head-group of the surrounding. Specific ion effects are strongly affected by the concentration of the added salt. At very low salt concentrations, electrostatic interactions are usually dominant. At intermediate salt concentrations, the electrostatic interactions are mainly screened and specific ion effects are measured. At highest salt concentrations, most of the water is captured in the ion hydration shells and even "salting-in" ions can become "salting-out". However, because ions affect more than one significant parameter in the same system it is nearly impossible to describe responsible interactions of the ions in a confidential way.[106, 113, 118]

1.6 Characterization Methods

1.6.1 Microscopy Experiments

A) Optical Polarizing Light Microscopy

a) Theory of Optical Polarizing Light Microscopy

An optical light microscope utilizes visible light and a system of lenses to magnify images of small samples. Optical light microscopes were designed in the 17th century and are the oldest of its kind.[121]

An optical polarizing light microscope uses polarized light to illuminate the observed object. It differs from a conventional light microscope in a number of ways. Optical polarizing light microscopy can be utilized for both quantitative and qualitative studies and it represents a technique to distinguish between isotropic and anisotropic substances. Beside the common set up, a polarizing microscope is equipped with a pair of polars (polarizing devices), which are the polarizer and the analyzer. The polarizer is located between the illuminator and the condenser (beneath the sample) and defines the initial plane of polarization of the light entering the microscope. The analyzer defines the plane of polarization of the light reaching the ocular and is

usually placed between the objective and the ocular tube. One or both of the polars must be rotatable around the optical axis of the instrument.

Light from a common light source that vibrates in random directions is called non-polarized light. Light with vertical vibration that travels within a single plane is called linearly polarized light. However, when it rotates while it travels it is called circular or elliptical polarized light.

Isotropic materials show the same optical properties when probed in all directions. These materials do only possess one refractive index and no restriction on the vibration direction of light passing through them. When both the analyzer and polarizer are inserted into the optical path and are perpendicular to each other (the analyzer is turned 90° to the polarizer), the polarizer and analyzer are crossed with no light passing through. Consequently, isotropic sample appear dark/black under the microscope. By contrast, anisotropic materials exhibit optical properties that vary with the orientation of the incident light. These substances present a range of refractive indices, act as "light-splitter", and divide light rays into two orthogonal components. Hence, anisotropic samples appear in different colors and shapes under the microscope, when the filters are crossed.[121]
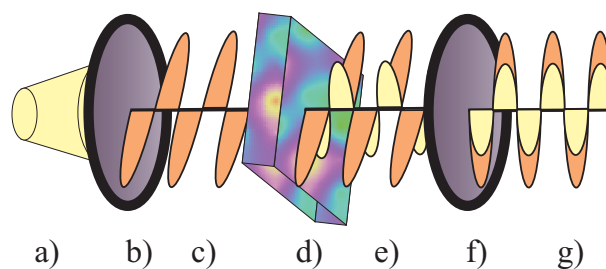
Figure 1.14: Scheme of a polarized wave passing through an anisotropic sample. The different components are: a) light source; b) polarizer; c) plane polarized light; d) birefringent sample; e) extraordinary and ordinary ray; f) analyzer; g) recombined light rays after interference.

The polarization process through an anisotropic sample works as followed (Figure 1.14). First, the light is linearly polarized by the first filter (polarizer). This polarized light hits the anisotropic sample and splits into an ordinary and an extraordinary beam. The light perpendicular to the anisotropy axis (ordinary ray) travels

with a different velocity through the birefringent sample than the light parallel to this axis (extraordinary ray). The faster component gains about half a wavelength of the slower component. Hence, the image contrast arises from the interaction of plane-polarized light with a birefringent sample, which produces two individual wave components that are each polarized in mutually perpendicular planes. After exiting the sample, the light components become out of phase, but are recombined with constructive and destructive interference when they pass through the analyzer.[121]

b) Phase Diagram Observation

Phase diagrams of a surfactant-water systems can be studied using optical polarizing microscopy because anisotropic liquid crystals (e.g. hexagonal or lamellar phase) show a characteristic pattern under the microscope using crossed polars. The so-called penetration scan is a common method to obtain information about the different liquid crystals formed over the whole concentration range. In addition, samples with different concentrations can be prepared to get more information about the liquid crystal formation as a function of temperature.
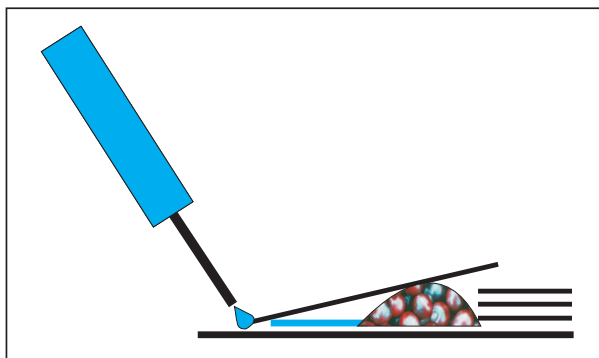
Figure 1.15: The penetration scan technique.

For the penetration scan technique, which was first described by Lawrence,[122] small amounts of the chosen surfactant are placed on a microscope slide. On one side of the surfactant a stack of three to four broken cover-slips is prepared. The surfactant will be covered with a cover-slip and quickly contacted with a drop of water (see Figure 1.15). The addition of water gives a monotonic increase of surfactant

concentration towards the center of the sample. The penetration scan method is a kinetic experiment, where water and surfactant continuously diffuse into each other. The different mesophases, which appear at various concentrations can be seen as distinct rings with characteristic optical textures between crossed polarizes.[39, 40] The relative viscosities, which also give an indication of phase structures, can be observed by slightly pushing the sample (mechanically). Depending on the liquid crystal, the sample can be low viscous and isotropic (normal/reverse micellar solution), low viscous and anisotropic (lamellar phase), highly viscous and anisotropic (normal/reverse hexagonal phase), or extremely viscous and isotropic (cubic phase). A complete phase diagram with exact transition temperatures and concentrations can be obtained by preparing bulk samples with different surfactant-water concentrations. To determine the transition temperatures, a microscope equipped with a hot stage and a temperature control is used. The different mesophases can be distinguished by their optical textures as mentioned before.[39, 40] Furthermore, airbubbles within the freshly prepared sample facilitate the analysis of the samples; the more viscous the sample, the more asymmetric are the airbubbles within the sample. For example, airbubbles within a lamellar phase appear symmetric round, while they are asymmetric and unformed in a hexagonal phase.

B) Transmission Electron Microscopy (TEM)

a) General Aspects

To obtain results on the nano-scale (e.g. micelles), transmission electron microscopy (TEM) is a common method. TEM is a technique, which uses a beam of electrons transmitted through a thin sample. The electron beam interacts with the sample, as it passes through, producing an image that results from the interaction of the transmitted electrons. The image is then magnified and focused onto an imaging device, which is usually a sensor like a CCD (charged coupled device) camera. In comparison to optical microscopy, TEM images are of significantly higher resolution. This provides the possibility to observe fine details of the sample, which can be tens of thousands times smaller than the smallest resolvable object of an optical light microscope. In this thesis, for example, TEM was used to obtain information about
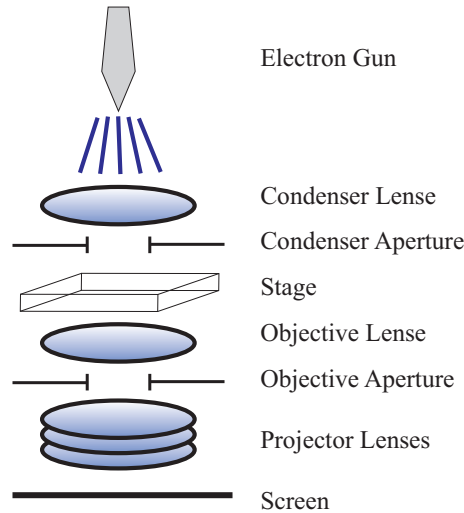
Figure 1.16: Construction of a transmission electron microscope (TEM) showing the principal components.

the micellar structure and size of the nano-emulsions.[123]

A TEM is composed of several components including a vacuum system, where the electrons travel, an electron emission source for generating the electron stream, a series of electromagnetic lenses, and electrostatic plates. The latter two allow the TEM user to guide and manipulate the beam (Figure 1.16).

The main component of a TEM is the emission source, which is called electron gun. In this context, thermionic and field emission guns (FEG) are the two most commonly used electron guns. By connecting this gun to a high voltage source (100-300 kV), it will start to emit electrons. This is carried out from a wire, which is superheated by an electric current until enough energy is produced to overcome the work function of the metal. The metal is usually tungsten filament or lanthanum hexaboride (LaB_6). These emitted electrons have a Boltzmann energy distribution and are incorporated into a tight beam. This extraction is usually aided by the use of a Wehnelt cylinder, which is an electrode inside the electron gun assembly and used to focus and control the electron beam. Afterwards, the upper lenses of the TEM allow the formation of the electron probe to the desired size and location for later interaction with the sample.[123, 124]

Two main physical effects are used to manipulate the electron beam. On the one hand, the electrons interact with a magnetic field, which causes the electrons to

move. Thus, electromagnets manipulate the direction of the electron beam. On the other hand, electrostatic fields can cause the electrons to be deflected through a constant angle. These two effects and the use of an electron imaging system allow sufficient control over the beam path. In comparison to an optical light microscope, the optical configuration of a TEM can be rapidly changed. For example, the lenses in the beam path can be enabled, their strength can be changed, or they can be completely disabled just by rapid electrical switching. Three different stages of lenses are typically used for a TEM, which are the condenser lens, the objective lens, and the projector lenses. The condenser lenses are responsible for primary beam formation, the objective lenses focus the beam, which passes the sample, and the projector lenses are used to expand the beam onto the imaging device.[123, 124]

b) Cryo-TEM
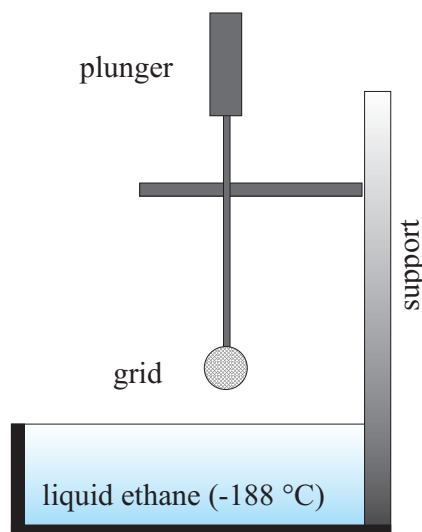
Figure 1.17: The freeze plunger used for cryo-TEM. For preparation, a drop of the sample is placed on the grid and then rapidly immersed into liquid ethane.

The preparation of the sample used for TEM can be very complex, since it has the requirement to be very thin. Specimens of high quality have a thickness of only a few nanometers, which is in the dimension of the mean free path of the electrons that penetrate the sample. Preparation of TEM samples is specific to the material, which is analyzed and the desired information needed from the sample. For liquid

samples, such as microemulsions, nano-emulsions, or vesicles, a common technique is cryomicroscope TEM (cryo-TEM). With this kind of TEM, one can study the sample at cryogenic temperatures in order to preserve and protect it. If a sample would be placed in a TEM without freezing it, evaporation would occur after the sample is brought into the vacuum and the electron beam of the microscope. The setup for cryo-TEM consists of an additional sample holder capable of maintaining the specimen at liquid nitrogen or liquid helium temperatures. It allows the observation of samples, which cannot be stained or fixed in any way and thus, it shows the sample in its native environment. Therefore, the sample is spread on an electron microscopy grid (about 3 mm diameter ring, with a thickness and mesh size ranging from a few to 100 μm) and preserved in a frozen-hydrated state by rapid freezing (Figure 1.17). This freezing process must be very fast to prevent the frozen water from forming cubic ice, which readily absorbs the electron beam and therefore, obscures the sample. The freezing usually takes place in liquid ethane (-188 °C) near liquid nitrogen temperature (-196 °C). If the freezing of the sample is fast, the water will solidify as an amorphous solid without any crystalline character. Liquid ethane is preferred over liquid nitrogen, which has a very low heat capacity. Thus, as soon as the grid is immersed into liquid nitrogen at room temperature, a small amount will warm and boil off. This effect slows the freezing process down and allows cubic ice to be formed. In contrary, liquid ethane has a much higher heat capacity than liquid nitrogen. The sample is prepared inside a liquid nitrogen reservoir and kept in a liquid nitrogen storage box. Henceforward, it can be introduced into the high-vacuum of the electron microscope column.[123, 125–128]

c) Freeze Etch-TEM

Freeze fracture or freeze etching is another method to prepare liquid samples containing colloidal structures and is shown in Figure 1.18. In this case, a Pt/C template of the sample is produced, which can be restored at room temperature for a long time. Again, the sample is frozen as previously described. Afterwards, it is transferred into a freeze fracture/etch box with a vacuum of less than 10^{-4} Pa and a temperature of -196 °C. Using a microtome (a cutting/separating instrument) the

sample is broken into two pieces. The fracture of the broken sample is irregular and occurs along lines of weakness, e.g. the hydrophilic/hydrophobic interface in case of microemulsions, nano-emulsions, or vesicles. The surface ice is then removed by vacuum. Therefore, the sample temperature is increased to about -100 °C. The microtome, having a temperature of -196 °C, is positioned above the sample and acts like a cooling trap. The sublimation of ice opens up deeper embedded structures. The bared fracture/etch face is then coated with a 1.5 nm thick layer of Pt or Pt/C (incident angle 45°). An additional 5 nm thick carbon layer coated under 90° stabilizes these thin metal layers (Figure 1.18). After the coating process (replication), the replica is cleaned and positioned on a microscopic grid and can then be analyzed any time with a TEM.[124, 129, 130]

1) cutting and breakage of the sample at -180 °C

2) etching and sublimation of the sample at -100°C
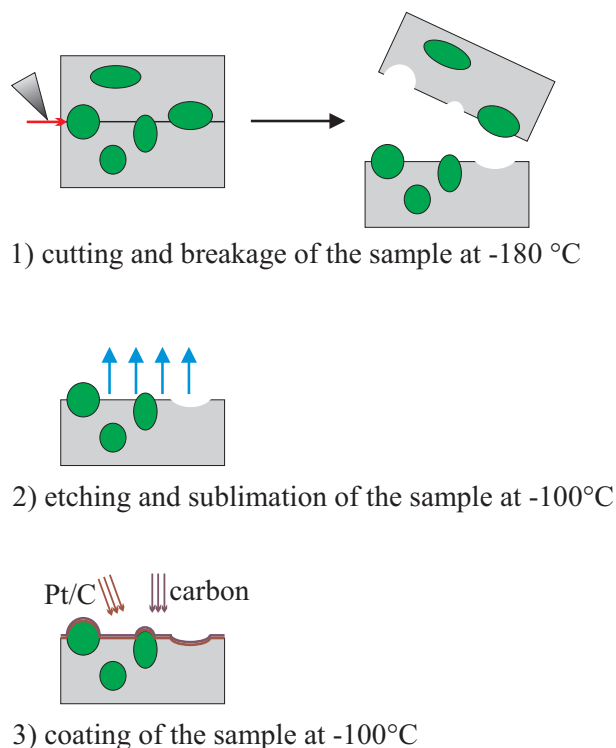
3) coating of the sample at -100°C

Figure 1.18: Schematic description of a freeze etching process.

1.6.2   Scattering Techniques

Scattering techniques based on light, X-ray, or neutron sources are often used to obtain information about the structure and the dynamics in systems containing

colloids, polymers, surfactants, or macromolecules. These kinds of measurements are different in comparison to imaging techniques, such as optical microscopy or freeze etch/cryo-TEM. Scattering techniques are model dependent. Furthermore, inter-particle interactions cannot be ignored. However, solutions, mixtures, or emulsions, can be well analyzed using a scattering method combined with an imaging technique.[131, 132]
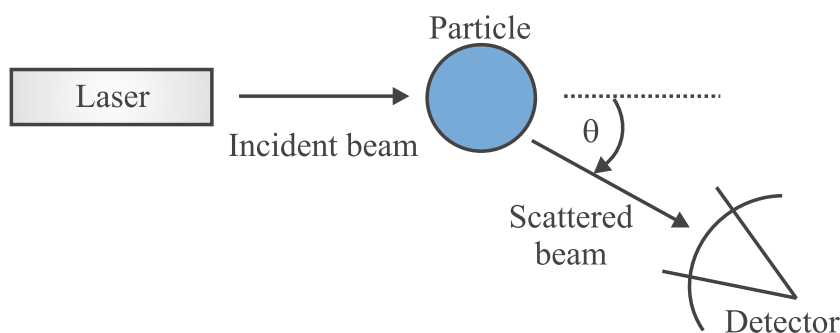
A) Dynamic Light Scattering (DLS)

Figure 1.19: Scheme of the incident light hitting a particle and of the resulting scattered light.

Light, i.e. an oscillating electromagnetic field, can interact with matter either by absorption or by scattering. If light hits a particle with a wavelength corresponding to the absorption band of the material, it will be absorbed. In contrary, if light hits the particle with a different wavelength, it will be transmitted or scattered.[132, 133] Basically, there are two different types of light scattering methods. Static light scattering experiments describe the measurement of the angle-dependence of the scattered intensity. This method provides information about the molecular weight of the scattering object. However, it will not be described in detail because this method was not used for this work. The interested reader is referred to numerous articles in the literature.[133–136] Dynamic light scattering (DLS, also known as photon correlation spectroscopy or quasi-elastic light scattering) describes the analysis of time dependent fluctuations in the scattered radiation. DLS experiments give information on how the particles are moving in Brownian motion and their shapes fluctuating with time.[133, 137] DLS measurements were used in this thesis to determine the size of the micelles or the droplets in solutions.

DLS is one of the most popular methods used for the study of colloidal systems.[138, 139] In a DLS experiment, the time correlation of the scattered light is measured. Therefore, the incident light of a monochromatic laser source (a light source with a single wavelength) hits the sample and the scattered beam is detected (Figure 1.19). Scattered radiation is obtained when the studied system is heterogeneous. The propagation of the incident beam is described by the scattering vector q, which is defined as:

$$q = \frac{4\pi n}{\lambda} \sin\frac{\theta}{2}, \tag{1.9}$$

where n is the refractive index of the medium, λ is the wavelength of the laser, and θ is the scattering angle with respect to the incident beam.[133, 137] For standard DLS measurements, the scattering angle θ is 90°. If the monochromatic beam with the frequency ν_0 hits an immobile particle, it emits the scattered radiation with the same frequency ν_0 in all directions. For a particle in motion and an immobile observer, the moving particle emits the scattered radiation with the same frequency ν_0. However, the observer will detect a frequency of $\nu = \nu_0 + \Delta\nu$. The frequency $\Delta\nu$ is the so-called Doppler shift, which depends on q and the velocity of the particle. The scattered particles in Brownian motion show a bell shaped spectrum, where the dynamic properties of the scatters can be obtained by Fourier transformation. The observed autocorrelation function, $g^{(2)}(t)$, is an average value of the product of the intensity observed at an arbitrary time t, $I(t)$, and the intensity observed at a time delay τ, $I(t+\tau)$. For a dispersion of polydisperse particles in Brownian motion, the intensity autocorrelation function is modeled by:

$$g^{(2)}(t) = \langle I(t)I(t + \tau)\rangle. \tag{1.10}$$

The decay rate, Γ, of the curve $g^{(2)}(t)$ is:

$$\Gamma = Dq^2 \tag{1.11}$$

where D is the diffusion coefficient, which is related to the hydrodynamic radius, R_H, by the Stokes-Einstein equation:

$$D = \frac{k_b T}{6\pi\eta R_H} \tag{1.12}$$

where k_b is the Boltzmann constant, T is the temperature, and η is the viscosity of the continuous phase of the sample. Therefore, the size of the aggregates can be deduced from DLS experiments.

Additionally, the polydispersity index can be obtained from DLS measurements. As the name implies, the polydispersity index (PDI) gives information about the polydispersity of a system. For a PDI < 0.05 monodispersed particles can be expected. For 0.1 < PDI < 0.2 a narrow, for 0.2 < PDI < 0.5 a large, and for PDI > 0.5 a very large size distribution can be assumed. For a PDI > 0.7, the correlation function cannot be interpreted and the results cannot be relied upon.[133, 137]

B) Small Angle Scattering (SAS)

a) SAS for Emulsions/Microemulsions

The use of small angle scattering techniques (X-ray [SAXS] or neutrons [SANS]) is very popular to analyze the structures of materials at the mesoscopic scale (1 nm to 1 μm). These methods are based on the interactions between the incident radiation and the particles and give quantitative information on size, shape, and structure of the colloidal particles in the solution. Information can be obtained from small angle scattering experiments when the incident wavelength λ falls within the size range of the structures to be detected. Therefore, the size of micelles, for example, can be examined.[131, 140]

X-rays are scattered by the electrons within a molecule, while neutrons are scattered by the nuclei. Thus, each type of radiation has its advantages and disadvantages depending on the system to be studied.

The scattering length of a single electron is $b_0^x = 2.8 \cdot 10^{-15}$ m[131], which is proportional to the atomic number and for a molecule containing z electrons it is given by:

$$b_i^x = z b_0^x \tag{1.13}$$

For neutrons, the coherent scattering length ($b_{i,coh}$) of an atom can be found in the literature.[131, 141] It varies with the type of nucleus and can be positive or negative. For example, for a hydrogen nucleus it is $b_{H,coh} = -3.74 \cdot 10^{-13}$ cm and for a deuterium nucleus it is $b_{D,coh} = 6.67 \cdot 10^{-13}$ cm.

The coherent scattering length density ρ_{coh}, is a parameter to quantify the scattering efficiency of different components in a system and is defined as:

$$\rho_{coh} = \frac{\sum_{i=1}^{n} b_{i,coh}}{V_m} = \frac{\rho N_A}{M} \sum_{i=1}^{n} b_{i,coh} \tag{1.14}$$

where V_m is the molecular volume of the particle, $b_{i,coh}$ is the scattering length, ρ is the mass density, M is the molecular weight, and N_A is the Avogadro constant (N_A = $6.022 \cdot 10^{23}$ mol^{-1}). The same equation can be used to calculate the scattering length densities of X-rays ρ_x, when $b_{i,coh}$ is replaced by b_i^x. Deuteration of some of the components within a solution changes the properties of the neutron scattering without significantly changing the physical and chemical properties. This is one advantage of SANS measurements. The scattering contrast of a particle in the solution can be expressed as:

$$\Delta\rho = \rho_p - \rho_s \tag{1.15}$$

with ρ_p and ρ_s corresponding to the scattering length densities of the particle and the solvent, respectively.

The scattering vector q, is related to the scattering angle and is defined as the modulus between the incident wave vector k_i and the scattered wave vector k_f and is given by:

$$q = |k_f - k_i| = \frac{4\pi n}{\lambda} \sin\frac{\theta}{2} \tag{1.16}$$

where n is the refraction index of the medium, λ is the wavelength of the laser, and θ is the scattering angle.

A complete SAS experiment includes measurements of the scattering intensities of the sample, its external background (empty cell), and of a standard sample that is necessary for the absolute calibration. Furthermore, transmission measurements of the sample, the reference sample, the empty cell, the standard sample, and the direct beam must be performed. In an ideal diluted solution, where each particle is independent from the others, the scattering intensity $I(q)$ is proportional to the so-called form factor $P(q)$. However, with increasing concentration, each particle will notice its neighbor. Thus, the position of one particle is dependent on the position of the other particles (e.g. due to particle interactions). The particle interaction

can be described by the so-called structure factor $S(q)$. Therefore, the scattering intensity can be expressed as:

$$I(q) = nP(q)S(q) \tag{1.17}$$

where n is the number density $(n = \frac{N}{V})$.[24, 25]

Information can be obtained directly from the scattering curves by means of Porod analysis.[131, 140] A Porod limit is only obtained when Iq^4 versus q^4 yields a limiting value at large q. For a sharp interface, the scattering intensity $I(q)$ is decreasing with q^{-4} for high q values. Thus, the Porod law can be expressed as:

$$lim_{x \to \infty}(Iq^4) = 2\pi^2 \Delta \rho^2 \Sigma \tag{1.18}$$

where $\Delta \rho^2$ is the square of the scattering contrast between the polar and the non-polar part. When the polar/non-polar interface is rough, no Porod limit can be observed at large q. In addition, the subtraction of the background is essential for the determination. Without the subtraction usually no Porod limit is observed. The background A can be obtained from the slope of the curve $I(q)q^4$ versus q^4 as:

$$I(q)q^4 = B + Aq^4. \tag{1.19}$$

From the Porod law the specific area, Σ, at the polar/non-polar interface can be calculated. This value is necessary to evaluate the radius of spherical micelles from:

$$R = \frac{3\phi}{\Sigma} \tag{1.20}$$

where ϕ is the volume fraction. The polar (ϕ_{pol}) and non-polar (ϕ_{apol}) volume fractions can be calculated from the known composition of the solution and the corresponding molar volumes. If the Porod limit is observed, the experimental invariant, Q_{exp}, can be determined by:

$$Q_{exp} = \int_0^\infty I(q)q^2 dq = \int_0^{q_{exp}} I(q)q^2 dq + \frac{[I(q)q^4]}{q_{exp}} \tag{1.21}$$

which should be identical to the theoretical invariant, Q_{theo}, given by:

$$Q_{theo} = 2\pi^2 \Delta \rho^2 \phi_{pol}(1 - \phi_{pol}) \tag{1.22}$$

Small angle scattering (SAS) experiments have been widely used to study aqueous microemulsions.[142–144]

b) SAS for Liquid Crystals

Beside microemulsions and nano-emulsions, ordered systems, like liquid crystalline phases, can also be studied using small angle scattering techniques. These methods are accurate, non-destructive, and usually require only small sample volume. It is a powerful tool when investigating the geometry of amphiphilic systems. Spectra, similar to powder spectra, with Bragg peaks in different ratios are observed. These obtained Bragg reflections are produced by the ordered orientation of the surfactant interface providing an accurate identification of isotropic and anisotropic liquid crystalline structures.[17, 131, 145]
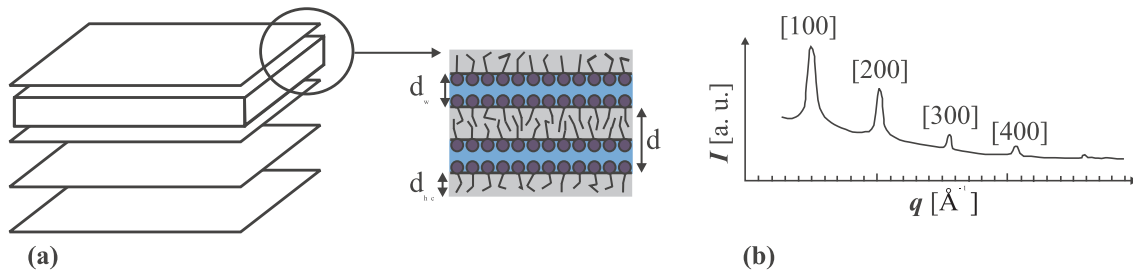
SAS of the Lamellar Phase (L_α)

Figure 1.20: a) Idealized structure of the lamellar phase; d_w is the water layer thickness, d_{hc} the thickness of the uniform hydrophobic layer containing all the hydrophobic tails of one layer, and d is the bilayer thickness. b) Typical SAXS spectra of a lamellar phase with the Bragg reflections in the ratio $1 : 2 : 3 : 4 \ldots$, etc. The numbers give the reflection indices.[17]

The ideal packing of a lamellar phase consists of planar stacks of amphiphilic bilayers (as already described in Section 1.1.3). The structure of the lamellar phase is of the smectic type (a 1D lattice), i.e. the lamellae are parallel and equidistant, without other correlation in position and orientation (Figure 1.20a). Due to the repeating sequence of the bilayers, the L_α phase can easily be determined using scattering techniques. Within this layer, the fluid-like characteristic of the alkyl chains is shown by a diffraction peak corresponding to a Bragg reflection at 4.5 Å.

Furthermore, sharp Bragg reflections in the ratio $1 : 2 : 3 : 4 \ldots$, etc. are observed. Any topology that is geometrically ordered along a single axis, like smectic ordering, will show these ratios of the Bragg reflections. A typical SAXS spectra of a L_α phase is given in Figure 1.20b.[17, 131, 145]

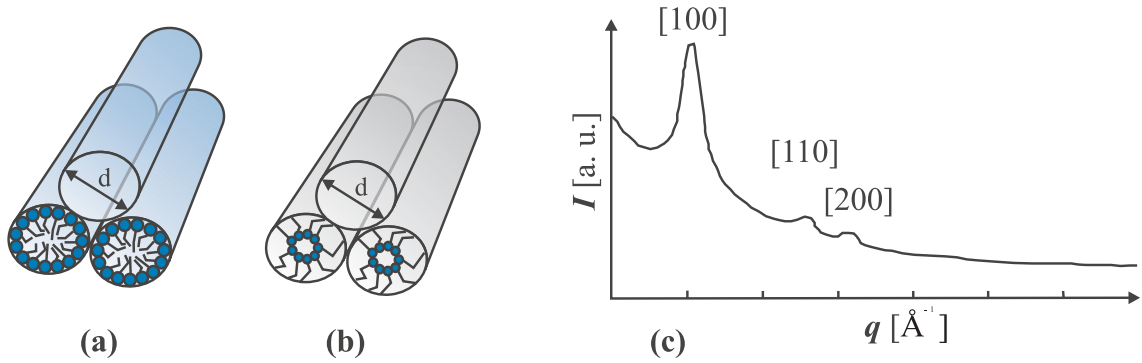*SAS of Hexagonal Phases (H_1/H_2)*

Figure 1.21: The normal (a) and reverse hexagonal (b) phase, d is the diameter of the cylinders. c) Typical SAXS spectra of a hexagonal (normal or reverse) phase with the Bragg reflections in the ratio $1 : \sqrt{3} : \sqrt{3} : \ldots$, etc. The numbers give the reflection indices.[17]

As already mentioned in the previous Section 1.1.3, the hexagonal phase consists of a dense packing of cylindrical (rod-like) infinite micelles, which are oriented parallel to each other and arranged on a two-dimensional (2D) hexagonal lattice. The lateral position and the relative orientation of the rods are fixed. Thus, the positions are random in the direction of the rod axis. The projection on the plane perpendicular to the rod axis defines the 2D lattice. In contrary to the lamellar phase, where the curvature toward both sides is equal, two different curvatures can be obtained for the hexagonal phase, normal (H_1) or reverse (H_2) (Figure 1.21a). Scattering studies of both phases, H_1 and H_2, show Bragg reflections in the ratio $1 : \sqrt{3} : \sqrt{4} : \sqrt{7} : \sqrt{12} \ldots$, etc. again with a diffuse reflection at 4.5 Å. The typical SAXS pattern of a hexagonal phase is given in Figure 1.21c.[17, 131, 145, 146]

SAS of Cubic Phases (I_1/I_2, V_1/V_2)

There are two different kinds of cubic phases, one comprised of globular small mi-

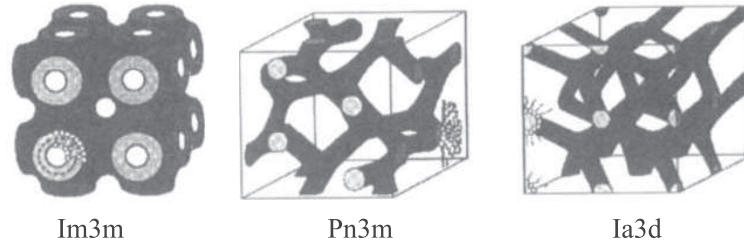Im3m   Pn3m   Ia3d

Figure 1.22:   Schematic representation of the three most common bicontinuous cubic structures.[17]

celles (I_1 and I_2) and one with a bicontinuous cubic structure (V_1 and V_2, already described in the previous Section 1.1.3). In a cubic phase, aggregates of finite size are packed in a three-dimensional (3D) lattice. The most usual form of the I-phases is the body-centered cubic (bcc) array of identical micelles with the 3D space group Im3m. Furthermore, face centered cubic (fcc) with the most common space group Fm3m and clathrate with the space group Pm3n or Fd3m can be observed. The size of the globular micelles within the lattice is similar to the size of the micelles in the solution. However, within the space group Pm3n two different micelle sizes are observed, one larger than the other.

The V-phases exhibit the most complex spatial organization of all known liquid crystals. These phases were first detected in lipid-water systems and dry metallic soaps by Luzzati in the 1960s.[145] The most common space groups of the V-phases, obtained from scattering measurements are the Pn3m, Im3m and Ia3d space group. The aggregates form a 3D network extending throughout the sample (see Figure 1.22). The first reported bicontinuous cubic phase was a body-centered lattice, Ia3d phase, also introduced by Luzzati in the 1960s.[43] He proposed rod-like aggregates joined three-by-three to form two independent networks. For determining and distinguishing the different structures of cubic phases with scattering methods, usually a minimum of four peaks in the spectra is necessary. The Bragg reflection ratios of the most common cubic phases are given in Table 1.1.[14, 41–45, 145]

Mesophase	Symmetry	Peak Ratios
I_1/I_2	Im3m	$1 : \sqrt{2} : \sqrt{4} : \sqrt{6} : \sqrt{8} : \sqrt{10}$: etc.
	Fm3m	$1 : \sqrt{3} : \sqrt{4} : \sqrt{8} : \sqrt{11} : \sqrt{12}$: etc.
	Pm3n	$1 : \sqrt{2} : \sqrt{4} : \sqrt{5} : \sqrt{6} : \sqrt{8}$: etc.
	Fd3m	$1 : \sqrt{3} : \sqrt{8} : \sqrt{11} : \sqrt{12} : \sqrt{16}$: etc.
V_1/V_2	Im3m	$1 : \sqrt{2} : \sqrt{4} : \sqrt{6} : \sqrt{8} : \sqrt{10}$: etc.
	Pn3m	$1 : \sqrt{2} : \sqrt{3} : \sqrt{4} : \sqrt{6} : \sqrt{8}$: etc.
	Ia3d	$1 : \sqrt{6} : \sqrt{8} : \sqrt{14} : \sqrt{16} : \sqrt{18}$: etc.

Table 1.1: Peak ratios and symmetry of the most common cubic phases.

Analysis of the SAS spectra

Various parameters of the liquid crystals can be obtained from the resulting scattering data. The alkyl chain volume fraction ϕ_a is necessary for further calculations. This can be obtained by using the expression by Luzzati as follows:[145]

$$\phi_a = \frac{M_a}{M(1 + \frac{\rho_a(1-c)}{\rho_w c})} \tag{1.23}$$

where M is the molecular weight of the surfactant, M_a is the molecular weight of the hydrophobic tail, c is the weight fraction of the molecule, and ρ_a and ρ_w are the densities of the hydrophilic and hydrophobic part, respectively. The water volume fraction ϕ_w can be calculated according to $\phi_w = 1 - \phi_a$.

For the lamellar phase, the thickness of the uniform hydrophobic layer d_{hc}, containing all the hydrophobic tails of one layer can be calculated after Luzzati,[145] using the separation of the bilayers d_0, and the volume fraction ϕ_a:

$$d_{hc} = \phi_a d_0 \tag{1.24}$$

assuming that the bilayers of the lamellar phase are infinite, continuous and without breaks. Furthermore, the area per molecule S_a, within the lamellar phase, can also be calculated as follows:

$$S_a = \frac{2V_a}{d_{hc}} = \frac{2V_a}{\phi_a d_0} \tag{1.25}$$

where V_a denotes the volume of the hydrophobic tail.

The diameter of the amphiphile cylinder d_{ca} of a hexagonal phase is expressed as:

$$d_{ca} = 2d_0\left[\frac{2\phi_a}{\pi\sqrt{3}}\right]. \tag{1.26}$$

The minimum distance between the cylinders d_w is defined as $d_w = d_p$ - d_{ca} with d_p being the lattice parameter. The surface area per molecule S_a for the normal hexagonal phase can be calculated as:[45]

$$S_a = \frac{[4\phi_a V_s] \cdot 10^{24}}{d_{ca} N_A n_a} \tag{1.27}$$

where V_s is the volume of the specimen, N_A is the Avogadro number, and n_a is the number of moles of amphiphile per gram of mesophase.

Similar calculations can be made for the reverse hexagonal phase, where the diameter of the water cylinders d_{cw} is given by:

$$d_{cw} = 2d_0\left[\frac{2\phi_w}{\pi\sqrt{3}}\right]. \tag{1.28}$$

The surface area per molecule S_a for the reverse hexagonal can be expressed as:[45]

$$S_a = \frac{[4\phi_w V_a] \cdot 10^{24}}{d_{cw} N_A n_a} \tag{1.29}$$

where ϕ_w corresponds to the volume fraction of water.

1.6.3   Nuclear Magnetic Resonance (NMR)

A) General Aspects

Nuclear magnetic resonance is a powerful and theoretically complex analytical tool. In chemistry, it is one of the most important techniques to determine the molecular structure, conformation, and the purity of a substance. Furthermore, molecular dynamics in a sample as well as different liquid crystals formed by amphiphilic compounds in an aqueous solution can be examined by NMR spectroscopy. Nuclear magnetic resonance (NMR) was first described in 1938 by I. Rabi and was first measured in 1944.[147] Until now, a lot of information about this technique is available in the literature and only a short overview about the fundamentals is provided in this section.[148, 149]

Nuclei	Unpaired Protons	Unpaired Neutrons	Net Spin	γ [MHz T^{-1}]
^{1}H	1	0	$\frac{1}{2}$	42.58
^{2}H	1	1	1	6.54
^{31}P	1	0	$\frac{1}{2}$	17.25
^{23}Na	1	2	$\frac{3}{2}$	11.27
^{14}N	1	1	1	3.08
^{13}C	0	1	$\frac{1}{2}$	10.71
^{19}F	1	0	$\frac{1}{2}$	40.08

Table 1.2: Characteristic properties of some nuclei. γ is the gyromagnetic ratio.[150]

The nuclei of many element isotopes have a characteristic spin (I). For example, even mass nuclei composed of odd numbers of protons and neutrons have integral spins (e.g. $I = 1, 2, 3, \ldots$, as ^{2}H, ^{14}N). Odd mass nuclei composed of an odd number of nucleons have fractional spins (e.g. $I = \frac{1}{2}, \frac{3}{2}, \frac{5}{2} \ldots$, like ^{1}H, ^{13}C, ^{19}F, ^{23}Na). And even mass nuclei with an even number of protons and neutrons have no spins ($I = 0$, like ^{12}C, ^{16}O, ^{32}S). Some characteristic properties of a few nuclei are given in Table 1.2. Nuclei with a spin $\frac{1}{2}$ have a spherical charge distribution and a magnetic moment (μ). A non-spherical charge distribution on the other hand, is observed for all other nuclei ($I \geq 1$), which possess an electric quadrupole moment (eQ). In the absence of an external magnetic field, the orientations of a nucleus with a spin of $\frac{1}{2}$ are of equal energy. If an external magnetic field B_0 is applied, nuclei with a spin $\frac{1}{2}$ exist in two nuclear spin states of different energy (Figure 1.23a).

Spin states, which are oriented parallel to the applied magnetic field are lower in energy than in the absence of the external field and referred to as α (m = $+\frac{1}{2}$). In contrast, spin states oriented anti-parallel to the applied field are higher in energy than without the external field and referred to as β (m = $-\frac{1}{2}$). The rotational axis of a spinning nucleus cannot be orientated exactly parallel/anti-parallel with the direction of the applied field, but must precess (a motion similar to a gyroscope) around this field at an angle, with an angular velocity given by:
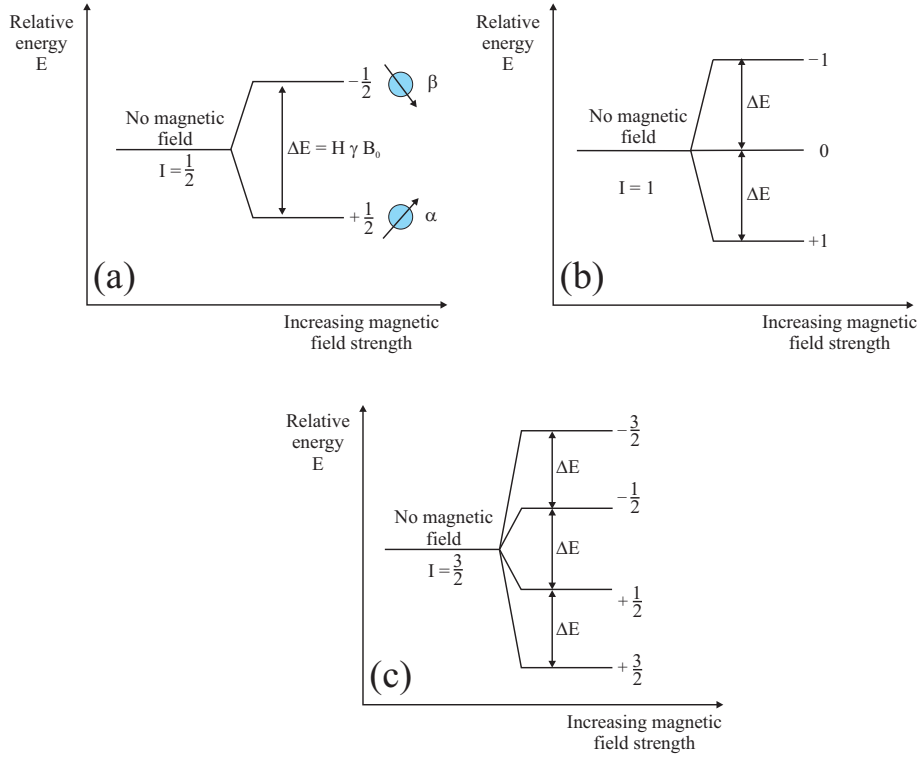
$$\omega_0 = \gamma B_0 \tag{1.30}$$

Figure 1.23: Energy profile of a nucleus with a spin of (a) $\frac{1}{2}$, (b) 1, and (c) $\frac{3}{2}$, before and after an external field B_0 is applied.

where ω_0 is the precession rate (so-called Larmor frequency), and γ is the gyromagnetic ratio. The gyromagnetic ratio γ is defined as a constant of proportionality between the nuclear angular momentum and the magnetic moment. Each nucleus has a characteristic value of γ and some examples are given in Table 1.2. The difference in energy between the two spins is very small and depends on the external magnetic field strength and is defined as followed:

$$\Delta E = \hbar\omega_0 = \gamma\hbar B_0 \tag{1.31}$$

When an energy separation exists, it is possible to induce a transition between the various spin states. By irradiating the nucleus with electromagnetic rays of the correct energy, a nucleus with an energetically lower orientation can be transferred to a higher orientation and absorb energy. In contrast, a nucleus with an energetically higher orientation can be transferred to a lower orientation and release energy. The number of transitions in both directions is given by multiplying the starting level population by a probability, which is the same for transitions in either direction. If
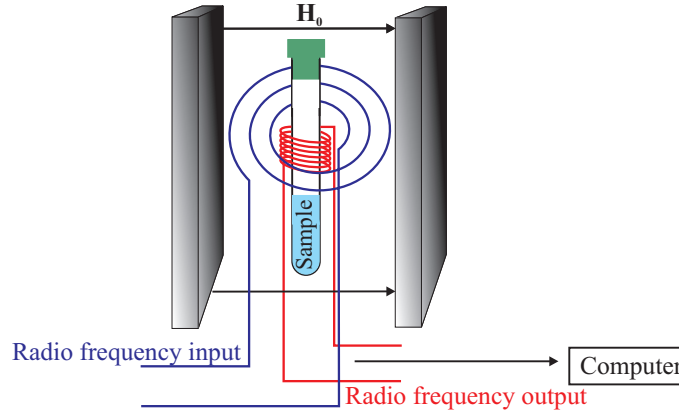
Figure 1.24: Construction of a nuclear magnetic resonance spectrometer.

the energy populations are the same, the number of transitions and the absorption and release of energy will be the same. Hence, nothing will be observed. However, if the populations are not equal, a net absorption or release of energy is obtained. The external magnetic field B_0 is homogeneous and created with a large magnet, which is usually a super-conducting solenoid. For example, a magnetic field of 7.05 T (Tesla, unit of the magnetic flux) is applied, resulting in a frequency, ν, of 300 MHz for ^{1}H and 75 MHz for ^{13}C. However, the frequency can be changed by varying the applied magnetic field; the larger the applied field, the better the sensitivity and the resolution. A typical construction of a NMR instrument is given in Figure 1.24.[148, 149] where $\hbar$ is the reduced Planck constant (Dirac constant).

B) Quadrupole Splittings

A nucleus with a spin quantum number $I > \frac{1}{2}$ (e.g. 1 for ^{2}H, $\frac{3}{2}$ for ^{23}Na and ^{7}Li) possesses an electric quadrupole moment, which interacts with the electric field gradients at the nucleus.[151]

In the simplest case of nuclei with a spin quantum number $I = 1$, the first order interaction gives a splitting of the resonance line into a symmetric doublet ($2I$ peaks). The energy profile for a spin quantum number $I = 1$ is given in Figure 1.23b. The resulting frequency separation is:

$$\nu_Q = \frac{3e^2qQ}{4h}(3\cos^2\theta - 1) \qquad (1.32)$$

where eQ is the electric quadrupole moment of the nucleus, eq is the principal electric field gradient tensor component, h is the Planck constant, and θ is the angle between the direction of the principal component of the electric field gradient and the magnetic field. The quadrupole coupling constant is defined as $\frac{e^2 qQ}{h}$ and will be denoted as E_Q in the following. In the case of a rapid molecular reorientation, the quadrupole splitting will be proportional to $< 3\cos^2 \theta - 1 >$ and thus, it equals zero for an isotropic reorientation. In anisotropic liquid crystals $< 3\cos^2 \theta - 1 >$ will not be effectively reduced to zero and a quadrupole splitting may be observed. This quadrupole splitting is usually smaller than obtained in solids.

For a molecule with a known value of E_Q, the degree of orientation within the crystalline structure in an anisotropic mesophase can be evaluated from the quadrupole splitting. Information concerning the orientation mechanism of a liquid crystal can be obtained by studying the influence of the temperature and the composition of the mesophases on the degree of molecular orientation. The quadrupole splitting Δ in partially oriented molecules under rapid reorientation is described as:[151]

$$\Delta = |\frac{3}{4} E_Q S \langle 3\cos^2 \theta_{LD} - 1 \rangle| \tag{1.33}$$

where S is the order parameter, which is a factor characterizing the partial orientation of the molecules and θ_{LD} is the angle between the mesophase director (i.e. the axis of the rotational symmetry) and the magnetic field direction. In a lamellar phase, the direction of the constraint is perpendicular to the lamellar planes and parallel to the rods in a hexagonal phase (normal and reverse). The order parameter S depends on the time-average angle between the electric-field gradient and the mesophase axis (θ_{DM}) and is given by:[151]

$$S = \frac{1}{2} \langle 3\cos^2 \theta_{DM} - 1 \rangle \tag{1.34}$$

In the case of partially oriented D_2O molecules, the explicit expression for S is:

$$S = S_{11} cos^2 \beta + S_{22} cos^2 \beta \tag{1.35}$$

where S_{11} and S_{22} are independent orientation matrix elements, which may have values between $-\frac{1}{2}$ and $+1$, and β denotes half the D-O-D angle in the D_2O molecule.

As seen from equation 1.33, the variations of the S parameter may be attributed to changes in the degree of orientation (the extend to which the orientation matrix elements deviate from zero) or changes in the direction of the preferred orientation (the ratio between S_{11} and S_{22}).

The frequency difference between two neighboring peaks (Δ) for a powder sample, where the electric field-gradient is axially symmetric and the most probable value of θ_{LC} is 90°, can be expressed as:[151]

$$\Delta = \frac{3}{4} E_Q S \qquad (1.36)$$

As found from relaxation studies, the value of E_Q is approximately constant. Thus, the changes in quadrupole splittings arise from different S values. For water molecules in lyotropic liquid crystals, the Δ (Δ^w) values are determined by the fraction of "bound" water. These water molecules are in rapid exchange with the rest of the water ("free" water) with $\tau_{exch.}^{-1} \approx 10^7 s^{-1}$.[152] It is generally assumed that $\Delta^w = 0$ for free water and thus, Δ^w for bound water is given by:

$$\Delta^w = p_b^w \delta_b^w = p_b^w \frac{3}{4} E_{Q,b}^w S_b^w \qquad (1.37)$$

where p_b^w is the fraction of bound water (subscript b denotes bound) and is defined as:

$$p_b^w = n_b \left(\frac{x_s}{x_w} \right) \qquad (1.38)$$

with n_b being the number of bound water molecules per surfactant head-group and x_s and x_w are the mol fractions of surfactant and water, respectively. Hence, information on the interactions between the water and the surfactant within the liquid crystal as well as information on the liquid crystalline structure can be obtained. Similar considerations hold for ^{23}Na resonances of counterions. Sodium nuclei have a spin quantum number of $I = \frac{3}{2}$, the first order interaction gives a splitting of the resonance line into a single peak and a symmetric doublet. The energy profile for a spin quantum number $I = \frac{3}{2}$ is given in Figure 1.23c. Sodium quadrupole splittings, $\Delta(^{23}$Na), arise from the presence of a net field gradient at the sodium ion due to an asymmetric hydration shell. This only occurs for the fraction of ions within a distance of 2-3 Å of the head-group (termed "bound"). Also in this case, the values

$\Delta(\Delta^{Na})$ arise from the fraction of "bound" counterions (p_b^{Na}).

$$\Delta^{Na} = p_b^{Na}\delta_b^{Na} = p_b^{Na}\frac{3}{4}E_{Q,b}^{Na}S_b^{Na} \qquad (1.39)$$

Due to different orientations of the aggregate surfaces with respect to the liquid crystalline axis, when molecular ordering is equal in the hexagonal and lamellar phases, $S_b(\text{lam}) = -2\,S_b(\text{hex})$ is expected. A more detailed theoretical description of NMR resonance splittings is given in a number of articles.[151, 153–158]

Chapter 2

Experimental

2.1 Materials

The extended surfactant (batch No.: 8625-2, 8625-47, and 8664-11), sodium linear-alkyl-polypropylene-oxide-polyoxyethylene sulfate containing 12-14 carbons in its alkyl tail, an average of 16 propylene oxides (PO) and an average of 2 ethylene oxides (EO; C_{12-14}-$(PO)_{16}$-$(EO)_2$-SO_4Na, Figure 2.1) was synthesized and donated by Huntsman Corporation (Texas, USA). The supplied surfactant is an isotropic solution with low viscosity, containing 23 wt% active, 0.1 - 0.2 wt% electrolyte, plus water to 100 wt%. The electrolyte concentration was determined by ion-chromatography, using a 6.1006.100 Metrosep Anion Dual 2 column.

A 1 mL : 1000 mL dilution of the 23 wt% solution was prepared and an eluent consisting of 2 mmol L^{-1} $NaHCO_3$, 1.6 mmol L^{-1} Na_2CO_3, and 15% acetone was used.
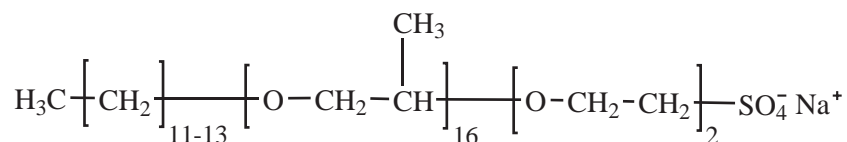
Figure 2.1: Structure of the used extended surfactant: X-AES.

For experiments with the neat surfactant and its dilutions, water was removed by lyophilization. The product was dried under vacuum, resulting in a viscous, but pourable yellowish liquid containing some (solid) particles. The final water

content was measured by means of the Karl-Fischer titration technique and was determined to be ≤ 0.3 wt%. The dried surfactant is liquid at room temperature. The liquid rather than a solid is formed because of the polydispersity of the surfactant and the PO groups which do not crystallize. Furthermore, the obtained solid particles were isolated from the surfactant and examined by optical microscopy, IR-spectroscopy (Jasco FTIR-610 spectrometer), elementary analysis (vario EL III elemental analyzer, Elemental Analysensysteme GmbH), and energy-dispersive X-ray spectroscopy (EDAX microanalyser mounted on a FEI Quanta 400T scanning electron microscope at 15 kV). More information about these particles is provided in Section 3.1.

Deuterated water was obtained from Deutero (Kastellaun, Germany) with a purity of 99.9%.

Rapeseed oil was purchased from Euco GmbH (Germany).

NaCl ($\geq$ 99.5%), NaBr ($\geq$ 98%), NaOAc (sodium acetate, $\geq$ 99.0%), NaNO$_3$ ($\geq$ 99.5%), Na$_2$SO$_4$ ($\geq$ 99.0%), KCl ($\geq$ 99.5%), LiCl ($\geq$ 99%), CsCl (= 99.5%), and Na$_2$HPO$_4$ ($\geq$ 99.5%) were received from Merck (Germany). NaSCN ($\geq$ 98.5%), NaBu (sodium butanoate, $\geq$ 99%), and NaOc (sodium octanoate, $\geq$ 99%) were obtained from Sigma (Germany). Choline chloride ($\geq$ 98%), and sodium xylene sulfonate (SXS) were purchased from Aldrich (Germany). SXS was received as an aqueous solution containing 40% of active in water.
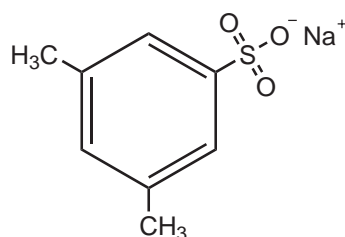
Figure 2.2: Structure of the hydrotrope sodium xylene sulfonate (SXS).

For experiments with lower SXS concentration H$_2$O, was removed by lyophilization. The product was dried under vacuum, resulting in a white powder. The final water content was measured using the Karl-Fischer titration technique and was

determined to be ≤ 0.1 wt%. The structure of SXS is shown in Figure 2.2.

All components were used as received.

2.2 Methods

2.2.1 The Surfactant/Water-System (Section 3.1)

Phase Diagram

Cloud points (temperatures) of surfactant solutions were measured using 1-2 mL samples between 5 and 30 wt% of X-AES in distilled water by slowly heating/cooling with a heating rate of 1-2 °C min^{-1}. The phase diagram was obtained by visual observation of the transition from clear to turbid and *vice versa*. For accurate measurements, the samples were completely immersed in a water bath and both the bath and the samples were stirred using a magnetic stirrer. The temperatures were recorded using a digital thermometer and ranged between 0 and 80 °C (accuracy $\pm$ 0.5 °C).

Optical Polarizing Light Microscopy

A Leitz Orthoplan polarizing optical microscope (Wetzlar, Germany), a Linkam hot stage with a Linkam TMS90 temperature control (accuracy $\pm$ 0.5 °C) and a Linkam CS196 cooling system (Waterfield, UK) were used to conduct the microscopy experiments. First, the sequence of mesophases was determined by using the optical microscopy penetration technique, described by Lawrence,[122] across a surfactant/water concentration gradient at various temperatures. Then, specific concentrations between 30 and 95 wt% of surfactant in water were chosen to obtain the phase transitions as a function of the temperature (0 to 90 °C), using the known different textures for the various mesophases.[39, 40] The accuracy of the transition temperatures was $\pm$ 1 °C. The heating and cooling rates for all measurements were 10 °C min^{-1}. Heating and cooling scans gave the same transition temperatures within $\pm$ 1 °C.

NMR-Measurements

NMR measurements were performed using a Bruker BioSpin Avance 400 spectrometer and variable temperature probes, operating at 105.8 MHz, 400.1 MHz and 61.4 MHz for ^{23}Na, ^{1}H and ^{2}H resonances, respectively. The $\pi/2$ pulse lengths were 8.7 μs for ^{23}Na resonance, 7.8 μs and 9.4 μs for ^{1}H and ^{2}H resonance, respectively. Temperatures were measured to be constant within $\pm$ 1 °C. Samples for NMR were prepared by weighing a total amount of 3.0 g into test tubes. The content was mixed by a magnetic stirrer for the lower viscosity samples or with repeated centrifugation until homogeneous for the higher viscosity samples. Then, the samples were transferred into NMR tubes (5 mm o. d.), while the higher viscosity samples were transferred into 5 mL syringes and squeezed into the tubes using a Teflon hose. Afterwards, the prepared samples were centrifuged again to remove air bubbles.

Dynamic Light Scattering (DLS)

Dynamic light scattering experiments were carried out using a model-CGS-II from ALV (ALV GmbH, Germany). Measurements were performed on surfactant solution between 0.1 and 5 wt% and over the temperature range of 10-30 °C ($\pm$ 0.02 °C). To obtain accurate results, each sample was thermostated for 30-45 min at the chosen temperature. All measurements were performed at a scattering angle of 90°. The samples were filtered before each measurement using 25 mm syringe filters with a w/0.2 μm cellulose acetate membrane.

Cryo-TEM

For cryo-TEM measurements, samples containing 0.5, 1.0 and 5.0 wt% surfactant were prepared. The TEM specimens were made by placing a small drop (ca. 4 μL) of the sample on a carbon grid. Immediately after blotting with a filter to obtain a thin liquid film over the grid, the sample was plunged into liquid ethane (at its melting temperature). The vitrified film was then transferred under liquid nitrogen to the electron microscope. The grid was examined with a Zeiss EM922 EF transmission electron microscope (Zeiss NTS GmbH). Examinations were carried out at

temperatures around 90 K. The TEM was operated at an acceleration voltage of 200 kV. Zero-loss filtered images (DE = 0 eV) were taken under reduced dose conditions (100-1000 e/nm^2). Images were registered digitally by a bottom mounted CCD camera system (Ultrascan 1000, Gatan), combined and processed with a digital imaging processing system (Digital Micrograph 3.9 for GMS 1.4).

Surface Tension Measurements

Surface tension measurements were performed at 25 °C using a K100 tensiometer (Kruess GmbH, Germany). The instrument was equipped with a du Nouy Pt-Ir ring. The initial solution was prepared by diluting the 25 wt% surfactant stock solution to 5 wt% using bi-distilled water. The different concentrations of the system were achieved by automatic titration of distilled water by the tensiometer. For this, the surfactant solution was reduced by 10 mL, while 10 mL of distilled water was added. The solution was diluted 90 times, while each concentration was measured ten times to obtain a valid result. Each concentration was stirred for 300 s before the next measurements.

Langmuir Isotherm

Surface measurements were made using a Langmuir Blodgett trough. Surface pressure-area (π-A) isotherms of the surfactant were obtained using a computer controlled NIMA Langmuir trough (NIMA Technology, UK) with a total area of 560 cm^2. Different surfactant concentrations (2.5, 5, 10, 40 mg mL^{-1}) in chloroform were prepared and spread onto a water subphase at room-temperature. A minimum period of 30 min was allowed for the evaporation of the solvent before compression. The (π-A) isotherms were measured using the Wilhelmy plate method with a compression speed of 200 cm^2 min^{-1} and a continuous readout. Solubility of the surfactant in water was checked on several compression-decompression steps with waiting times of 30-120 min. The stability of the monolayer was also checked on compression until a certain pressure and left for 30-60 min. A film collapse was forced to see the reproducibility of the monolayer.

Small Angle X-Ray Scattering

Small angle X-ray scattering (SAXS) was employed to determine the structure of the mesophases. SAXS measurements were carried out at the Max-Planck-Institute in Golm (Germany) on a home-built apparatus equipped with an Fr591 rotating anode (Bruker-Nonius, Netherlands) and a MarCCD Camera (Mar 165) with a diameter of 165 mm. The sample to detector distance and the detector tilt and center were calibrated using a silver behenate standard.[159, 160] The distance between the sample and the detector was 741 mm and the detector resolution was 2048 x 2048 pixels. Samples between 30 - 95 wt% surfactant were measured using sealed capillaries ($\varnothing$ = 2 mm). The recorded two-dimensional (2D) scattering pattern was integrated to a one-dimensional scattering function *I(q)* using the ImageJ software. The result is an angle dependent scattering curve, in which q is the length of the scattering vector, defined by $q = (\frac{2\pi}{\lambda})sin(\frac{\theta}{2})$, with λ being the x-ray wavelength (CuK α 1.542 Å) and θ the scattering angle.

Viscosity Measurements

Temperature	η (90 wt% X-AES)	η (95 wt% X-AES)	η (100 wt% X-AES)
	[Pa · s]	[Pa · s]	[Pa · s]
10 °C	2.11	5.57	15.6
27 °C	0.72	1.82	4.15
65 °C	0.16	0.31	0.51

Table 2.1: Viscosity values of high concentrated X-AES samples at different temperatures.

Viscosity measurements, necessary to calculate the size of the reverse micelles, were performed using a Bohlin Instruments rheometer CVO 120 and a shear rate between 10 and 400 s^{-1}. The solutions were thermostatted at 10, 27 and 65 °C (the same temperatures used for the NMR measurements). The obtained viscosity values for the 90, 95 and 100 wt% sample at different temperatures are given in Table 2.1.

2.2.2 The X-AES/Water/Salt/(SXS)-System (Section 3.2)

Phase Diagram

Cloud temperatures of the surfactant or the surfactant/hydrotrope solutions with various salts were visually determined using 1 g samples. The surfactant stock solution had a concentration of 23 wt% active in water (equivalent to 0.18 mol L^{-1}) and was used as supplied. The surfactant/hydrotrope stock solution was prepared by adding SXS to the same 0.18 mol L^{-1} surfactant solution. A solution with a total mole ratio R (X-AES/SXS) = 0.5 was used for the experiments. Solutions with lower and higher X-AES/SXS mole ratios were also examined (between 0.1 - 0.8). However, no difference in the phase behavior after the addition of salt was observed besides a small temperature shift.

Different amounts of sodium and chloride salts were added to 1 g of the surfactant or the surfactant/hydrotrope stock solutions. Afterwards, the solutions were heated up to 80 °C, while being completely immersed in a water bath and then cooled down to 0 °C. The samples were left at 0 °C for about 15 min. Phase diagrams were achieved by visual observation of the transition from clear to turbid by heating the samples again in a water bath from 0 to 80 °C (accuracy ± 0.5 °C) with a heating rate of 2 °C min^{-1}. For precise measurements, the samples were completely immersed in a water bath and both the bath and the samples were stirred during the measurements using a magnetic stirrer.

Optical Polarizing Light Microscopy

A Leitz Orthoplan polarizing optical microscope (Wetzlar, Germany), a Linkam hot stage with a Linkam TMS90 temperature control (accuracy ± 0.5 °C) and a Linkam CS196 cooling system (Waterfield, UK) were used to conduct the microscopy experiments. Specific concentrations of salt/surfactant/water or salt/surfactant/ hydrotrope/water systems were chosen to analyze the phase transitions from clear to turbid as a function of temperature (0 to 90 °C). The different phases that appeared were determined by their characteristic optical textures under crossed polars.[39, 40] The accuracy of the transition temperatures was ± 1 °C. The heating and cooling

rates for all measurements were 2 °C min^{-1}.

NMR-Measurements

^{1}H-NMR measurements were performed using a Bruker BioSpin Avance 300 spectrometer operating at 300.13 MHz for ^{1}H resonance with a 30° pulse lengths of 7.2 μs and 64 scans. Samples were prepared by adding 30 mg of the substance, which needs to be analyzed, to 700 mg of an acetone-D_2O mixture. The content was mixed by a magnetic stirrer and transferred into NMR tubes (5 mm o. d.). The salt solutions were prepared using a 23 wt% surfactant solution made with the neat surfactant in D_2O.

Freeze-Etch Transmission Electron Microscopy (FE-TEM)

Samples used for freeze-etch (FE) experiments were frozen in liquid N_2. Freeze-etching was performed using a CFE-50 (Cressington, Watford, England) apparatus at -97 °C under a vacuum of 10^{-7} mbar for 4 min. Metal replicas were obtained by Pt/C (incident angle 45°, 1 nm) and carbon (incident angle 90°, 10 nm) shadowing onto the fracture surfaces. The replicas were examined and documented with a CM 12 transmission electron microscope (Eindhoven, Netherlands), using a slowscan 1024 x 1024 CCD camera (TViPS, Gauting, Germany).

2.2.3   The Low Oil Content - System (Section 3.3)

Phase Diagram

Nano-emulsions were prepared by adding different concentrations of sodium or chloride salts (0-20 wt% in 2 wt% steps) to a 3 g sample containing SXS (40 wt% in water), oil and surfactant (23 wt% in water). The total mass ratio of X-AES/SXS, X-AES/rapeseed oil, water/rapeseed oil and rapeseed oil/SXS was kept constant to 3.3, 1.3, 4.7, and 2.5, respectively, during all measurements. A recipe for a formulation of a nano-emulsion (with 7 wt% NaCl) was provided by the Huntsman Corporation (Texas, USA) and therefore, the same composition without salt was chosen for the phase diagrams. In the case of a clear solution at 0 °C, more salt was

added (in 2 wt% steps) until a turbid solution was obtained. The solutions were heated up to 70 °C, being completely immersed in a water bath and then cooled down to 0 °C. Phase diagrams were achieved by visual observation of the transition from clear to turbid or *vice versa*, by heating the samples in a water bath from 0 to 70 °C (accuracy ± 0.5 °C) with a heating rate of 2 °C min^{-1}. For precise measurements, the samples were completely immersed in a water bath and both the bath and the samples were stirred during the measurements using a magnetic stirrer. The appearance of liquid crystals was determined using crossed polarizers.

Time Stability Measurements

Time stability measurements were performed by heating the samples to 70 °C and cooling to 0 °C. Afterwards, the solutions were thermostatted on a self-made temperature controlled magnetic stirrer at 21 °C (without stirring). The stability of the nano-emulsions was determined by visual observation from clear to turbid or to phase separations.

Optical Polarizing Light Microscopy

A Leica Reichert Polyvar 2 polarizing optical microscope (Wetzlar, Germany) equipped with a Mettler FP82HT hot stage was used to conduct the (time dependent) optical microscopy experiments at room temperature (25 °C). Specific concentrations of the salt/surfactant/SXS/water/rapeseed oil system were chosen to conduct the experiments within the clear and turbid regions.

Temperature dependent microscopy measurements were performed using a Leitz Orthoplan polarizing optical microscope (Wetzlar, Germany), equipped with a Linkam hot stage, a Linkam TMS90 temperature control (accuracy ± 0.5 °C) and a Linkam CS196 cooling system (Waterfield, UK). Again, specific concentrations of the salt/surfactant/SXS/water/rapeseed oil system were chosen to analyze the phase transitions from clear to turbid or *vice versa* as a function of temperature (0 to 70 °C). The different phases appearing were determined by their characteristic optical textures using crossed polarizers.[39, 40] The accuracy of the transition temperatures was ± 1 °C. The heating and cooling rates for all measurements were 2 °C min^{-1}.

Conductivity Measurements

All conductometric measurements were performed using an InoLab® Cond 730 conductometer (WTW GmbH, Germany) with a TetraCon® 325 electrode (WTW GmbH, Germany). The specific conductivity of the used Millipore water was always below 3.0 μS cm^{-1}. The cell constant was periodically checked and calibrated with a 0.01 M KCl solution. A sample volume of 50 ml was used for the studies. For the measurements, the temperature was constantly increased (1-2 °C min^{-1}) from 20 to 70 °C using a Lauda C20 thermostat (Lauda GmbH, Germany). Measurements with salt concentrations of 0.53, 0.87, 1.37 and 1.97 mol/kg NaCl or 0.52 and 1.85 mol/kg NaSCN were performed.

Dynamic Light Scattering (DLS)

Droplet size analysis was performed using a Zetasizer 3000 PCS (Malvern Instruments Ltd., England), equipped with a 5 mW helium neon laser with a wavelength output of 633 nm. The scattering angle was 90°. The intensity autocorrelation functions were analyzed using the CONTIN software. Different solutions were prepared as described for the partial phase diagrams and brought into a 1.0 cm to 1.0 cm to 4.8 cm plastic cuvette. All measurements were performed at 21 °C.

2.2.4   The High Oil Content - System (Section 3.4)

Phase Diagram

Nano-emulsions were prepared by adding different concentrations of NaCl, NaSCN or NaNO$_3$ (0 - 10 wt% in 1 wt% steps) to a 2 g sample containing rapeseed oil/water (1:1 mass ratio) and surfactant (X-AES, 0.3:1 surfactant to oil/water mass ratio) or rapeseed oil/water (1:1 mass ratio), surfactant (X-AES, 0.3:1 surfactant to oil/water mass ratio), and hydrotrope (SXS, 0.05:1 hydrotrope to surfactant mass ratio). The solutions were heated to 80 °C, while being completely immersed in a water bath and then cooled back down to 0 °C. Phase diagrams were achieved by visual observation of the transition from clear to turbid or *vice versa*, by heating the samples in a

water bath from 0 to 80 °C (accuracy $\pm$ 1 °C) with a heating rate of 2 °C min^{-1}. For precise measurements, the samples were completely immersed in a water bath and both the bath and the samples were stirred during the measurements using a magnetic stirrer. The appearance of liquid crystals was determined using crossed polarisers.

Optical Polarizing Light Microscopy

Optical microscopy measurements were performed using a Leitz Orthoplan polarizing microscope (Wetzlar, Germany), equipped with a Linkam hot stage, a Linkam TMS90 temperature control (accuracy $\pm$ 0.5 °C) and a Linkam CS196 cooling system (Waterfield, UK). Specific concentrations of the salt/surfactant/water/rapeseed oil system and the salt/hydrotrope/surfactant/water/rapeseed oil system were chosen to analyze the phase transitions from clear to turbid or *vice versa* as a function of temperature (0 to 80 °C). The different phases appearing were determined by their characteristic optical textures using crossed polarizers.[39, 40] The accuracy of the transition temperatures was $\pm$ 1 °C. The heating and cooling rates for all measurements were 2 °C min^{-1}.

Conductivity Measurements

All conductometric measurements were performed using an InoLab® Cond 730 conductometer (WTW GmbH, Germany) with a TetraCon® 325 electrode (WTW GmbH, Germany). The specific conductivity of the used Millipore water was always below 3.0 μS cm^{-1}. The cell constant was periodically checked and calibrated with a 0.01 M KCl solution. A sample volume of 50 ml was used for the studies. For the measurements, the temperature was constantly increased (1-2 °C min^{-1}) from 20 to 70 °C using a Lauda C20 thermostat (Lauda GmbH, Germany). Measurements with salt concentrations of 0.37 and 0.52 mol/kg NaCl or 0.25 and 0.39 mol/kg NaSCN were performed.

NMR-Measurements

^{23}Na- and ^{2}H-NMR measurements were performed using a Bruker Avance 400 spectrometer and variable temperature probes, operating at 105.8 MHz and 61.4 MHz for ^{23}Na and ^{2}H resonances, respectively. The $\pi/2$ pulse lengths were 8.7 μs for ^{23}Na resonance and 9.4 μs for ^{2}H resonance, respectively. Temperatures were measured to be constant within $\pm$ 1 °C. Samples for NMR were prepared by weighing a total amount of 3.0 g into test tubes and homogenized by repeated centrifugation. Afterwards, the prepared samples were centrifuged again to remove air bubbles.

Chapter 3

Results and Discussion

3.1 Phase Behavior of an Extended Surfactant in Water

3.1.1 A Detailed Characterization of the Dilute and Semi-Dilute Phases

Introduction

The oil and water solubilization capacity of a microemulsion can be improved by increasing the surfactant-oil and surfactant-water interaction. The optimum solubilization can be found when the oil and water interactions are equal, which can be done by either increasing the hydrophilicity of the head-group or the hydrophobicity of the tail group of a surfactant.[1]

A new class of amphiphiles, containing both a lipophilic and a hydrophilic linker, has awaken interest for many scientists. These so-called extended surfactants (Figure 1.3), alkyl-polypropylene-oxide ether sulfates, are the most promising candidates to solubilize high amounts of vegetable oil in the continuous aqueous phase of microemulsions. It was shown by Graciaa *et al.*,[3, 5] Miñana-Perez *et al.*,[10] Salager *et al.*[3–5, 10] and Witthayapanyanon *et al.*[25, 26] that the presence of a very lipophilic amphiphilic additive improves substantially the solubilization of oils. In addition to the properties of these surfactants mentioned in Section 1.2, CMC

values can be evaluated for such a molecule as shown in Figure 2.1
(C_{12-14}-$(PO)_{16}$-$(EO)_2$-SO_4Na, X-AES). Considering that the propylene-oxide moieties have the hydrophobic character of three CH_2 groups, then this surfactant has a hydrophobic tail containing a total of ca. 60 CH_2 groups. Using the standard formulae to estimate the CMC values for monovalent ionic surfactants (CMC is lowered by a factor of 0.25 for every two CH_2 groups), the expected CMC is ca. 10^{-15} M.[17] Witthayapanyanon *et al.* used surface tension data to obtain critical micelle concentrations (CMC's) and to derive an area per molecule at the air/water interface. These values (150-200 $Å^2$) are much larger than those of conventional surfactants. The CMC of a surfactant similar to the structure in Figure 2.1, but with 14 PO groups was reported to be 80 μM with an area per molecule of 200 $Å^2$. This CMC value is much higher than what can be expected, although it is significantly lower than the CMC's of classical anionic surfactants. Further, this value is lower by a factor of 1.5 than the value for a surfactant with only 8 PO groups and no EO groups (130 μM).[25, 26]

Salager *et al.* were the first to examine the solubilization of various oils in water using extended surfactants.[10] They also reported CMC's of extended surfactants with different PO chain lengths. For the surfactant with 14 PO groups, they give a value of ca. 30 μM, but the CMC of a surfactant with 8 PO groups is only slightly higher at 100 μM. Thus, the CMC decreases by a factor of 3 between the two surfactants. Again, the CMC values are very high compared to the estimated values.

In addition, Salager *et al.* performed cloud point measurements on a 10 wt% surfactant solutions, where the cloud point decreases with increasing PO content, which is a very rare phenomenon to occur with ionic surfactants in the absence of electrolytes.[4, 10] All the experiments were aimed at obtaining an optimum formulation of oils in water. However, the neat surfactant and its behavior in water have not yet been examined.[3–5, 10, 25]

In this section, the different mesophases formed by an extended surfactant (X-AES, Figure 2.1) in water were investigated. A phase diagram covering the whole concentration range was determined using polarizing optical microscopy. The phase behavior at lower surfactant concentrations (<30 wt% X-AES) was studied with

cloud temperature measurements during several heating and cooling steps. The cloud temperature corresponds to the formation of lamellar phase droplets within the micellar phase.

The sizes of the micelles were determined by cryo-TEM and dynamic light scattering measurements. Also ^{1}H-NMR measurements were carried out for the clear solutions (prepared in D_2O) at concentrations below 30 wt% of X-AES. The changes in linewidths gave information about surfactant rotational correlation times, from which the sizes of the micelles and the lamellar phase droplets could be deduced.

Furthermore, an attempt was made to measure the CMC using surface tension measurements. The apparent value obtained was higher then expected for this kind of surfactant and similar to the results described above.[10, 25] The possibility that slow surfactant exchange between the adsorbed surface layer and the bulk solution might occur was investigated. The behavior of the X-AES monolayer at the air/water interface on a Langmuir balance was examined to investigate the occurrence of an apparently insoluble fraction of the surfactant. Finally, the effect of salt (sodium chloride) on the cloud temperature was studied for a better understanding of the mechanism of lamellar phase formation at low concentrations.

Results

a) Phase Behavior

The penetration scan described by Lawrence [122] is a rapid method to obtain information on the liquid crystals formed by surfactants in water and was already described in section 1.6. The different mesophases which appear at various concentrations can be seen as distinct rings with characteristic optical textures under crossed polars.[39, 40]

The images of the penetration scan at 18 °C (left) and at 42 °C (right) are shown in Figure 3.1.

At 18 °C, the penetration scan shows multiple separate phase rings. The phase structures assigned were, in order of increasing surfactant concentration, micellar (L_1), hexagonal (H_1), lamellar (L_α), reversed bicontinuous cubic (V_2), reverse hexagonal (H_2) and reverse micellar (L_2) with solid particles (S). The two hexagonal and the
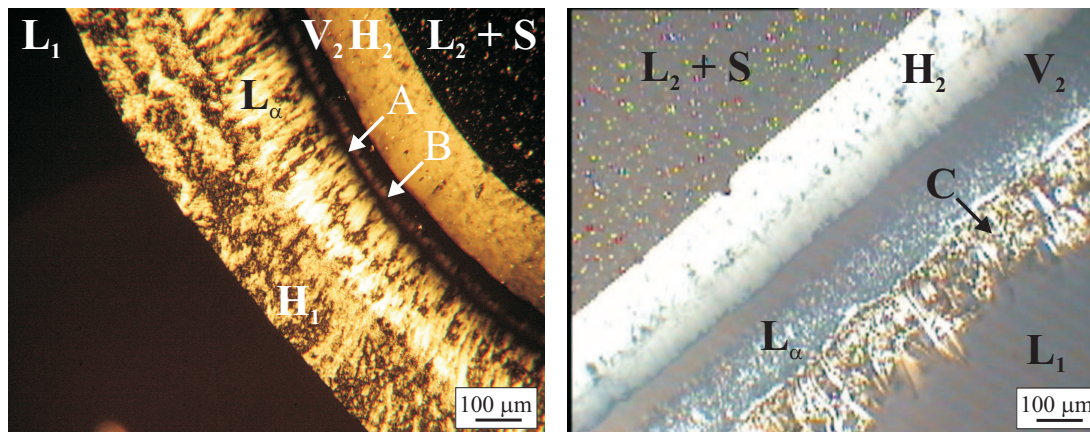
Figure 3.1: Penetration scan photograph of water into X-AES at ca. 18 °C (left) with crossed polarizers and 42 °C (right) with partially crossed polarizers. A and B are a lamellar phase with a change in birefringence (left). C describes also a lamellar phase with no sharp boundary (right). The symbols are identified in the text.

lamellar phases were identified by their relative viscosities and their textures.[39, 40] All measurements were reproduced over several heating and cooling cycles. It should be noted that the results slightly depend on the measurements for the surfactant batch number used, where the temperatures can vary between $3 - 5$ °C.

Although most of the phases were easy to identify because the textures were commonly observed, it was more difficult to assign the region between the lamellar and reversed cubic phases, where a faint birefringent line (B) occurs within an isotropic zone (A). This phase occurs over the whole temperature range. It results from the occurrence of a lamellar phase region where the birefringence goes to zero (see below).

The penetration scan at 42 °C does not show the hexagonal phase between L_1 and L_α observed at lower temperatures (Figure 3.1, right). Instead, the lamellar phase contacts L_1 directly. The two phases have an irregular boundary rather than the smooth L_1/H_1 boundary and is identified as (C) in Figure 3.1 (right). The irregular boundary has some similarity to the myelins commonly observed for low molar mass surfactants. However, all the other phases which appear at 18 °C could be observed at this temperature (Figure 3.1, right). The two regions (A) and (B) were also observed, but can be seen for the sample in Figure 3.1 (right) only at higher magnifications and with fully crossed polars.
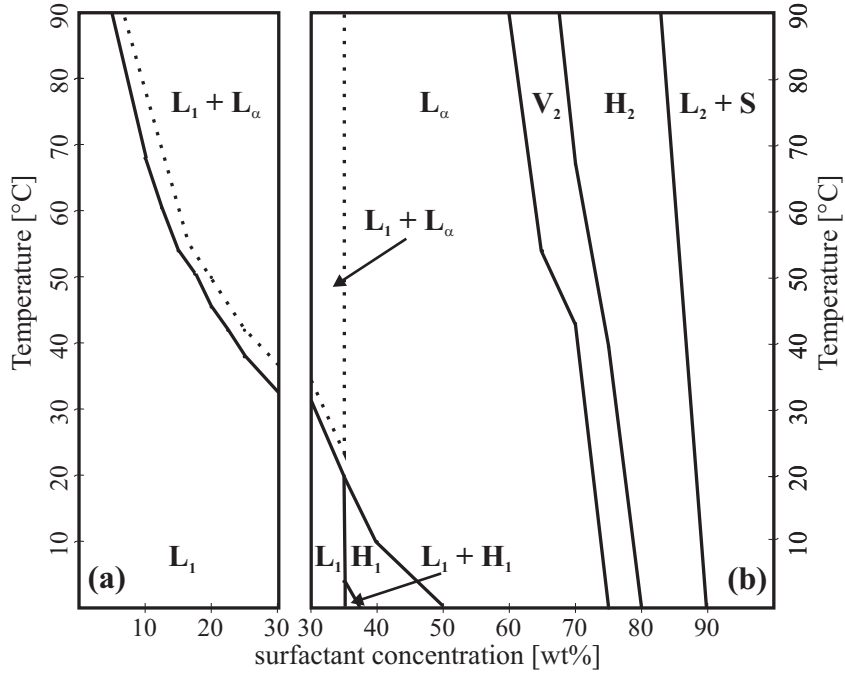
Figure 3.2: Schematic phase diagram of the extended surfactant X-AES/water system. The left side (a) shows the measurements in H_2O and the right side (b) the measurements in D_2O. L_1 is a micellar solution, L_2 is an isotopic liquid phase, and H_1, L_α, V_2, and H_2 are liquid crystals described in the text. S is a solid phase.

For the construction of a more detailed phase diagram, bulk samples with concentrations in the range of 5.0-95.0 wt% of surfactant were observed over heating and cooling cycles using crossed polarizers to identify the birefringent phases. In addition, these samples were also examined with temperature dependent optical microscopy. The resulting schematic phase diagram is shown in Figure 3.2 and is in agreement with the penetration scan. Measurements (except for ^{1}H-NMR) on samples with < 30 wt% of X-AES were performed using ^1H_2O as solvent (Figure 3.2a) and above this concentration the solvent was D_2O (^2H_2O, Figure 3.2b). The results are separated in two parts of the phase diagram.

A "clouding" phenomenon was observed when micellar solutions with > ca. 5 wt% surfactant were heated, despite the non-occurrence of any liquid-liquid partial miscibility in the penetration scan (as is commonly observed for polyoxyethylene nonionic surfactants with a cloud point). The clouding temperature was recorded by visual observation on different heating and cooling steps and is shown in Figure 3.2 as a solid line between 5 and 30 wt%. The dotted line above these temperatures

represents the appearance of droplets of lamellar phase as confirmed with polarizing microscopy. This lamellar dispersion probably appears already at the transition temperature from clear to turbid; however, the droplets were too small to be seen under the microscope. This two-phase region turns into a single lamellar phase at higher temperatures. Note that the cloud temperature decreases sharply as the surfactant concentration increases. This behavior is very different from that of nonionic surfactants, even polymeric ones, and is discussed further below.

At the lowest temperatures, an H_1 phase is formed at the L_1 phase boundary rather than L_α. This is only stable up to a maximum at ca. 20 °C for a 35 wt% X-AES solution. However, at this temperature and concentration a two-phase region of H_1/L_α exists. Below 4 °C a two-phase region can also be observed for the same sample, consisting of a H_1 and a L_1 phase. This region could not be seen for any sample with > 35 wt% surfactant. Heating up the different samples of the H_1 phase leads to a single lamellar phase. Above 50 wt% of X-AES, only the lamellar phase occurs and the region extends up to ca. 65-70 wt% over the whole temperature range.

To see the lamellar phase with its Maltese crosses at concentrations between 60 and 75 wt%, more and more light intensity was necessary. In this region, the lamellar phase loses intensity until almost no birefringence can be seen. This is in agreement with the first dark ring in the penetration scan (Figure 3.1). A similar phenomenon was already observed by Rogers and Winsor in 1969 for the Aerosol-OT/water system.[161] An optically isotropic region was found within the lamellar phase. They demonstrated that this arose because the birefringence changed sign from positive to negative on increasing water content. It seems highly likely that a similar explanation holds here. Hence, there is one composition where the ordinary and extraordinary refractive indices are equal.

By further increasing the concentration of surfactant, the bicontinuous cubic, reverse hexagonal, and finally the liquid surfactant phase (L_2, probably an inverse micellar solution) with particles (S) can be found, as observed with the penetration scan.

The solid particles in the neat surfactant were also studied by optical microscopy and may be inorganic substances (e.g. Na_2SO_4). Several cooling and heating cycles could show that the particles dissolve at temperatures around 150 °C and do not reappear

again after dissolution. However, these particles also appear at 5 and 10 wt% water. At these concentrations, electrolytes should be dissolved in the water or at least a smaller amount should appear. However, the contrary was observed, the amount of particles seemed to increase with increasing water amount. A more detailed description of the phases above 30 wt% X-AES and of the solid particles will be given in the next section.

b) Micellar Solution
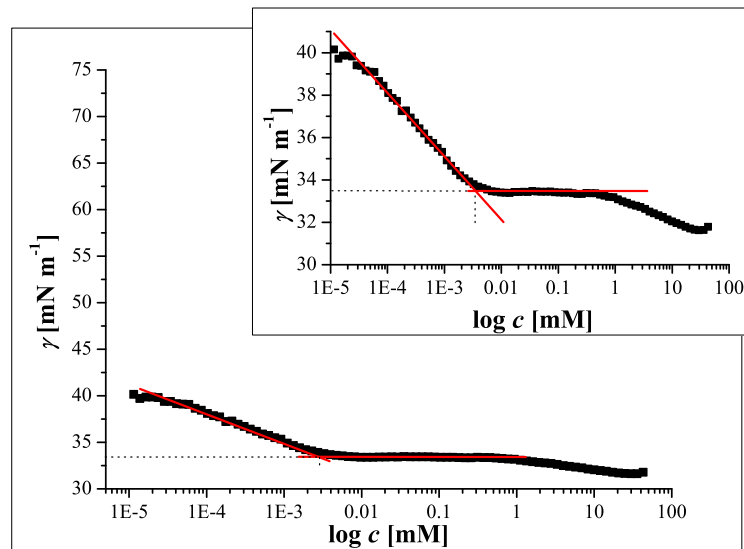
Figure 3.3: Surface tension of X-AES versus concentration at 25 °C, measured by dilution of a 5 wt% surfactant solution.

In the L_1 region of the phase diagram at lower concentrations, a micellar solution can be observed. The CMC of the surfactant was investigated by surface tension measurements (Figure 3.3). These show a decrease in surface tension with increasing surfactant concentration and reach a plateau at the apparent CMC (2.9×10^{-6} M), which is similar to that of conventional non-ionic surfactants. At this point, the surface tension (γ) is constant until it slightly decreases again at the highest surfactant concentrations. Note that γ at the lowest surfactant concentration is well below the value for water (72.8 mN m^{-1}). In repeated cycles, the concentration was reduced
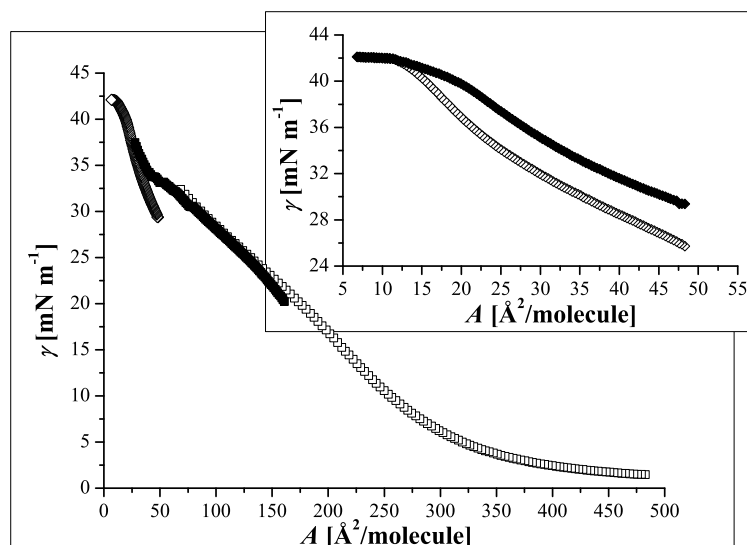
Figure 3.4: (π-A) isotherm of a 2.5 mg/mL solution and different volumes: $\square$ 10 μL, $\blacksquare$ 30 μL, $\diamond$ 90 μL at room temperature. The insert shows the same isotherm with 90 μL: $\blacklozenge$ first compression; $\diamond$ second compression, after opening the barriers again.

to below 10^{-5} mM, but no significant increase in γ was observed. Although this CMC value is similar to literature values for polymeric surfactants, it is higher by many orders of magnitudes than the value expected for an ionic surfactant with the equivalent of ca. 60 CH_2 groups (10^{-15} M). Hence, we investigated the stability of the X-AES monolayer at the air/water interface using a Langmuir-Blodgett trough. Several (π-A) isotherms for X-AES are given in Figure 3.4, showing that a significant surface pressure can be observed even for very large A values (> 400 Å^2/molecule). The pressure already increases to 1 mN m^{-1} just 30 min after spreading only 10 μL (Figure 3.4, $\square$) of the initial 2.5 mg/mL solution onto the interface. Further compression of the monolayer leads to an increase in pressure until a slight change in the curve appears (ca. 120 Å^2/molecule). The layer formed can be further compressed until ca. 7 Å^2/molecule. This clearly demonstrates that the exchange between the X-AES in the bulk solution and that in the surface is very slow. To obtain these results, different volumes of the initial solution were necessary because of the small area of the trough (30 ($\blacksquare$) and 90 μL ($\diamond$), Figure 3.4). After the barriers were opened and closed again, a decrease in pressure at the beginning
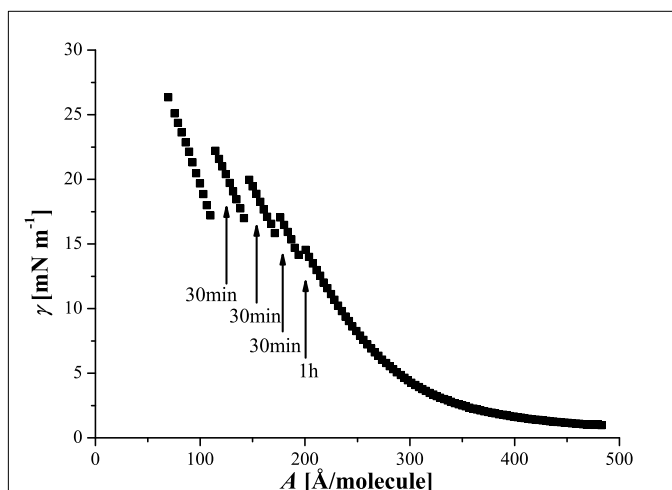
Figure 3.5: (π-A) isotherm of a 2.5 mg/mL surfactant solution. The arrows indicate the different stops and the times until the next compressions.

of the isotherm could be observed (see insert, Figure 3.4). This decrease indicates a loss of molecules at the surface. Nevertheless, the same pressure of ca. 42 mN m^{-1} could be observed again at 12 Å^2/molecule.

For a better understanding of the mechanism, an isotherm was recorded where the barriers were stopped at certain pressures for various times (Figure 3.5). It could be seen that at lower pressures a small loss of molecules from the surface appears, while a large loss appears at higher pressures and shorter time. This effect is an indication for limited water solubility of the surfactant at the beginning and the very slow solubilization kinetics. On adding a small amount of the neat surfactant to the air/water interface of the Langmuir trough, an increase in surface pressure to 39.5 mN m^{-1} is observed, the same as that for the compressed monolayer in Figure 3.4. Despite the ultra low interfacial tension of the extended surfactant, the added drop was swimming on the air/water interface. The transfer energy, which is necessary for the molecules to go into the bulk and form micelles, is high. Therefore, the molecules prefer to spread on the subphase with their long hydrophobic tails in the air. All of the samples in the clear L$_1$ region were of rather low viscosity, being readily pourable. Hence, there were no obvious signs that long rod-like micelles were present, even in solutions adjacent to the hexagonal phase. The micellar solution at

wt% X-AES	Temperature [°C]	Radius [nm]	PDI
1.0	10	1.2	0.932
	15	1.4	0.812
	20	1.2	0.73
	25	1.2	0.694
	30	1.3	0.587
5.0	10	1.0	0.354
	15	1.1	0.326
	20	1.1	0.315
	25	1.1	0.345
	30	1.1	0.345

Table 3.1: Micelle radii and polydispersity index for the DLS measurements of a 1.0 and 5.0 wt% surfactant solution at different temperatures.

low concentrations was studied by cryo-TEM and dynamic light scattering (DLS) to obtain the size and the shape of the micelles. DLS measurements between 0.1 and 5.0 wt% show a constant hydrodynamic radius over a wide concentration range of about 1.2-1.5 nm (Table 3.1). However, the polydispersity index (PDI) appears to be very high, so the data should be treated with caution. Even so, it can be concluded that the radius of the micelles is very small compared to the maximum extension of the surfactant (on average ca. 8 nm).
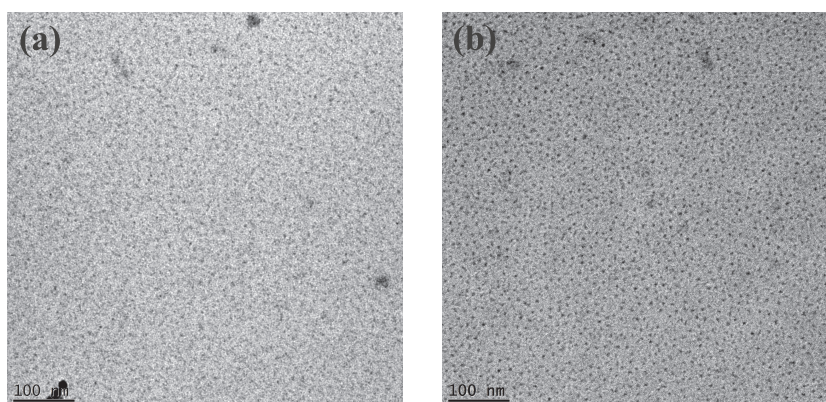
Figure 3.6: Cryo-TEM photograph of an aqueous solution of X-AES with a total surfactant concentration of 1.0 wt% (a) and 5.0 wt% (b). Globular micelles can be seen.

The cryo-TEM photographs in Figure 3.6a and b show that only small globular
"potato-like" micelles with a radius of about 2.5-7.0 nm at low surfactant concen-
trations (taken from the larger spots) were formed. The contrast in the image comes
from the hydrophobic chains (black blobs), while the head-groups and water appear
to be the same. Similar images were observed for the other concentrations examined.
The size is in agreement with the DLS measurements, considering the fact that at
the high magnification employed it is very difficult to obtain a sharp image of the
sample. There was no evidence for the formation of long rod-like micelles.

Further measurements of the micellar solutions were made using ^{1}H high resolu-
tion NMR. It is well known that sharp resonances are observed for small micelles,
while broad peaks occur for long rod micelles. Proton NMR spectra were recorded
for solutions in D_2O over the concentration range 1-35 wt% and the temperature
range 10-90 °C. A typical spectrum of a 20 wt% surfactant solution is shown in
Figure 3.7. The first peak in the spectrum is from the terminal CH_3 group of the
alkyl chain (Figure 3.7, a). The remaining peak assignment was carried out using
readily available standard chemical shift data.[162]
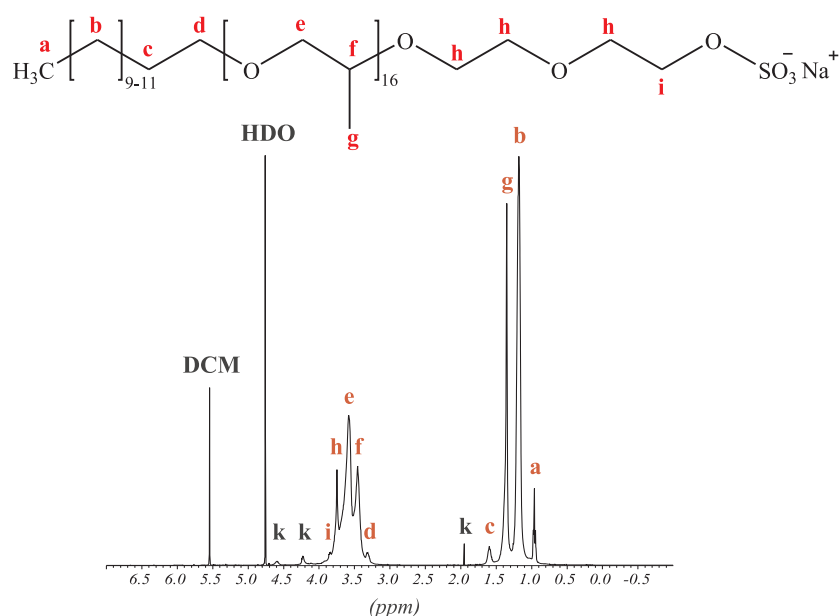
Figure 3.7: ^{1}H-NMR spectra of a 1.0 wt% X-AES solution in D_2O at 27 °C. The peaks are
labeled in the structure above. DCM is dichloromethane and (k) are impurities.
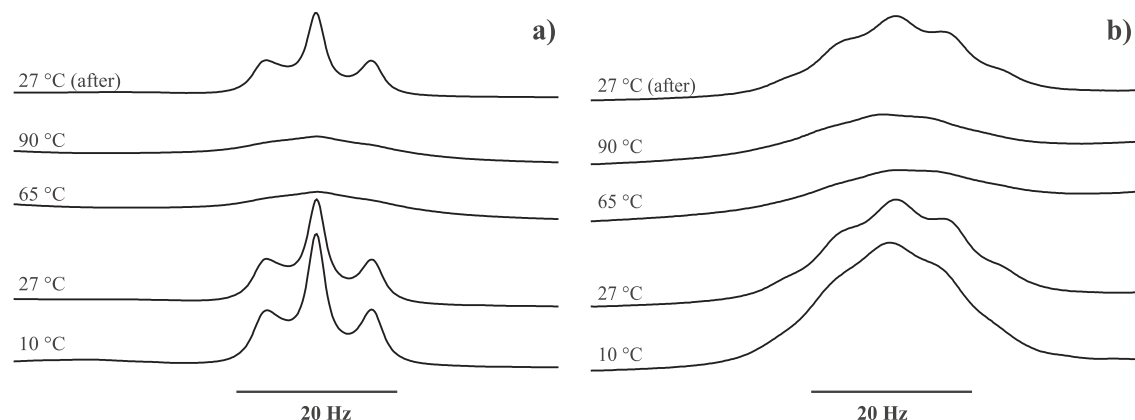
Figure 3.8: (Sequence of ^{1}H-NMR spectra of a 20 wt% surfactant solution at different temperatures. (a) Terminal CH_3 group (peak (a) in Figure 3.7); (b) β-CH$_2$ of the alkyl chain (peak (c) in Figure 3.7

To illustrate the changes in linewidths, peaks corresponding to a single group of protons that are well separated from other resonances were selected. For these, the peaks a) and c) in Figure 3.7 were chosen. Representative spectra for these resonances of a 20 wt% X-AES solution at different temperatures can be seen in Figure 3.8. The terminal methyl peak (Figure 3.7, a) appears as a triplet due to scalar J coupling from the adjacent CH$_2$ group, while the peak from the β-CH$_2$ protons (Figure 3.7, c) is a quintet due to scalar J coupling from the two adjacent CH$_2$ groups. They show indications of line-broadening at higher temperatures for all the samples, and close to the mesophase boundaries for the higher concentrations.

All of the measurements on the L$_1$ phase suggest that it contains fairly small "potato-like" micelles over the whole temperature range. The increase in linewidth can be used to estimate the size of the micelles because it arises from incompletely averaged ^{1}H-^{1}H dipole-dipole coupling. The approach of Staples *et al.* was employed, who used the line-broadening to estimate the sizes of sodium dodecylsulfate micelles in the presence of electrolyte and octanol.[163] The molecular motions of the surfactant are divided into two classes, each with a specific correlation time (τ_c). The fast local motions (random diffusion, conformational changes etc.) are described as fast (τ_c^f), while the diffusion around the micelle is slow (τ_c^s). For a surfactant of chain length n, each proton can have dipole-dipole interactions with *2n+1* other protons, but the major coupling is between protons on the same carbon. This is

proportional to the order parameter (S). From previous measurements on lamellar phases, the order parameter S of the terminal CH_3 group was estimated to be 0.01 and of the β-CH_2 group to be 0.05.[164–166] Using the calculations made by Staples *et al.* and with the help of Figure 1 in reference [163], the rotation relaxation time τ_c^s can be calculated. Considering that the rotation relaxation time is equal to three times the measured NMR relaxation time, then:[167]

$$\tau_{rot} = 3\tau_{NMR} \tag{3.1}$$

And considering that the volume of a micelle (V_0) is similar to that of an equivalent sphere, then the size can be calculated using the Stokes-Einstein equation:

$$\tau_{rot} = \frac{3V_0\eta}{kT} \tag{3.2}$$

$$r = \sqrt[3]{\frac{\tau_{NMR}4kT}{\pi\eta}} \tag{3.3}$$

where η is the viscosity of water at different temperatures, τ_{NMR} is the measured relaxation time, τ_{rot} is the calculated rotation relaxation time, k is the Boltzmann constant and T is the temperature. The calculated radii at different temperatures as a function of the surfactant concentration are shown in Figure 3.9.
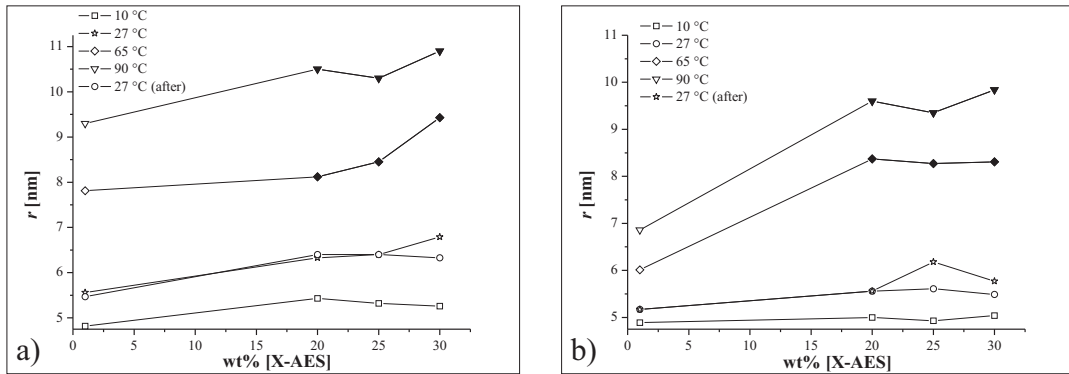
Figure 3.9: Calculated radius from the linewidth against the surfactant concentration at different temperatures: (Left) terminal CH_3, (right) β-CH_2. The filled symbols are measurements within the lamellar phase.

Given the very approximate estimates of the order parameters, these values must be considered with caution. However, a small increase in the size of the micelles with concentration can be observed at 10 °C. Compared to the other temperatures, the sizes remain almost constant at ca. 5 nm. The radii at 27 °C are larger and also increase with surfactant concentration. After a heating cycle (cooling to 10 °C, heating to 90 °C and again cooling to 27 °C, ca. 4 h), the size of a micelle at 27 °C is approximately the same as before. Considering the long equilibration times between the measurements, it can be concluded that micelle fusion rather then micelle exchange is a likely mechanism for the L_1/L_α transition.[168] At 65 and 90 °C, the increase of the radii is more pronounced with increasing surfactant concentration. In addition, the radius also increases between the two temperatures from ca. 8 nm to ca. 10 nm. A general increase in radii of ca. 3-5 nm happens between 10 °C and 90 °C. A size range between 5 and 10 nm is also observed by the ^{1}H-NMR measurements, which is in agreement with the sizes obtained with cryo-TEM and DLS.

c) Effect of Salt
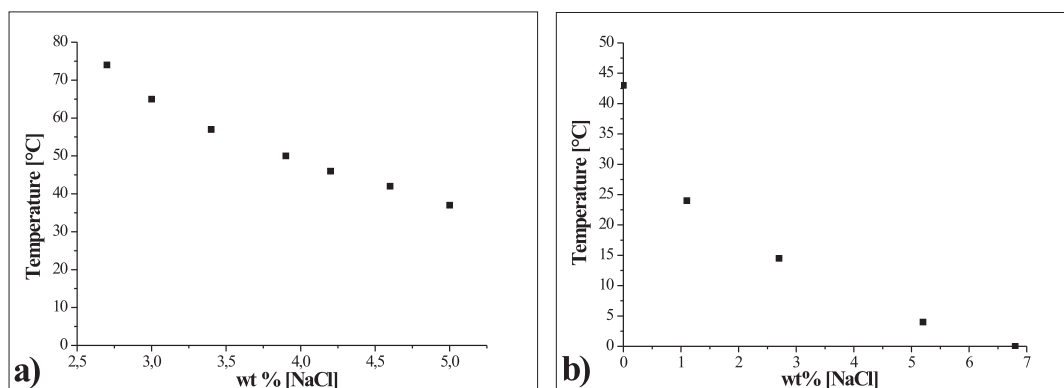
Figure 3.10: Effect of NaCl on the clouding of a 1 wt% (a) and 25 wt% (b) solution.

The effect of added NaCl on the clouding (L_1/L_α transition) of a 1 wt% and a 25 wt% surfactant solution was studied to determine the extent to which the increase in electrolyte level from surfactant counter-ions influenced the lamellar phase formation. The data are shown in Figure 3.10a and b. At both concentrations, NaCl has

a "salting-out" effect on the extended surfactant. Note that for 1 wt% surfactant a minimum added NaCl concentration of > 2.5 wt% is required for clouding below 80 °C. To obtain clouding at ca. 45 °C (the cloud temperature for 25 wt% X-AES) ca. 4.5 wt% added NaCl is required. This is equivalent to ca. 0.8 M NaCl, which is far higher than the counter-ion concentration for 25 wt% X-AES (ca. 0.1 M), particularly if ca. 70% are bound through electrostatic forces (0.03 M). Thus, the clouding is driven mainly by intra-micellar forces, with a small contribution from inter-micellar effects.

Discussion

a) Micellar Solution

All of the measurements on the L_1 phase suggest that it contains small "potato-like" micelles over the whole temperature range. Using the radii derived from the cryo-TEM images, the aggregation numbers (N_{mic}) and the area per molecule (a) an be estimated. Assuming that the micelles are spherical and the density of the hydrophobic region is similar to that of a liquid with the same chemical composition as the hydrophobic tail. The head-group is assumed to have the same density as water, where it resides. The volumes of the molecular fragments were calculates as:[169, 170] CH_3 = 54.3 Å^3; CH_2 = 27 Å^3; and $-O-CH_2-CH(CH_3)-$ = 92 Å^3. Hence, the hydrophobic group has a molecular volume of 1877 Å^3. Assuming hydrophobic core radii of 2.5-7 nm, N_{mic} can be estimated to be in the range of 35-770 with a = 80.4-224.4 Å^2.[14, 16] This range of a values is mostly far larger than would normally be expected for the ($-OCH_2CH_2OSO_3-$) head-group (ca. 60-70 Å^2).

b) Mechanism of the L_1/L_α Phase Transition

The phase diagram indicates two routes for the formation of the lamellar phase from a micellar solution. The first route, for temperatures < ca. 20 °C, requires an increase in surfactant composition and passes through a hexagonal phase. This is the very common route seen for numerous anionic surfactants.[17] With increasing concentration, small micelles are transformed to rods, which become ordered in the hexagonal phase. The hexagonal/lamellar transition occurs when the effective

volume fraction of the surfactant exceeds the maximum that can fit into hexagonally-packed rods. The second route involves raising the temperature at constant surfactant composition, with the transition temperature decreasing with concentration. This requires a transition from small micelles to lamellae, without going through the rod micelle stage. It suggests that the micelles are oblate (rather than prolate) spheroids close to the lamellar phase. Obviously, the transition requires a reduction in aggregate curvature. As the curvature is reduced, there is an abrupt increase in N_{mic}, with very large aggregates (say $N_{mic} >> 1000$) being formed to give vesicles and/or bilayer sheets. For conventional non-ionic surfactants, this is achieved with a decrease in a due to dehydration of the EO groups on increasing temperature. Such a decrease is very unlikely to occur with ionic head-groups because conventional surfactants show no evidence of a large change in head-group area with temperature. Hence, there must be a decrease in the intra-micellar curvature because the inter-head group repulsions are reduced or because the hydrophobic tails adopt more disordered configurations. A major contribution from inter-micellar repulsions, occurring as the concentration is increased, can be discounted from the behavior of cloud temperatures in the presence of added NaCl. Thus, the transition is driven by a decrease in the intra-micellar curvature. Hence, the decrease in curvature could arise from an increased repulsion between the hydrophobic groups with increase in temperature. The PO chains become more extended at higher temperatures because they access a wider range of configurations. A recent study [30] of the effect of temperature on the optimum salinity for microemulsion formation with extended surfactants has presented data that are consistent with a small decrease of surfactant hydrophilicity with increasing temperature. This was attributed to a dehydration of PO groups with increasing temperature, an alternative explanation. Note that these studies are carried out with added inorganic electrolyte (NaCl) where the ionic strength is much larger than in the samples investigated in this case, particularly for concentrations of < 30 wt% surfactant. Thus, the effects of long range electrostatic repulsions on the micelle curvature (which favor positive micellar curvature) will be much smaller than in this system. Yet the change in curvature in this studied system appears to be larger, requiring a larger temperature dependent cause than

in microemulsion systems.

c) CMC Measurements and Monolayer Behavior

The CMC of a surfactant is a well-defined concentration. Below the CMC, the surfactant is dissolved as monomers, and above the CMC, all additional surfactant forms micelles. This argument also applies to mixed surfactants, but is more complicated because the CMC is determined by all the individual CMC's of the pure compounds and their amounts in the mixture. X-AES (Figure 2.1) is an industrial product and contains homologues with different chain lengths. The CMC is determined mainly by the long hydrocarbon chain surfactant fraction, and minor constituents can influence the CMC because of the strong dependence of CMC on hydrocarbon number. Nevertheless, considering only the structures with 16 PO groups and not more, an approximate CMC can be calculated. Numerous studies on conventional surfactants lead to a logarithmic relationship between the CMC and the alkyl chain, as follows:

$$log(CMC) = An + B \tag{3.4}$$

n is the alkyl chain number, A and B are constants. In this case, the constant A is 0.3,[17] and the constant B can be estimated from the measured value of the CMC for, e.g. a C_{14} ionic surfactant (say 10^{-4} M). This means that the CMC for the extended surfactant X-AES decreases by a factor of 0.25 for every two additional CH_2 groups and should be 10^{-15} M. Considering the same calculations for the extended surfactant used by Salager and Sabatini with 14 PO groups, then their CMC must be approx. 10^{-13} M.[10, 25] Thus, the CMC values measured by surface tension seem to be much too high.

Taking a closer look at the results from the Langmuir balance, it was shown that the surfactant is able to perform an insoluble monolayer at the air/water interface. Despite the fact that the surfactant is water-soluble, the exchange between the interface and the bulk solution is very slow. When surface tension measurements are used to determine the CMC, it is assumed that equilibration between bulk and surface species is fast (say < 10 min). As the concentrated surfactant solution

is diluted, micelles disintegrate to provide the additional monomers required to maintain an almost constant monomer concentration. When micelles are no longer present, the monomer concentration decreases with dilution and hence, the surface tension increases. If the micelle disintegration rate is too slow, then the surface tension will show an increase, even above the CMC. It is well established that the lifetime of a monomer in a micelle (τ_{mon}) increases as the CMC decreases, as does the micelle lifetime (τ_{mic}) [$\tau \approx$ f(1/CMC)]. For conventional surfactants with a CMC of 10^{-2}-10^{-4} M, the micelle lifetime is $\tau_{mic} \approx 10^{-2}$ s. Once the CMC is reduced to 10^{-8} M, the micelle lifetimes are on the order of hours. For lower CMC values, the lifetimes are likely to be much longer, but experimental measurements are impossible at present. However, with the estimated CMC value above, the micelle lifetimes are expected to be substantial. In fact, the increase observed in surface tension on dilution is due to the solubility of a small fraction of the most hydrophilic components (short hydrocarbon/PO chains oligomers with relatively high CMC's) present in the used surfactant X-AES. These occupy the surface at high concentrations because they have a low molar mass and they diffuse to the surface the most quickly. Similarly, they are the fraction that desorbs the most readily from the surface on dilution. The sharp increase in surface tension on dilution is not an indication that the concentration is below the CMC of the majority of the surfactant. Similarly, the CMC measurements reported by others are likely to be due to the same phenomenon. Indeed, caution against the use of surface tension measurements to obtain the CMC values of polymeric surfactants, where no Langmuir trough measurements have been made, is necessary.[10, 25, 171, 172] It is probable that many of the literature reports give CMC's that are much too high, representing the behavior of the most soluble fraction rather than the CMC.

Concluding Remarks

Alkyl polypropylene oxide ether sulfates, so called extended surfactants, are found to exhibit different mesophases in water. For the surfactant used in this work, six phases were observed: a micellar (L_1), a hexagonal (H_1), a lamellar (L_α), a cubic (V_2), a reverse hexagonal (H_2), and an isotropic liquid phase (L_2) containing solid

particles (S). All of the phases showed the typical optical textures under crossed polarizers. The structure of the micellar solution was determined using different methods. In addition, two ways of liquid crystal formation could be found. The first analysis showed a transition from micellar to hexagonal that appeared by increasing the concentration. The transition is due to a change in the shape of the micelles from small spheres, to small rods, and finally into a hexagonal phase. A second route could be found by increasing the temperature above the clouding of the surfactant. In this case, a transition from micelles to a lamellar phase appeared without going through a rod-like state. This phenomenon was explained by a reduction of the curvature of the micelles. This reduction would also lead to an extreme increase in N_{mic}, and large aggregates would be formed (bilayer or vesicles). The decrease of the curvature was explained to arise from a change in intra-micellar curvature. Thus, the effect is due to a disordered conformation of the PO groups. Furthermore, it could be shown that anionic extended surfactants show both ionic and non-ionic properties. The structure of the micelles was determined using various techniques, which gave very similar results. There was no abrupt change in the size of the micelles observed. By raising the temperature or the concentration, the size increases by ca. 5 nm (maximum), which leads to an increase of the aggregation number and the area per molecule. This result is in agreement with the appearance of the lamellar or hexagonal phase, which must lead to a slight change in size. The effect of salt was studied via a cloud point shifting, and a "salting-out" effect of NaCl on the surfactant could be observed. Furthermore, it was shown that small amounts of salt have almost no influence on the phase behavior of the extended surfactant. Thus, the clouding is driven by intra-micellar forces with a small contribution from the inter-micellar effects. In addition, an attempt was made to determine the CMC of the extended surfactant by surface tension measurement. Compared to calculated values, the obtained experimental CMC was much too high. The increase in surface tension on dilution is due to solubility of small amounts of the most hydrophilic compounds in the solution. Thus, the determination of the CMC by surface tension measurements must be handled with caution and should be supported by Langmuir trough measurements.

3.1.2   A Detailed Characterization of the Concentrated Phases

Introduction

In the last section, the dilute and the semi-dilute part of the phase diagram (0-30 wt%) of the chosen extended surfactant X-AES (C_{12-14}-$(PO)_{16}$-$(EO)_2$-SO_4Na, Figure 2.1) in water was described. A micellar solution with "potato-like" micelles was observed at low surfactant concntrations. In addition, two ways of liquid crystal formation from the micellar solution were found. The first route describes a transition from a micellar to a hexagonal or a lamellar phase by increasing the surfactant concentration. The second route showed a transition from a micellar to a lamellar phase by increasing the temperature. A cloud-point was observed for the micellar solution, which corresponds to the formation of a lamellar phase. Furthermore, it could be shown that very small amounts of electrolyte have nearly no influence on this behavior. Thus, it could be concluded that the clouding of the surfactant is driven by intra-micellar forces. Importantly, it was demonstrated that the surfactant forms insoluble monolayers at the air/water surface. Hence, the determination of CMC values by surface tension measurements is invalid. Reports of CMC values for long chain surfactants should be treated with caution.

In this section, the high concentration part of the phase diagram (30-100 wt%) will be examined. Optical microscopy was used to analyze the different phases formed and to obtain the phase transition temperatures. ^{2}H- and ^{23}Na-NMR spectra were recorded for various samples in the hexagonal (H_1), lamellar (L_α), bicontinuous cubic (V_2), reverse hexagonal (H_2), and the surfactant liquid (L_2) region at different temperatures, whereas ^{1}H-NMR was used to determine the structure of the inverse isotropic solution (L_2). Furthermore, small angle X-ray scattering of the phases was performed to support these results and to give the dimensions of the aggregates.
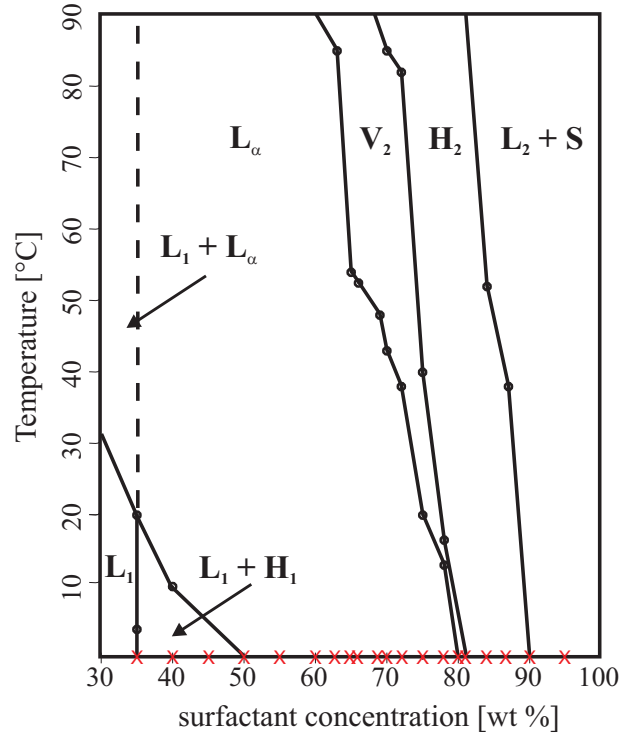
Figure 3.11: Phase diagram of the extended surfactant X-AES in D_2O. L_1 is a micellar solution, L_2 is an isotropic liquid phase (reversed micelles), and H_1 (hexagonal), L_α (lamellar), V_2 (bicontinuous cubic), and H_2 (reverse hexagonal) are liquid crystals described in the text. S is the solid phase. $\bullet$ shows the measured transition temperatures for the different mesophases. The dotted line represents a boundary not accurately determined. The red x symbolizes the compositions used for NMR measurements.

Results

a) Optical Microscopy

 A phase diagram from optical microscopy and the other measurements of the extended surfactant X-AES above 30 wt% of surfactant in D_2O is shown in Figure 3.11. The different phases observed using the penetration scan technique (see Figure 3.1) were a micellar (L_1), hexagonal (H_1), lamellar (L_α), reversed bicontinuous cubic (V_2), reverse hexagonal (H_2), and reverse micellar solution (L_2) with solid particles (S). The two hexagonal and the lamellar phases were identified by their relative viscosities and their textures.[39, 40] Typical optical micrographs are shown in Figure 3.12. The transition temperatures between the different mesophases were also determined by optical microscopy using the same concentrations and samples as used for the NMR measurements ($\bullet$ in Figure 3.11). Therefore, more transition
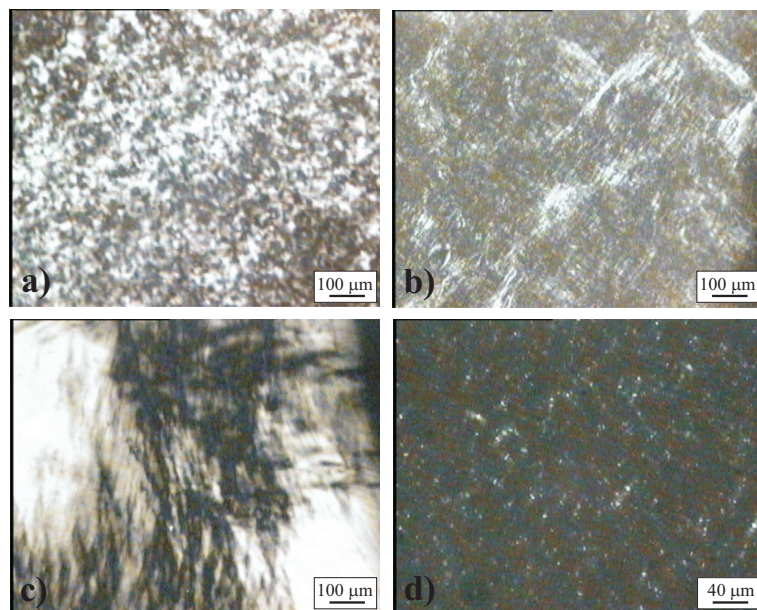
Figure 3.12: Photographs of the textures of the various mesophases at different concentrations and temperatures with crossed polarizers. (a) 35 wt% X-AES at 2 °C, hexagonal; (b) 45 wt% X-AES at 20 °C, lamellar; (c) 80 wt% X-AES at 20 °C, reverse hexagonal; (d) 95 wt% X-AES at 20 °C, isotropic solution with solid particles.

points were achieved compared to the phase diagram in the last section. Before and after the phase transition from L_α to V_2 or from V_2 to H_2, a short two-phase region may appear. However, due to great difficulties in detecting the first occurrence of these regions with the optical microscope it is not displayed in the phase diagram. Typically, these regions were less than 2 wt% and less than 10 °C wide.

As already mentioned, the hexagonal phase appears at low temperatures for a short concentration range (Figure 3.12a) arising from a micellar solution containing rod-like micelles. Increasing the temperature or the concentration, a lamellar phase is observed (Figure 3.12b). This lamellar phase becomes difficult to identify between 60 and 75 wt%, where more and more light was necessary to observe the textures. In this region, the lamellar phase textures lose intensity until almost no birefringence can be seen. This phenomenon was compared to a similar effect observed by Rogers and Winsor and was already discussed in the last section.[161] On increasing the concentration of the extended surfactant to 72 wt%, a bicontinuous cubic phase appears until 81 wt%, which turns into a reverse hexagonal phase by either increasing the temperature or the concentration. Figure 3.12c shows the reverse hexagonal

phase, which remains until 87 wt% and turns then into a liquid surfactant phase containing solid particles (reverse micellar, L_2; Figure 3.12d).

b) NMR Measurements
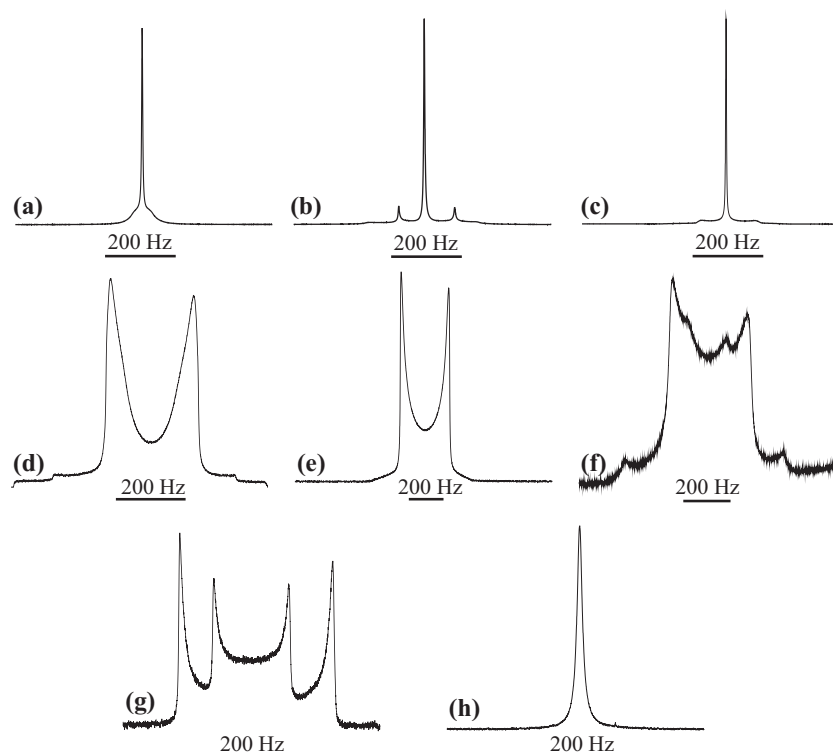
Figure 3.13: Typical ^{2}H-NMR spectra of different X-AES concentrations in D_2O: (a) 40 wt% X-AES at 10 °C ($H_1 + L_1$); (b) 40 wt% X-AES at 27 °C ($L_\alpha + L_1$); (c) 40 wt% X-AES at 90 °C ($L_\alpha + L_1$); (d) 55 wt% X-AES at 65 °C (L_α); (e) 60 wt% X-AES at 30 °C (L_α); (f) 63 wt% X-AES at 65 °C (L_α); (g) 80 wt% X-AES at 90 °C (H_2); (h) 95 wt% X-AES at 27 °C (L_2).

NMR studies on the mesophases were made using deuterium (^{2}H) and sodium (^{23}Na) resonances. A detailed description of the theory of this measurement is given in section 1.6. The deuterium and most of the sodium measurements were performed at 10, 27, 65, 90, and 27 °C again with equilibration at each temperature for one hour. To obtain more precise results for the hexagonal phase (H_1), temperature measurements between 0-10 °C in 3 °C steps were realized.

Figure 3.13 illustrates various spectra observed for different surfactant concentrations in the composition range of 40-95 wt% at different temperatures. The NMR

spectra are typical for lyotropic mesophases. However, it needs to be mentioned that the used surfactant X-AES is a multi component system (polydisperse) and thus, the phase diagram is not expected to behave exactly according to the phase rule for a two component system.

A hexagonal phase is observed at lower surfactant concentrations (40 wt%) and low temperatures (1-10 °C). However, a single peak, which is typical for an isotropic solution (L_1), appears in every spectrum for the H_1 phase and the quadrupole splittings are poorly resolved (see Figure 3.13a). On increasing the temperature, a well resolved doublet for the lamellar phase (L_α) is observed for the 40 wt% sample until 90 °C. In addition, a single peak for the L_1 phase occurs indicating a two phase system in every spectrum (Figure 3.13b, c).

At higher concentration (45 wt%), the lamellar phase occurs over the whole temperature range, also containing a single peak of an isotropic solution. The intensity of the L_1 phase decreases with increasing surfactant concentration; thus, the 50 wt% sample is almost all lamellar above 27 °C. Integration of the intensities of the L_1 and the L_α phase from the spectra was possible to estimate the compositions of the surfactant within the isotropic solution and the liquid crystal. As a result, the relative amounts of surfactant in the L_1 phase of the 40 and 45 wt% samples are approximately 27%. However, the results obtained from the calculation are not very reproducible, probably because of a contribution to the isotropic peak from a disordered lamellar phase. The appearance of such a disordered phase contributes to the intensity of the isotropic peak and thus, the results. In addition, spectra for the 40 wt% sample at 27 °C before and after the heating cycle do not appear to be exactly the same. The spectrum is less well-defined after heating to 90 °C. However, the relative amounts of isotropic solution in both spectra are almost the same.

All the samples with concentrations above 50 wt% are L_α only over the whole temperature range until approximately 60 wt% surfactant, which can be seen by the two clearly resolved doublets (Figure 3.13d, e). Note that in Figure 3.13d the main peaks are broadened compared to the spectrum in Figure 3.13e, possibly due to the presence of small isotropic regions. These are too small to give a separate peak, but their water undergoes fast exchange with the neighboring lamellar phase, resulting

in a slightly reduced splitting in some parts of the sample. This appears to be a real effect rather than due to poor mixing. It suggests some "separation" of different compositions, not unexpected for such a poly-disperse surfactant. A consequence is that some of the $\Delta(^2H)$ values are slightly reduced (Figure 3.14).

A cubic phase (single peak) is observed for the 60 wt% sample at 90 °C, which is consistent with the phase diagram (Figure 3.11). On further increasing the surfactant concentration to 63 wt%, a single lamellar splitting is observed at 10 and 27 °C, but at 65 °C a minor second splitting besides the one obtained for the L_α phase is observed ($\Delta(^2H)$ = 164.38 Hz, Figure 3.13f). This is clear evidence for small amounts of a second phase (as discussed in the previous paragraph) and an example of a fairly rare behavior. It can be the appearance of an "intermediate" phase, which can appear at compositions around a bicontinuous cubic phase.[17] However, this subject is beyond these investigations and thus, will not be discussed any further. The L_α phase is followed by a bicontinuous cubic phase (V_2), which is then followed by a reverse hexagonal phase (H_2). Two well-resolved doublets arise, which are an indication for the H_2 phase (Figure 3.13g). For the 80 wt% surfactant solution, an alignment of the H_2 director along the NMR tube occurs, as indicated by the intense sharp outer lines in the spectra (Figure 3.13g). This alignment does not remain on cooling the sample to the L_α phase at 10 °C; however, the measurement is completely reproducible.

Finally, a second isotropic solution (Figure 3.13h) occurs (L_2) above 87 wt% of surfactant. Due to the isotropic structure of the bicontinuous cubic phase and the isotropic solutions, no quadrupole splittings are observed; only a single peak can be seen. All the results from the NMR measurements at higher surfactant concentrations are those expected from the phase diagram and in good agreement. All the observations are completely reproducible, as checked by repeat measurements of the same sample as well as measurements of different samples with the same composition.

Figure 3.14 illustrates the variation of the ^{2}H-NMR splitting, $\Delta(^2H)$, with various surfactant mole ratios at different temperatures (Figure 3.14a-e). $\Delta(^2H)$ increases sharply within the lamellar phase by increasing the concentration, but increases only
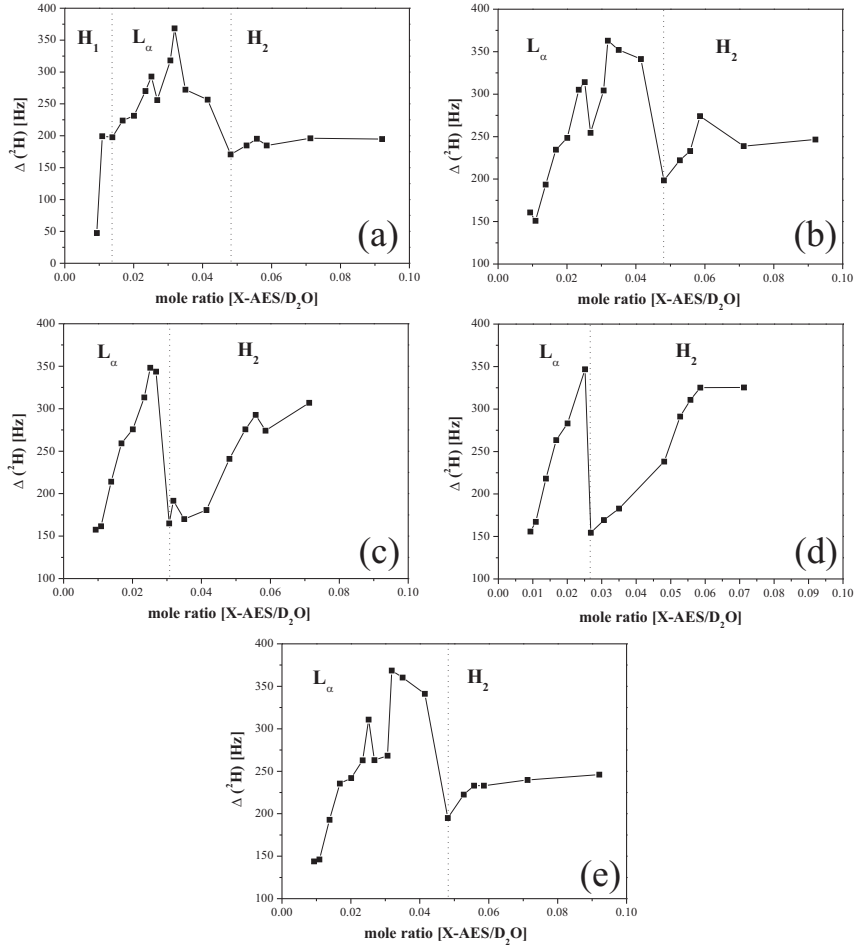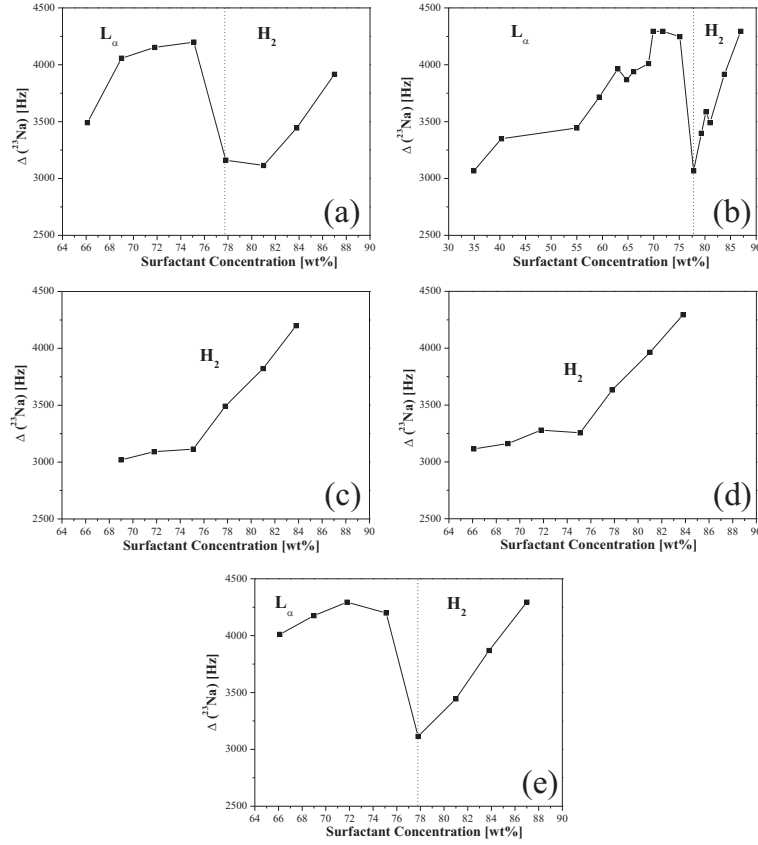
Figure 3.14: Deuterium NMR quadrupole splittings as a function of the surfactant/water mole ratio for the different mesophases of the extended surfactant X-AES: (a) $\theta = 10\ °C$; (b) $\theta = 27\ °C$; (c) $\theta = 65\ °C$; (d) $\theta = 90\ °C$; (e) $\theta = 27\ °C$ (after).

slightly with temperature. At a certain concentration, the $\Delta(^2H)$ values show some scatter (ca. ± 60 Hz). This occurs in the region discussed above where broad lines were observed, as seen in Figure 3.13d. The increase in $\Delta(^2H)$ of the L_α phase is followed by a sharp decrease, which is explained by the formation of the reversed hexagonal phase. The values are smaller than for the L_α phase, but not by the expected factor of two at lower temperatures (Figure 3.14a, b, e). Smaller than expected $\Delta(^2H)$ values for the L_α phase because of the presence of minor amounts of a second phase with small $\Delta(^2H)$ values could be responsible for this, as discussed above. Furthermore, it could be shown that the $\Delta(^2H)$ values observed from the

measurements at 27 °C after the heating cycle are close to the results at 27 °C be-
fore heating. This effect shows that no long-lived changes appear due to the heating
procedure.

The $\Delta(^2H)$ values in Figure 3.14 can be compared with those of sodium dodecyl
sulfate (SDS).[154] The values for SDS are larger by about a factor of 5-10. This
probably arises from the lower values of S_b^w for X-AES due to the larger range of
conformations for the -$(EO)_2SO_4$ head-group compared to the SO_4 head-group, as
indicated by the larger area per molecule (see X-ray data below).

The concentration dependence of the $\Delta(^2H)$ values in Figure 3.14 shows a sharp
increase with X-AES concentration followed by a leveling-off at the highest concen-
trations and low temperatures. This trend is continuous across both the L_α and
H_2 phases, provided that account is taken of the x2 factor difference due to the
difference in phase symmetries noted above. A simple model for an equilibrium
between "bound" and free water has been used previously to rationalize these data
as explained above. This has been developed further to allow an estimation of the
numbers of bound waters per surfactant.[158] Remarkably, the theory predicts that
a maximum in $\Delta(^2H)$ values will occur at a surfactant/water mole ratio of *1/(n-1)*,
where n is the number of bound waters per surfactant. The model assumes that all
bound waters are identical, which is clearly not valid here. The curves in Figure 3.14
do level-off at high concentrations, with this occurring at higher mole ratios at higher
temperatures. That there is no abrupt change (except for the factor of 2) at the
L_α/H_2 boundary shows that there is no change in water binding between the two
phases. The value of the mole ratios at the point where the $\Delta(^2H)$ values level-off
was taken to estimate the maximum possible number of bound water molecules.
This occurs at mole ratios of ca. 0.05 at 10 °C, rising to ca. 0.06 at 90 °C. The
values of n estimated from this are $n \approx 21$ (10 °C) and $n \approx 18$ (90 °C). However, at
low temperatures it is suspected that the $\Delta(^2H)$ values could be influenced by the
presence of a second phase; thus, the second estimate was taken as the more valid.
Since two EO groups might be expected to bind ca. 5 molecules of water, while
the $NaSO_4^-$ head-group will bind ca. 10 molecules, a total of ca. 18 bound water
molecules appear to be reasonable.[173] EO groups usually have a reduced solubility

in water at high temperatures because of the dehydration at higher temperatures. However, this is not the case for this anionic surfactant; the negative charge of the sulfate head-group dominates preventing the reduced solubility. There is no evidence of any drastic reduction in the amount of bound water with increasing temperature. No change larger than the uncertainties associated with the estimation of bound water was observed.
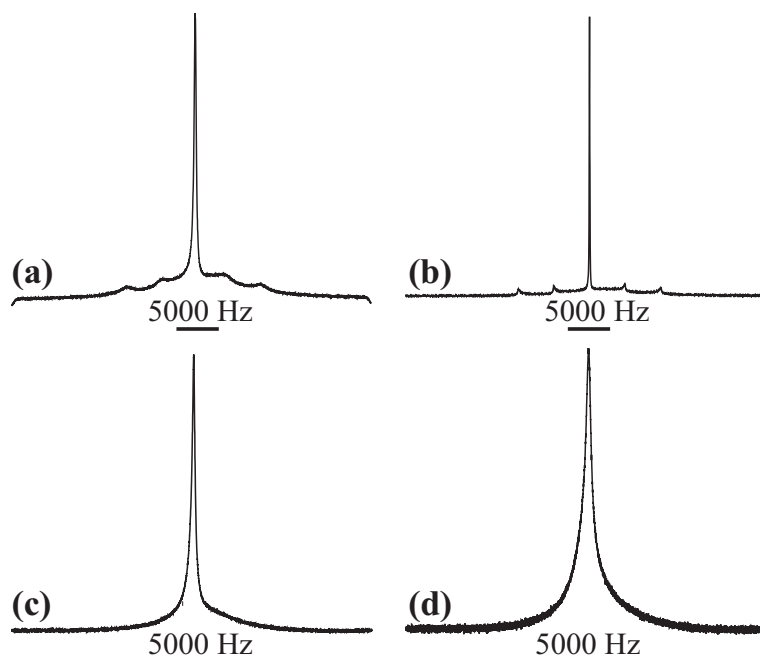
Figure 3.15: Typical ^{23}Na-NMR spectra of an X-AES solution at different concentrations and temperatures: (a) 84 wt% (H$_2$), 10 °C; (b) 84 wt% (H$_2$), 65 °C; (c) 90 wt% (L$_2$), 27 °C, (d) 95 wt% (L$_2$), 27 °C.

Typical ^{23}Na-NMR spectra are given in Figure 3.15. In the ^{23}Na spectra it is difficult to detect small quantities of the isotropic phases (L$_1$, V$_2$, and L$_2$) because of the central peak, which is always present.[151, 154, 155] The results obtained from the sodium NMR measurements are in good agreement with the deuterium NMR measurements. The ^{23}Na splittings ($\Delta(^{23}$Na$)$) against the surfactant concentration at different temperatures are shown in Figure 3.16. The $\Delta(^{23}$Na$)$ values are much more constant with increasing concentration and temperature than the $\Delta(^2$H$)$ values. As with the deuterium data, the actual splittings are much smaller in comparison to SDS ($\Delta(^{23}$Na$)$ = ca. 9 ± 1 kHz for the H$_1$ phase, and ca. 20-35 kHz for

the L_α phase; there is no H_2 phase).[156] This clearly results from the more disordered nature of the head-group region for X-AES compared to SDS because of the extra configurational freedom allowed by the EO groups. The quadrupole splittings increase somewhat within the lamellar phase with increasing surfactant concentration, as for the L_α phase of SDS. Moreover, the $\Delta(^{23}Na)$ decreases at the L_α to H_2 transition, but by less than a factor of two followed by an increase within the H_2 phase. These changes are consistent with an increase in Δ_b^{Na} due to an increase in S_b^{Na} which, in turn, is caused by a reduction in the surface area per molecule as the X-AES concentration is increased. No large change in the counter-ion binding within the mesophases is suggested, for example at the L_α/H_2 transition.

For the 66 wt% sample at 90 °C and the 69 wt% at 65 °C, a quadrupole splitting is observed, indicating the appearance of a reverse hexagonal phase at these concentrations and temperatures, contrary to the phase diagram in Figure 3.11. However, as already mentioned before, a two phase region appears especially at the phase boundaries (e.g. $V_2 + H_2$). Due to the isotropic structure of the cubic phase, it is difficult to detect it using ^{23}Na-NMR measurements because of the intense central peak, but two phases ($V_2 + H_2$) are observed with ^2H-NMR at these temperatures and concentrations. The obtained quadrupole splittings of the two phase region from the ^2H- and ^{23}Na-NMR are shown in Figure 3.14c, d and 3.16c, d, respectively.

Above 81 wt% X-AES, the ^{23}Na lines in the spectra are broadened at 10 °C (for example Figure 3.15a). This broadening is attributed to a reduction in the molecular motion of the ^{23}Na ions due to the decreased water content. In addition, ^{23}Na-NMR spectra of the reverse isotropic solution (L_2) also show a broadening of the isotropic single peak (Figure 3.15c, d). The linewidth increases from 414 Hz (87 wt% X-AES) to 1058 Hz (95 wt% X-AES). Sharp resonances are usually observed for fast molecular motion of the sodium ions around the surfactant head-group, while broad peaks are observed for slow molecular motion of the sodium ions. The size of the reversed micelles is increasing strongly from 87 wt% to 95 wt% X-AES. Hence, the linewidth is increasing due to the slow motion of the sodium ions around the head-groups.

Figure 3.16: Sodium NMR quadrupole splittings as a function of the surfactant concentration for the different mesophases of the extended surfactant X-AES: (a) $\theta = 10$ °C; (b) $\theta = 27$ °C; (c) $\theta = 65$ °C; (d) $\theta = 90$ °C; (e) $\theta = 27$ °C (after).

c) X-ray Scattering

X-ray data were performed for a concentration range between 30 and 95 wt% of surfactant in H_2O to supplement the results from NMR measurements and to obtain the dimensions of the aggregates. Figure 3.17 shows typical SAXS patterns for the L_α, V_2, H_2, and L_2 phases at 25 °C. The L_α phase is clearly identified since the positions of the first and second Bragg peaks are in a ratio of 1:2. Increasing the surfactant concentration, the first- and second-ordered peak positions can be found to be $1:\sqrt{3}$, which is consistent with a V_2 as well as an H_2 phase. However, optical microscopy helped to distinguish between the bicontinuous cubic and the reverse hexagonal phase. Increasing the concentrations of the surfactant further, no second-ordered peak can be found, only a single peak appears. This isotropic phase
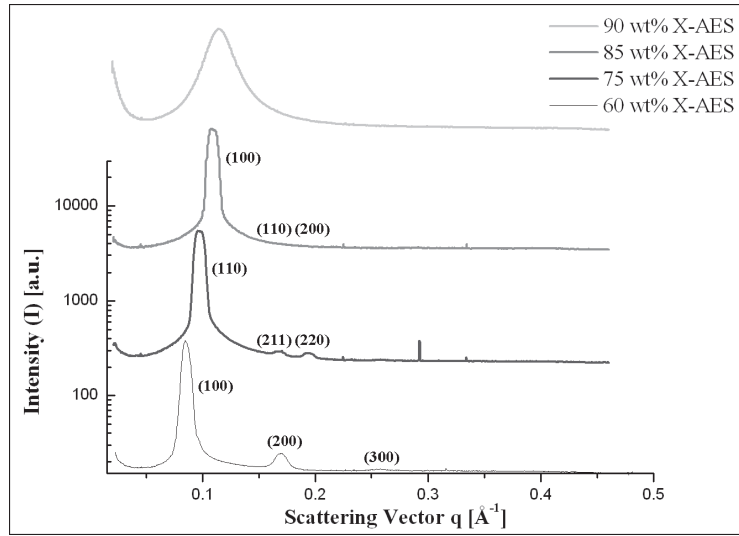
Figure 3.17: Small-angle X-ray scattering for three different mesophases and the L_2 phase at 25 °C; 60 wt% X-AES: lamellar phase L_α , 75 wt% X-AES: bicontinuous cubic V_2, 85 wt% X-AES: reverse hexagonal H_2 and 90 wt% X-AES: inverse micellar phase L_2. The numbers give the reflection indices.

showed a broad peak with an aggregate diameter of $d_{max} = 5.49$ nm. The following was already mentioned in section 1.6. However, because of its main importance for the analysis of the SAXS results some of the calculations are repeated in this section. The alkyl chain volume fractions, which are necessary for further calculations, can be obtained by using the expression by Luzzati as follows:[41]

$$\phi_a = \frac{M_a}{M\left(1 + \frac{\varphi_a(1-c)}{\varphi_w c}\right)}. \tag{3.5}$$

An approximation was done by considering that the polar head-group including the two oxyethylene groups to be in the aqueous region of the phases. M is the molecular weight of the surfactant and M_a is the molecular weight of the hydrophobic tail, including the oxypropylene groups. c is the weight fraction of X-AES, φ_a and φ_w are the densities of the hydrophilic and hydrophobic part, respectively. The density of the polar head-group was assumed to be 1.0 g cm^{-1} and 0.85 g cm^{-1} for the hydrophobic tail. The volume fractions of all concentrations are shown in Table 3.2. For the lamellar phase, the thickness of the uniform hydrophobic layer d_{hc}, containing all the hydrophobic tails of one layer can be calculated after Luzzati,[41] using the

separation of the bilayers d_0, and the volume fraction ϕ_a:

$$d_{hc} = \phi_a d_0 \tag{3.6}$$

assuming that the bilayers of the lamellar phase are infinite, continuous, and without breaks. Thus, the area per molecule S_a can be calculated as follows:

$$S_a = \frac{2V_a}{d_{hc}} = \frac{2V_a}{\phi_a d_0} \tag{3.7}$$

where V_a is the volume of the hydrophobic tail, which was calculated to be 1.877 nm³. For the reverse hexagonal phase, the diameter of the water cylinders d_{cw} is calculated from:

$$d_{cw} = 2d_0 \left[\frac{2\phi_w}{\pi\sqrt{3}} \right] \tag{3.8}$$

and the surface area per molecule S_a at the interface is given as:[45]

$$S_a = \frac{\left[a\phi_w V_a \right] \times 10^{24}}{\left[d_{cw} N_A n_a \right]} \tag{3.9}$$

where ϕ_w is the volume fraction of the water, N_A is the Avogadro number and n_a is the number of moles of amphiphile per gram of mesophase. The results for each sample of the lamellar and the reverse hexagonal phase were calculated and are also shown in Table 3.2. No calculations were made for two-phase samples, e.g. for the 30-45 wt% samples because of the presence of the L_1 phase within the L_α phase. Further discussion of the X-ray data is given below.

	wt% X-AES	T [°C]	ϕ_a	d_0 [nm]	d_{hc} [nm]	S_a [nm^2]
	30.0	25.0	0.29	9.04		
		65.0	0.29	10.39		
		90.0	0.29	10.08		
	35.2	25.0	0.33	9.67		
		65.0	0.33	10.63		
		90.0	0.33	10.92		
Lamellar	39.4	25.0	0.37	9.68		
Phase		65.0	0.37	10.86		
(L$_\alpha$)		90.0	0.37	11.09		
	45.1	25.0	0.42	10.08		
		65.0	0.42	10.48		
		90.0	0.42	10.68		
	50.1	25.0	0.46	9.10	4.21	0.89
		65.0	0.46	9.31	4.31	0.87
		90.0	0.46	9.61	4.45	0.84
	54.9	25.0	0.50	8.49	4.27	0.88
		65.0	0.50	8.83	4.45	0.84
	59.7	25.0	0.54	7.67	4.17	0.90
		65.0	0.54	7.92	4.30	0.87
		90.0	0.54	8.17	4.44	0.85

	wt% X-AES	T [°C]	ϕ_a [nm]	Unit Cell [nm]	Space Group
Bicontinuous	69.7	25.0	0.62	9.13	I4$_1$32
Cubic Phase		65.0	0.62	9.64	I4$_1$32
(V$_2$)	75.1	25.0	0.67	9.20	I4$_1$32

	wt% X-AES	T [°C]	ϕ_a	ϕ_w	d_0 [nm]	d_{cw} [nm]	S_a [nm^2]
Reverse							
Hexagonal	75.1	65.0	0.67	0.33	6.45	1.58	0.49
Phase		95.0	0.67	0.33	7.22	1.77	0.44
(H$_2$)	84.3	25.0	0.74	0.26	5.78	1.11	0.55

Table 3.2: Parameters obtained for the lamellar phase L$_\alpha$, the reverse hexagonal phase H$_2$, and the bicontinuous cubic phase V$_2$ of the extended surfactant X-AES at different temperatures, showing the weight fraction wt%, the temperature T, the volume fraction of the alkyl chain ϕ_a, the volume fraction of water ϕ_w, the interplanar distance d_0, the thickness of the alkyl layer d_{hc}, the diameter of the water cylinders d_{cw}, the surface area per molecule S_a, the unit cell, and the space group of the bicontinuous cubic phase.

Discussion

a) The Hexagonal Phase

The hexagonal Phase (H_1) was determined by optical microscopy (Figure 3.12a) and ^{2}H-NMR measurements. The H_1 phase is only stable for small temperature and concentration ranges. It emerges from rod-like micelles at 35 wt% surfactant and 0 °C. At this concentration the lyotropic liquid crystal remains stable until 20 °C and then turns into a L_α phase. In addition, it is important to mention that the NMR spectra of the H_1 phase were never observed without the appearance of an isotropic solution (L_1). Optical microscopy images of the 35 wt% sample below 5 °C confirm this result. The ^{2}H-NMR splitting of this phase at low temperatures is rather difficult to measure because the splittings are poorly resolved.

However, a quadrupole splitting was observed (Figure 3.13a) with a value of about 50 Hz for a 40 wt% surfactant solution at 10 °C. At the H_1/L_α boundary, Δ should change by a factor of two. Comparing the splittings of the H_1 and L_α phase from the NMR data (see Figure 3.13a), $\Delta(^2$H$)$ changes by a factor of approximately four from 50 Hz to 200 Hz. This effect appears because the rod-like micelles in the hexagonal phase are more disordered than usual due to being close to their melting point. Due to the small temperature and concentration range, and also possibly because of the disorder, it was not possible to obtain a well defined spectrum with higher order reflections from the SAXS measurements.

b) The Lamellar Phase

The lamellar phase was clearly identified by its optical texture (Figure 3.12b), NMR measurements, and from the ratio of the first- and second-ordered Bragg peaks using SAXS. The calculated parameters from the SAXS measurements for the lamellar phase are shown in Table 3.2. The all-trans length of the tail can be calculated to be 7.87 nm. It shows that the alkyl chain in the lamellar phase is shortened between 73% (for 60 wt% X-AES) and 84% (for 30 wt% X-AES). This indicates a very disordered state and suggests that the hydrophobic tails on opposing layers are mixed together. The shortening of the alkyl chain of an extended surfactant is more pronounced than for conventional surfactants.[174] Alternatively, the chains

are highly folded. The alkyl layer thickness and the area per molecule for low surfactant concentrations (30-45 wt%) were not calculated due to the presence of an isotropic solution (L_1). Increasing the concentration, d_{hc} and S_a are constant from 50 to 60 wt%.

The area per molecule is relatively high compared to conventional surfactants. Moreover, the calculated sphere to rod ($S_a < 72$ Å^2) and rod to disc ($S_a < 48$ Å^2) transitions for this surfactant are much smaller than the obtained area per molecule (S_a) for the lamellar phase of X-AES (Table 3.2). Therefore, spherical rather than disc-like micelles should occur. Hence, there must be a strong influence of the alkyl chains in providing a contribution to the negative curvature of the micelle surface. This is likely to be an entropic effect of the chain conformation preventing the all-trans form from occurring in quantities required to stabilize spherical micelles. Furthermore, S_a decreases slightly with increasing temperature. This result is in good agreement with the NMR data. The quadrupole splittings of both ^{23}Na- and ^{2}H-NMR, for the L_α phase are increasing with increasing surfactant concentration. The quadrupole splittings change with the fraction of bound water and its order parameter. If the area per molecule decreases (which is the case for this surfactant by increasing the concentration), the order parameter of bound water is expected to increase. Note that the thickness of the aqueous layer is always larger than the fully extended length of two head-groups (ca. 2.7 nm).

c) The Bicontinuous Cubic Phase

The bicontinuous cubic phase was investigated by optical microscopy, SAXS (Figure 3.17), and ^{23}Na- and ^{2}H-NMR. Due to the isotropic structure, the cubic phase did not show birefringence under the optical microscope and only a black ring was observed in the penetration scan (Figure 3.1). Furthermore, a single peak is observed from ^{23}Na- and ^{2}H-NMR. The experimentally observed spectrum and the spacings from SAXS measurements are given in Figure 3.17 and Table 3.2, respectively.

The analysis of the SAXS spectra of the bicontinuous cubic phase was affiliated with difficulties. Only three peaks are observed, which could be mistaken for the

reverse hexagonal phase (H_2). Additional optical microscopy clearly identified the cubic phase samples (70 wt% at 25 and 65 °C, 75 wt% at 25 °C) from the SAXS measurements and could eliminate any ambiguity. Within these samples, the first and second-ordered peak positions can be found to $1:\sqrt{3}$, where only the space group $I4_132$ (No 214) can be fitted to the three reflections (110), (211), and (220). The $I4_132$ space group is a body-centered cubic phase with a 4-fold screw axis in [100] direction, a 2-fold rotation axis in [111], and a 2-fold rotation axis in [110] direction.[175] Furthermore, it is a sub-group of the more common bicontinuous cubic space group $Ia3d$, which is formed by a translational transition. The $I4_132$ space group is rarely known for conventional surfactants and often observed for (triblock) copolymers or lipid systems.[46, 176, 177] The choice of the common $Ia3d$ space group can be excluded in this case because of the number of absence peaks in the spectrum ((211), (321), (400), etc.). In addition, the second-ordered peak position cannot be fitted to any reflection of the $Ia3d$ space group. Furthermore, due to the fact that reflections followed after the first-ordered Bragg peak can be too weak or overlapped, also $Im3m$ (absence of reflection (211)) and $Pn3m$ (reflections (111) and (200) absent) could be possible space groups. Therefore, more measurements are necessary to prove the presence of the $I4_132$ space group; however, this investigation is not of main interest for this thesis.

The observed results for the unit cell are approx. 9.2 nm at 25 °C and are increasing to 9.6 nm at 65 °C (Table 3.2). These results are much lower compared to SDS (11.7 nm), but in the range of the values obtained for anionic surfactants (usually between 7 and 12 nm).[17, 173] Compared to non-ionic surfactants, the values of the unit cell of the extended surfactant are higher than, for example, the size of a similar unit cell ($Im3m$) of $C_{12}EO_{12}$ at 50.2 wt% of surfactant in water with 7.4 nm.[47] In summary, the unit cell of the extended surfactant is in the same range as of common actives. This result is surprising because X-AES is much bigger than the mentioned surfactants. Hence, X-AES must have a geometry by a factor of about five shorter in comparison to the all-trans length, similar to the reduced length within the L_α phase.

d) The Reverse Hexagonal Phase

The SAXS pattern of this phase (Figure 3.17) is characteristic for an H_2 phase as is the optical texture (Figure 3.12c). Again, the first- and second-ordered peak positions can be found to be $1 : \sqrt{3}$. The results for all the samples were calculated and are shown in Table 3.2. The area per molecule is significantly smaller than for the lamellar phase. In addition, it is decreasing with temperature and appears to increase at the highest concentration, although, more data are required to confirm this. This result leads to the inference that the polar head-group is stretched. However, the value of d_{cw} is again much shorter than the full extension of two head-groups. Thus, the ether-sulfate groups still have some conformational disorder despite the relatively small area per molecule compared to the lamellar phase. Furthermore, due to the small amount of water molecules at higher surfactant concentrations,the EO groups may not be as much hydrated as in the lamellar phase.

e) The Reverse Isotropic Solution and Solid Particles
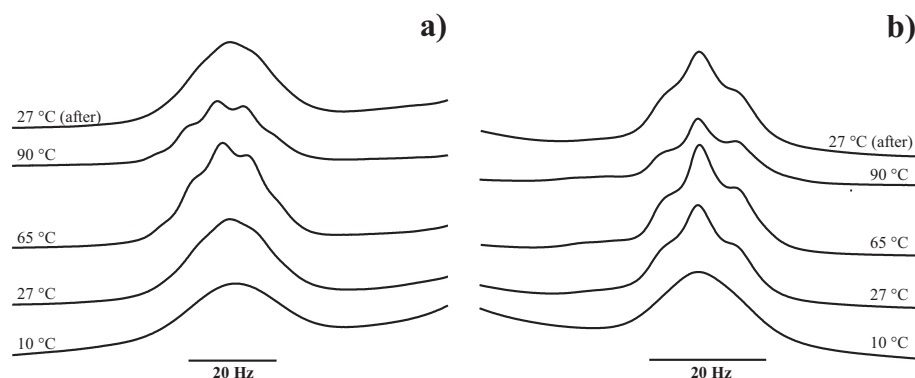
Figure 3.18: Sequence of ^{1}H-NMR spectra of a 95 wt% surfactant solution at different temperatures. (a) terminal CH_3 group; (b) β-CH_2 of the alkyl chain.

The reverse micellar solution (L_2) was also determined by optical microscopy (Figure 3.12d), NMR, and SAXS measurements. Using optical microscopy, an isotropic phase was observed containing solid particles. In addition, a broad single peak could be seen from the SAXS measurements, which is typical for an isotropic

solution. These results were supported by a single peak obtained from ^{2}H-NMR measurements, which is also specific for an isotropic solution.

^{1}H high resolution NMR measurements were performed to determine the size of the reverse micelles in the L_2 phase. As already described in the previous section, sharp resonances are observed for small micelles, while broad peaks occur for bigger micelles. Proton NMR spectra were recorded for solutions in D_2O over the concentration range 80-95 wt% and the temperature range 10-90 °C. The remaining peak assignment was carried out using readily available standard chemical shift data.[162] To illustrate the changes in linewidths, the terminal methyl peak (appears as a triplet due to scalar J coupling from the adjacent CH_2 group, Figure 3.18a) and the β-CH_2 group (is a quintet due to scalar J coupling from the two adjacent CH_2 groups, Figure 3.18b) were chosen, which are well separated from the other resonances.

The increase in linewidth arises from incompletely averaged ^{1}H-^{1}H dipole-dipole coupling and thus, the size of the micelles can be estimated. Calculations were performed using the approach of Staples *et al.*[163] and were already described in the last section. For the reverse micellar solution, the order parameter S was assumed to be the same as for normal micelles; hence, 0.01 for the terminal CH_3 group and 0.05 for the β-CH_2.[164, 166] Using the calculations made by Staples *et al.*, the rotation relaxation time τ_c^s can be calculated. Furthermore, with the help of the Stokes-Einstein equation (Equation 3.3), the radii of the reverse micelles at different temperatures and concentrations can be estimated.[163, 167] However, given the very approximate estimates of the order parameters, these values must be considered with caution. In addition, the viscosity of the continuous phase in the reverse system is necessary to obtain correct sizes of the reverse micelles. Therefore, viscosity measurements were performed to obtain the viscosity values of the samples at the same temperatures as used for NMR-measurements (see Table 2.1).
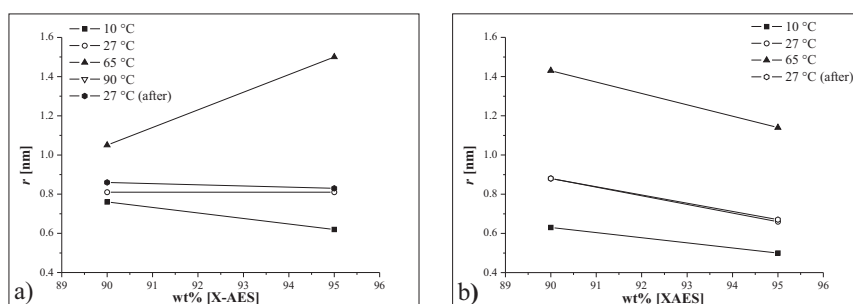
Figure 3.19: Calculated radius from the linewidth against the surfactant concentration at different temperatures: a) terminal CH_3; b) β-CH_2.

The calculated values for the radius from the terminal CH_3 group and the β-CH_2 group are given in Figure 3.19a, b. Starting with the 90 wt% terminal CH_3 group, a radius can be calculated (0.75-1.05 nm), which increases with increasing temperature. On increasing the concentration (95 wt%) and the temperature, a small change in micelle size occurs (0.6-1.5 nm). Looking at the sizes calculated from the linewidth of the β-CH_2 group, the sizes decreases insignificantly with increasing concentration and increases with increasing temperature (0.6-1.45 nm). After a heating cycle (cooling to 10 °C, heating to 90 °C, and again cooling to 27 °C, ca. 4 h), the size of a micelle at 27 °C is the same as before. The obtained sizes of the reverse micelles are, as expected smaller than for the normal micelles (0.6-1.5 nm) due to the smaller head-group in comparison to the hydrophobic tail. The obtained radius reflects the size of the hydrophilic micelle core, containing the EO groups, the sulfate head-group, and the water. The sizes estimated from the NMR measurements are not so different from the X-ray scattering peak observed for the L_2 phase (aggregate diameter ca. 5.5 nm). Thus, the measurements do confirm the presence of reversed micelles. The radius of the extended surfactant is smaller in comparison to conventional surfactants.[178, 179]

The solid particles were analyzed by optical microscopy, IR-spectroscopy, elementary analysis, and energy-dispersive X-ray spectroscopy (EDX). Optical microscopy could show that the solid particles remain unchanged until at least 150 °C leading to the assumption that these particles are mainly inorganic. This fact was proved by elementary analysis, which showed that 20% of the solid particles are organic

and 80% inorganic. The presence of NaCl and Na_2SO_4 could already be proved by ion chromatography. IR-spectroscopy showed bands typical for sulfate (inorganic, 1130-1080 cm^{-1}) and for carbonate (1450-1410 cm^{-1}). Additionally, EDX confirmed the presence of the elements C, H, O, S, Cl, and Na. No other elements were detected with EDX. Furthermore, it is known that double fatty acids are produced through side reactions during the synthesis of the surfactant. Hence, other substances than the ones already mentioned can be excluded. In summary, the solid particles consist of organic compounds (e.g. double fatty acids) and inorganic substances, like salts (e.g. NaCl, Na_2SO_4, etc). All these compounds are impurities due to the synthesis of the surfactant. It is also worth to mention that the solid particles can be removed from the surfactant by washing X-AES with acetone, separating the two phases and drying the particles and the surfactant. The separation process has no influence (besides the absence of the solid particles) on the phase behavior of X-AES, which could be shown by a penetration scan of the cleaned surfactant.

f) Comparison to Common Surfactants without Linker Groups - Sodium Dodecyl Sulfate (SDS), Sodium Dodecyl-di-Oxyethylene Sulfate (SLES), and Sodium Linear Alkylbenzene Sulfonate (LAS).

The behavior of the X-AES/water mixtures is very unusual in that both normal (water-continuous) and reversed (alkyl chain-continuous) phases are present. This is the first report of a surfactant that forms both H_1 and H_2 phases without the addition of a third component (e.g. a co-surfactant). It demonstrates the wide range of structures that can be formed by extended surfactants as a result of their very flexible molecular structure.

By comparing the extended surfactant X-AES with sodium dodecyl sulfate (SDS), sodium dodecyl-di-oxyethylene sulfate (SLES) and commercial sodium linear-alkylbenzene sulphonate (LAS), the influence of the hydrophilic (EO-group)/lipophilic linker (PO-group) on the phase behavior can be quantified.[17, 156, 180–183] Starting with the low concentration area of the phase diagram, a Krafft temperature is observed for SDS, but not for X-AES, SLES or LAS. The Krafft temperature depends on the hydrophilic head-group and even more on the

hydrophobic alkyl chain. The longer the alkyl chain, the higher the Krafft temperature. However, crystallization can be hindered if the alkyl chain contains methyl or other alkyl group branches, which prevent a regular packing into the crystalline phase (as with LAS, A-OT or PO surfactants). For PO surfactants, the polydispersity of the PO moiety will also help to prevent crystallization because only molecules with the same number of PO groups will crystallize together. Other contributions come from the polarity of the head-group (which increases the solubility) and the structural polydispersity of the head-group (which prevents crystallization because different homologues crystallize separately, as with SLES). The latter clearly makes a contribution for X-AES because SLES has a Krafft temperature below 0 °C. However, the main contribution for X-AES arises from the presence of the PO groups. On increasing the surfactant concentration, liquid crystalline phases appear for all the surfactants. However, for SDS a certain solubility temperature is necessary to form liquid crystals due to the Krafft boundary. By contrast, X-AES and the other two surfactants are soluble over the whole concentration and temperature range. The first liquid crystal phase for X-AES over most of the temperature range is the L_α phase and a transition from L_1 to L_α is observed by increasing the temperature. SLES and SDS give an H_1 phase, so the difference in behavior is due to the compressed chain configurations of the long linker moieties as was already described before. This is a very significant effect - a large amount of chain branching is required to remove the H_1 phase for conventional surfactants, for example with LAS. For SDS and SLES on increasing the surfactant concentration, a cubic phase (V_1) appears before the lamellar phase, while for the extended surfactant the cubic phase (V_2) arises after the lamellar phase. With X-AES the limited range of the H_1 phase is the cause of the non-appearance of a V_1 phase. Again, this is a consequence of the compressed chain configurations of the long linker moieties.

The phases that occur at concentrations above the lamellar phase are not seen with conventional single chain ionic surfactants. Again, this is attributed to the greater solubility of X-AES in water and to the long PO linker. Remarkably, the neat surfactant forms a liquid rather than a liquid crystal or solid. Most ionic surfactants require temperatures well above 100 °C for this to occur, where decomposition is

also commonplace. This must be because the volume fraction of polar groups is too small to form an ordered phase (as forms with neat A-OT). The reversed micelles formed by X-AES must also be fairly small and globular in shape. Further measurements are required to elucidate their structures in greater detail.

Concluding Remarks

In this work, the different mesophases observed for a chosen alkyl polypropylene oxide ether sulfate surfactant (extended surfactant, X-AES) and an isotropic liquid phase (reversed micellar) were determined and analyzed. Four liquid crystal phases are formed in the X-AES-water system; a hexagonal (H_1), a lamellar (L_α), a bicontinuous cubic (V_2), and reverse hexagonal (H_2) phase. It was shown that the hexagonal phase, appearing at low concentrations and temperatures, consists of rod-like micelles, which are more disordered than in conventional surfactants. In addition, a L_1 phase is always present within the H_1 phase. This effect is also found within the L_α phase at lower surfactant concentrations. The L_α phase appears over a large concentration and temperature range. Again, a disordered state can be found for the L_α phase proving that the hydrophobic tails are linked into each other and highly folded. The relatively high area per molecule leads to the inference that there must be a strong influence of the alkyl chains on the negative curvature of the micelles. The bicontinuous cubic phase and its cell parameters were identified. The unusual space group $I4_132$ was found to be the most likely symmetry of the bicontinuous cubic phase. However, the $Im3m$ and $Pn3m$ space groups could not be excluded and hence, more detailed measurements are necessary. The reverse hexagonal phase and its aggregate parameters were also determined. Furthermore, the isotropic solution at highest surfactant concentrations was analyzed and it was possible to obtain a radius for the reverse micelles, which is between 0.6 and 1.5 nm and thus, much smaller than the size of the normal micelles (see Section 3.1.1). In addition, the structure and origin of the solid particles was identified. A comparison between the extended surfactant and common anionic surfactants SDS, LAS, and SLES was made, concluding that the hydrophilic/lipophilic linkers have a strong influence on the phase behavior of the extended surfactant.

3.2 Hydrotrope Induced Inversion of Salt Effects on the Cloud Point of an Extended Surfactant

3.2.1 Introduction

Specific ion effects are particularly pronounced at the interfaces of different phases. A first series of salts was established more than a century ago by Franz Hofmeister, a pharmacologist, on protein solutions.[114, 115] A detailed explanation of the Hofmeister series is already given in section 1.5. As previously mentioned, certain anions can be classified as "salting-in" (chaotropes, weakly hydrated, strongly polarizable) or "salting-out" (kosmotropes, strongly hydrated, weakly polarizable), according to their ability to increase or decrease the solubility of proteins in water. The Hofmeister series for anions roughly is ("salting-out") $SO_4^{2-} > HPO_4^{2-} > CH_3COO^-$ $> F^- > OH^- > Cl^- > Br^- > NO_3^- > I^- > ClO_4^- > SCN^-$ ("salting-in"; the positions of the NO_3^- and Br^- ions are often switched in the lyotropic series).[113–117] In this series, the most "salting-out" ions are on the total left side and the most "salting-in" ions on the total right side. The borderline is often drawn at the chloride ion, which has nearly no influence on protein solubility. Each salt is therefore expected to either adsorb at the interface between the micelles and the water ("salting-in") or to remain strongly hydrated in the bulk ("salting-out").[106, 113]

Furthermore, extensive studies have shown that the counterion has a strong influence on the thermodynamics and aggregation properties of surfactants.[113, 117, 118] The differences in the cation effects appear less significant than those seen with the anions. A general explanation is that kosmotropes have a high charge density and a tightly bound hydration shell and hence, they tend to be excluded from the surface. On the other hand, chaotropes have a low charge density and a less tightly bound hydration shell which leads to a higher association with non-polar surfaces or with "soft" head-groups.[115, 119] In this part of the work, the effect of different anions and cations on the solubility of the extended surfactant, X-AES (C_{12-14}-$(PO)_{16}$-$(EO)_2$-SO_4Na, Figure 2.1) was examined and the "pseudo"-binary phase diagrams were observed. Furthermore, the influence of sodium xylene sulfonate (SXS), a

well-known hydrotrope, on the cloud temperature of X-AES was determined. In a final step, a solution containing a mixture of X-AES and SXS (mole ratio R(X-AES/SXS) = 0.5) in water was prepared and the influence of added electrolytes on the solubility of the X-AES/SXS mixture was studied. Again, "pseudo"-binary phase diagrams of the X-AES/hydrotrope solution with different concentrations of anions and cations were recorded. In addition, the surfactant/water/salt and the surfactant/hydrotrope/water/salt mixtures were analyzed using optical microscopy, NMR measurements, and freeze-etch transmission electron microscopy (FE-TEM). The mechanism of the different phase transitions will be discussed in detail.

3.2.2   Results

The extended surfactant X-AES in water alone has a cloud temperature, which decreases with increasing concentration. By increasing the temperature, a micellar L_1 to lamellar L_α phase transition is observed. The driving force for this transition is the growth of "potato-like" micelles into large bilayers. This transition obviously requires a reduction in aggregate curvature. The micelles grow because the hydrophobic tails of the extended surfactant get longer with increasing temperature (PO groups have a more extended conformation). This was already described in the last Section 3.1.

The influence of salts on the cloud temperature of the extended surfactant (X-AES) in water and a solution of the extended surfactant with a hydrotrope in water was examined using two different batch numbers of X-AES (batch No. 8625-2 and batch No. 8625-47). Thus, the cloud temperature of the 23 wt% X-AES stock solution can vary within 5 °C, depending on the used batch. Also, the cloud temperatures of the different salt solution prepared from the two batch numbers can vary within 5 °C. Nevertheless, besides the temperature shift no other effects on the phase behavior were observed. Especially, the "salting-in" and "salting-out" effects of the various salts were found to be the same.

Effect of Anions on the Cloud Point of X-AES

a) X-AES in Aqueous Electrolytes.
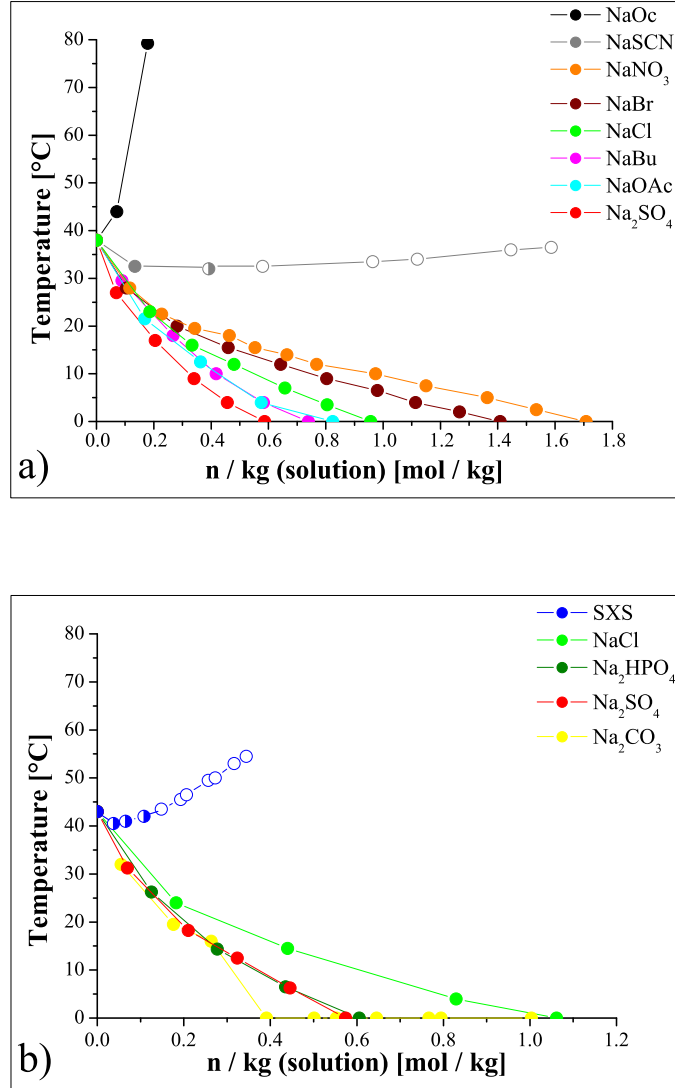
Figure 3.20: Influence of different anions on the phase behavior of the extended surfactant X-AES: (a) batch No. 8625-2; ● NaOc, [●, ◐, ○] NaSCN, ● $NaNO_3$, ● NaBr, ● NaCl, ● NaBu, ● NaOAc, ● Na_2SO_4; and (b) batch No. 8625-47: [●, ◐, ○] SXS, ● NaCl, ● Na_2HPO_4, ● Na_2SO_4, ● Na_2CO_3. Samples are clear below the curves and turbid above. The curves with the filled symbols show a $L_1 \rightarrow L_\alpha$ phase transition, while the curves with the empty symbols show a $L_1 \rightarrow L_1$'. For the half filled symbols a phase transition to both L_α and L_1' arises.

The effect of various anions on the clouding of a 23 wt% X-AES stock solution

(equivalent to 0.18 mol L^{-1}) was studied by varying the concentration of different sodium salts (NaOc, NaSCN, NaNO$_3$, NaBr, NaCl, NaBu, NaOAc, Na$_2$SO$_4$, SXS, Na$_2$HPO$_4$, and Na$_2$CO$_3$). The results of the "pseudo"-binary system (water/X-AES/anion) are shown in Figures 3.20a and b.

Depending on the salt, the cloud temperature can be either lower or higher than the cloud temperature of the 23 wt% X-AES solution. A decrease of the clouding with increasing salt concentration is observed, as expected for all "salting-out" anions (kosmotropes) and in this case for NaBu, NaOAc, Na$_2$SO$_4$, Na$_2$HPO$_4$, and Na$_2$CO$_3$. The curve for NaBu at low salt concentrations is slightly higher than the curve for NaOAc. NaBu has a small hydrophobic tail and adsorbs a bit more to the surfactant X-AES than NaOAc. Hence, it has a similar effect like NaOc. At higher salt concentrations, both curves are overlapping. In addition, NaNO$_3$, NaBr, and NaCl decrease the cloud temperature of the extended surfactant and are, in this case, considered to act more like a "salting-out" than a "salting-in" electrolyte.

On the other hand, for NaSCN the cloud temperature decreases for small amounts of salt and increases with higher concentrations, which is in agreement for a "salting-in" anion (chaotrope). The obtained results follow precisely the same behavior as expected from the Hofmeister series.[114, 115]

NaOc also increases the cloud temperature with increasing salt concentration. However, due to its structure, it is expected to behave more like a co-surfactant than a salt. It is well known that co-surfactants participate inside the micelles between the surfactant molecules. Thus, they can influence the curvature of the micelle and the internal energy. The short hydrophobic alkyl chain and the hydrophilic head-group enhance the interaction between the surfactant monolayers at the interface. Usually, low molecular weight alcohols or short chain amphiphiles are used as co-surfactants (Section 1.2).[184–186]

Optical microscopy was used to get detailed information about the phase transitions as well as on the clear and turbid regions. Images of the turbid regions (above the cloud temperature) are given in Figure 3.21. Depending on the salt, two different routes can be found. The first route is a transition from a clear solution (L$_1$) to a lamellar phase (L$_\alpha$, L$_1$ $\rightarrow$ L$_\alpha$ transition) and is observed for all
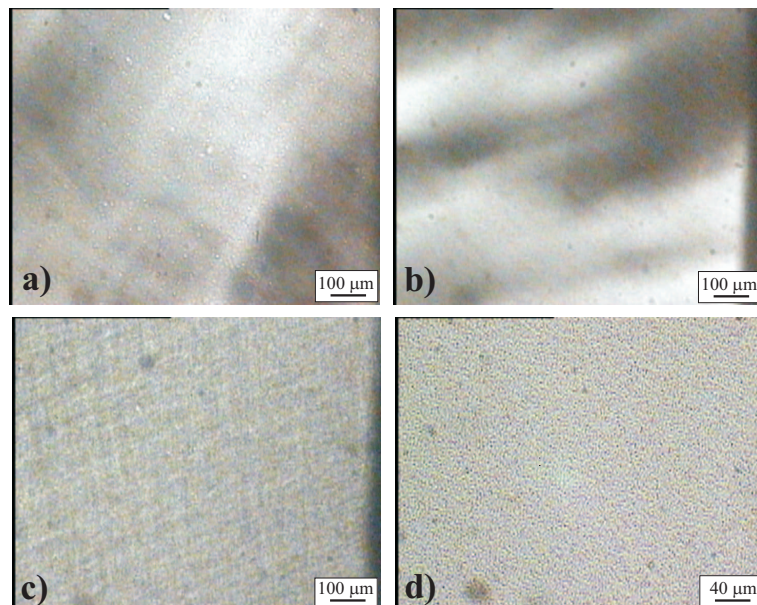
Figure 3.21: Optical microscopy images of a 23 wt% X-AES solution and different salts and of the two possible routes of phase transition using crossed polarisers. a) $L_1 \rightarrow L_\alpha$ phase transition of 0.4 mol/kg Na_2SO_4 at 35 °C ("salting-out", birefringent); b) $L_1 \rightarrow L_\alpha$ phase transition of 0.4 mol/kg NaCl at 30 °C ("salting out", birefringent); (c) $L_1 \rightarrow L_\alpha$ phase transition of 0.1 mol/kg NaOc at 60 °C (co-surfactant, "salting-in", birefringent); and (d) $L_1 \rightarrow L_1'$ phase transition of SXS 0.2 mol/kg at 45 °C (hydrotrope, "salting-in", droplets).

"salting-out" salts ($NaNO_3$, NaBr, NaCl, NaBu, NaOAc, Na_2SO_4, Na_2HPO_4, and Na_2CO_3) (Figure 3.21a and b). In this case, small droplets are obtained at temperatures around the cloud point. These droplets are too small to see the birefringence under the microscope. However, as described in section 3.1, they are expected to be a lamellar phase dispersion in water.

Increasing the temperature, a lamellar phase is observed (Figure 3.21a, b). Depending on the concentration of the salt, the birefringence of the lamellar phase can be weak (low salt concentration) or intense and well visible (higher salt concentration). In addition, increasing the temperature of the NaOc samples, a well defined lamellar phase is already observed at the cloud temperature ($L_1 \rightarrow L_\alpha$ transition, Figure 3.21c).

In contrast to the "salting-out" results, a second route can be found for all "salting-in" anions. When the cloud temperature decreases at low salt concentrations, a $L_1 \rightarrow L_\alpha$ phase transition appears. At the minimum of the curve, a lamellar phase

arises as well as larger droplets (Figure 3.20a [●, ◐, ○] NaSCN and Figure 3.20b [●, ◐, ○] SXS). Increasing the salt concentration more, the cloud temperature increases again without the appearance of a lamellar phase ($L_1 \rightarrow L_1'$). However, in this case well resolved droplets can be seen under the microscope. These droplets are very small around the cloud temperature and grow larger at higher temperatures, without any sign of birefringence.

Similar studies were performed by adding different concentrations of a hydrotrope (sodium xylene sulfonate, SXS, Figure 2.2) to the 23 wt% X-AES stock solution (equivalent to 0.18 mol L^{-1}). Hydrotropes are known to be weakly surface active and generally do not micellize. However, their presence enhances the solubility of a sparingly soluble material in water associated with a surfactant.[49, 51, 187] As seen in Figure 3.20b, the hydrotrope also decreases the cloud temperature at low salt concentrations and increases it at higher concentrations. Small droplets are seen around the clouding, growing larger at higher temperatures (Figure 3.21d). In this context, SXS is considered as a "salting-in" salt. Thus, it also shows a phase transition from $L_1 \rightarrow L_1'$. Similar studies were already performed by Bauduin *et al.*[187]

b) X-AES/SXS in Aqueous Electrolytes.

A stock solution containing a mole ratio of R(X-AES/SXS) = 0.5 was prepared to perform the same experiments as described above. The obtained results from the analysis of different sodium ions on the cloud behavior of the X-AES/SXS stock solution are shown in Figure 3.22. Again, a transition from clear to turbid is observed with increasing temperature for all salts. All monovalent "salting-out" anions decrease the cloud temperature of the extended surfactant/hydrotrope mixture, while all monovalent "salting-in" anions decrease it at low salt concentrations followed by an increase at higher salt concentrations. Again, this is expected from the Hofmeister series. The slope of the decrease in cloud temperature of the "salting-out" ions is smaller than for the surfactant solutions without SXS. Hence, much more salt is necessary to reach a turbid solution at 0 °C. Most interestingly, all investigated divalent salts behave like a "salting-in" electrolyte in a solution of X-AES/SXS (mole ratio
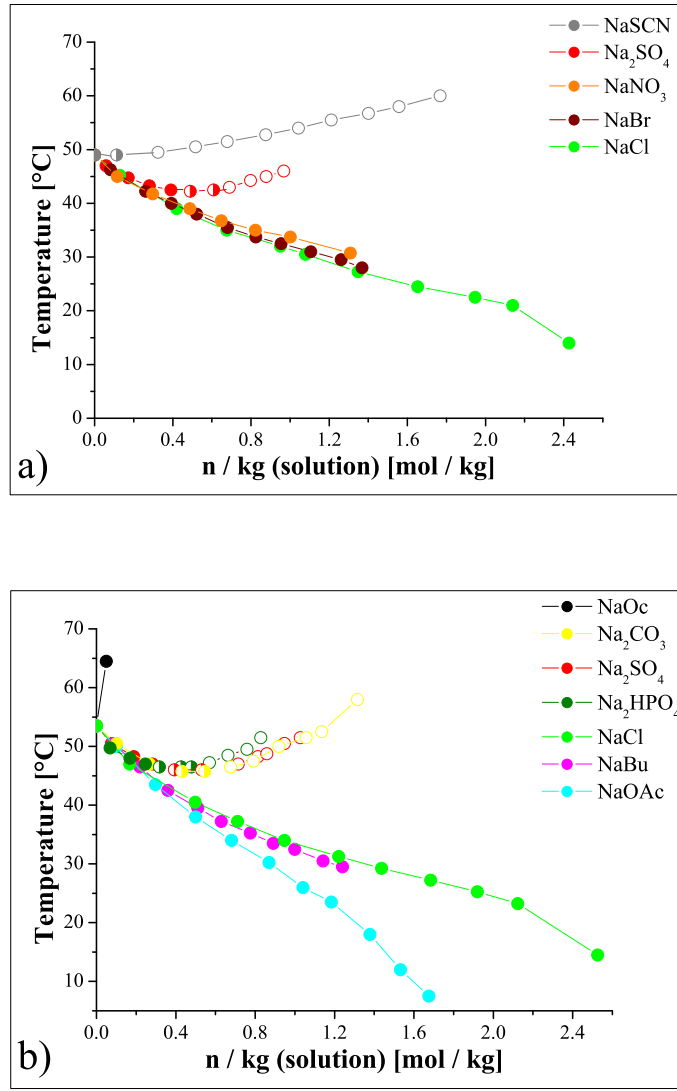
Figure 3.22: Influence of different anions on the phase behavior of a X-AES/SXS stock solution (mole ratio R = 0.5): (a) batch No. 8625-2: [●, ◑, ○] NaSCN, [●, ◑, ○] Na_2SO_4, ● $NaNO_3$, ● NaBr, ● NaCl, (b) batch No. 8625-47: ● NaOc, [●, ◑, ○] Na_2CO_3, [●, ◑, ○] Na_2SO_4, [●, ◑, ○] Na_2HPO_4, ● NaCl, ● NaBu, ● NaOAc. Samples are clear below the curves and turbid above. The curves with the filled symbols show a $L_1 \rightarrow L_\alpha$ phase transition, while the curves with the empty symbols show a $L_1 \rightarrow L_1$'. For the half filled symbols a phase transition to both L_α and L_1' arises.

R = 0.5). Therefore, the cloud temperature decreases at low salt concentrations and increases at high concentration. This effect is not expected from the Hofmeister series.

Observations obtained from optical microscopy measurements gave analogue results
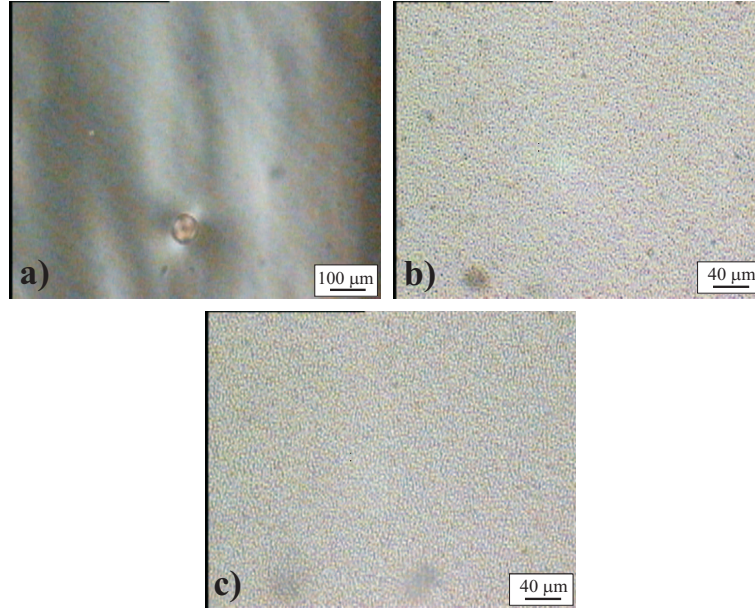
Figure 3.23: Optical microscopy images of an X-AES/SXS (mole ratio R = 0.5) solution with different salts showing two possible routes of phase transition using crossed polarizers. a) $L_1 \rightarrow L_\alpha$ phase transition of 0.4 mol/kg NaCl at 75 °C ("salting-out", birefringent); b) $L_1 \rightarrow L_1$' phase transition of 0.05 mol/kg NaSCN at 56 °C (salting-in", droplets); (c) $L_1 \rightarrow L_1$' phase transition of 0.8 mol/kg Na_2SO_4 at 70 °C ("salting-in", droplets).

to those obtained for the solutions without SXS (Figure 3.23). All "salting-out" ions show, as expected a transition from a clear solution to a lamellar phase ($L_1 \rightarrow L_\alpha$). Starting from small droplets at the cloud temperature, which are expected to be lamellar phase dispersion (Section 3.1), the droplets grow larger (birefringent), and turn into a L_α phase. However, the appearing lamellar phase has lost intensity in comparison to the L_α phase without SXS. Much more light and higher concentrations of salt were necessary to observe birefringence under the microscope. Furthermore, no birefringence was observed for NaSCN, NaOc and all divalent ions (Na_2SO_4, $NaNO_3$, etc). Again, at low salt concentrations a $L_1 \rightarrow L_\alpha$ phase transition occurs, which is shown by a decrease of the cloud temperature. At the minimum of the curve, a lamellar phase coexists with larger droplets. Once the cloud temperature increases again, only large droplets can be seen under the microscope without the appearance of a lamellar phase ($L_1 \rightarrow L_1$').

^{1}H-NMR measurements were performed to get more details about the phases formed above the clouding (before and after addition of SXS). To this purpose, the samples

were left to equilibrate above the cloud temperature for three to four weeks. Afterwards, if two distinct layers were observed, the phases were separated from each other and NMR samples were prepared as described in the Experimental Section 2.2. The amount of surfactant in the two phases was calculated using the integration of the terminal methyl triplet in comparison to a standard added to the solutions (acetone).
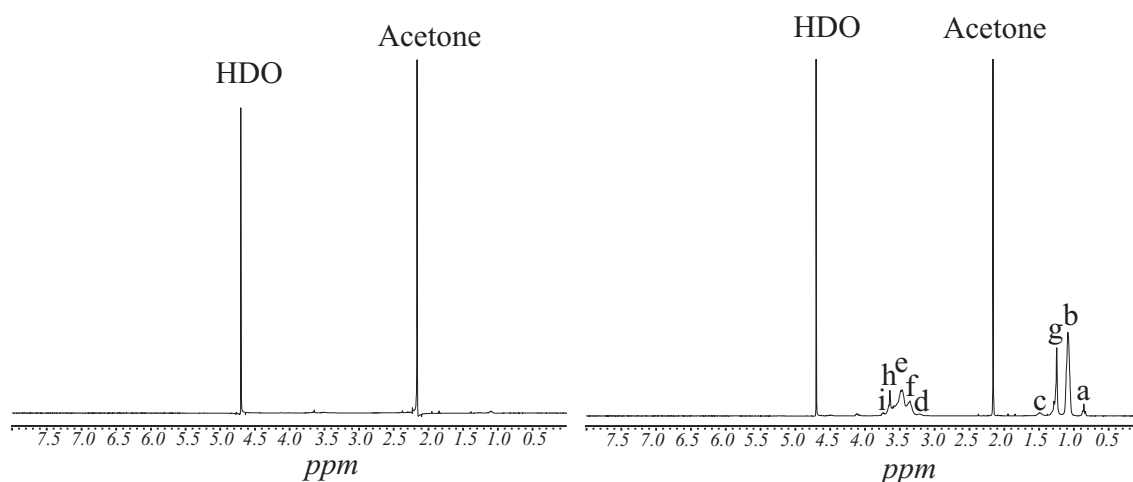
Figure 3.24: ^{1}H-NMR spectra of the separated phases at 40 °C of a 23 wt% X-AES solution containing 0.8 mol/kg NaCl; (left) lower phase; (right) upper phase. The assignment of the peaks is given in Figure 3.7.

There were two possibilities for the samples to equilibrate at the temperatures above the cloud temperature. On the one hand, a phase separation occurred into a lamellar phase (birefringence observed under crossed polars) and a clear solution. In this context, the upper phase consisted of 84% surfactant and 16% water and salt, while the bottom phase consisted of 1% surfactant and 99% water and salt. Hence, at the cloud temperature a phase separation of a L_1 phase (water, salt, small amounts of surfactant) and a surfactant rich phase, bicontinuous cubic V_2 or reverse hexagonal H_2 phase (surfactant, salt, small amounts of water) appears (Figure 3.24). This effect was observed for all salts, which decrease the cloud temperature in both cases: the 23 wt% surfactant solution and the X-AES/SXS mixture. On the other hand, no macroscopic phase separation occurred for NaOc, NaSCN, and all divalent ions in the mixture of X-AES/SXS. Additionally, no birefringence was observed.
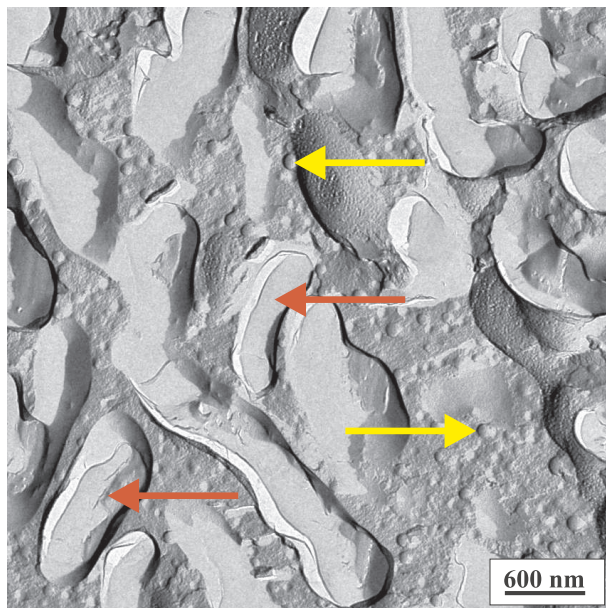
Figure 3.25:   TEM image of a freeze-etched (FE) solution of 0.4 mol/kg Na_2SO_4 in X-AES/SXS/water with a mole ratio of R(X-AES/SXS) = 0.5. Red arrows point to large, irregular-shaped droplets and yellow arrows show small, spherical droplets.

In addition to the optical microscopy results, micrographs of freeze-etched samples were taken within the turbid region from the surfactant/hydrotrope solution containing Na_2SO_4. It could be shown that the solution consists of large droplets (width: 0.5-2 μm, length: 2-6 μm, red arrow in Figure 3.25), which are irregular and long-shaped ("potato-like"). Additionally, smaller droplets can be seen with an approximate diameter of 60-80 nm (yellow arrows in Figure 3.25). The small droplets cannot be seen by polarizing light microscopy. However, the large droplets are consistent with the droplets seen around the cloud temperature. This result was compared to the results from the optical microscopy measurements and the equilibrium measurements. It seems that the large, "potato-like" and the smaller droplets must be a surfactant rich phase containing almost all the surfactant.

Effect of Cations on the Cloud Point of X-AES

a) X-AES in Aqueous Electrolytes.
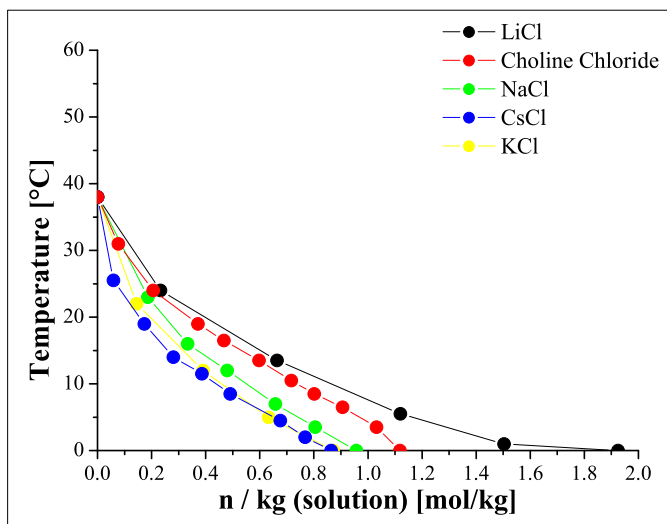
Figure 3.26: Influence of different cations on the phase behavior of the extended surfactant X-AES (batch No. 8625-2): ● LiCl, ● Choline Chloride, ● NaCl, ● CsCl, and ● KCl. Samples are clear below the curves and turbid above.

The effect of various cations on the cloud temperature of a 23 wt% X-AES stock solution (equivalent to 0.18 mol L^{-1}) was also studied by varying the concentration of different chloride salts (LiCl, choline chloride, NaCl, CsCl, and KCl). The results of the "pseudo"-binary system (water/X-AES/cation) are shown in Figure 3.26. Above a critical temperature, a transition from clear to turbid is observed for all salts. However, in comparison to the anions, all cations decrease the cloud temperature of the surfactant with increasing concentration. The order of the salts decreasing the cloud temperature follows precisely the same behavior as expected from the Hofmeister series.[114, 115]

As for the anions, the phase transition of the cations was studied by optical microscopy for a better understanding of the mechanism. In this case, only the phase transition from a clear solution to a lamellar phase can be found for all the salts (L$_1$ → L$_\alpha$). Again, in the beginning of the turbidity, droplets are seen, which should

be birefringent and a lamellar phase dispersion (Section 3.1). These droplets grow larger by increasing the temperature indicating birefringence.

b) X-AES/SXS in Aqueous Electrolytes.
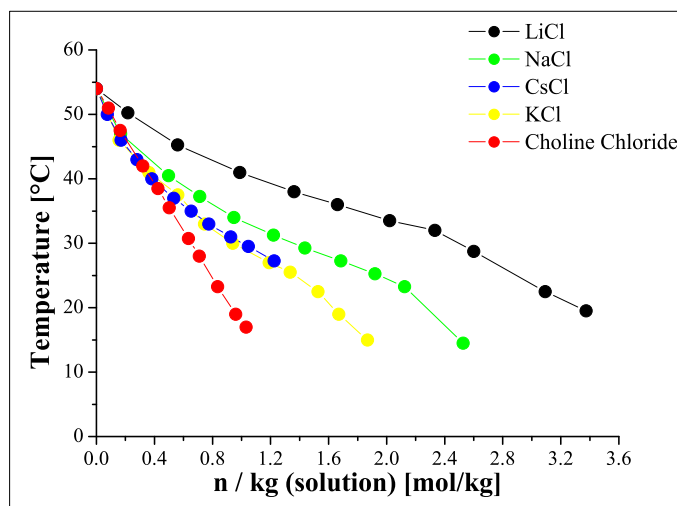
Figure 3.27: Influence of different cations on the phase behavior of X-AES (batch No. 8625-47)/SXS (mole ratio R = 0.5): ● LiCl, ● NaCl, ● CsCl, ● KCl, and ● Choline Chloride. Samples are clear below the curves and turbid above.

Furthermore, the influence of cations on a stock solution containing a mole ratio of R(X-AES/SXS) = 0.5 was studied by varying the concentration of the mentioned chloride salts (Figure 3.27). Again, as the temperature of the systems increases, a transition from clear to turbid is observed for all salts. The order of the salts decreasing the cloud temperature follows precisely the same behavior as expected from the Hofmeister series.[114, 115]

In this case, the hydrotrope SXS has nearly no influence on the phase behavior of the surfactant/water/salt system. Again, the slope of decrease in cloud temperature of the "salting-out" ions is flatter than obtained for a surfactant solution without SXS. Thus, much more salt is necessary to achieve a turbid solution at 0 °C. However, this effect cannot be seen for choline chloride, which has the same slope before and after addition of SXS. Also for this case, the phase transition of the cations

in a surfactant/hydrotrope solution was studied by optical microscopy for a better understanding of the mechanism. As already observed from the "pseudo"-binary phase diagram, only the phase transition from a clear solution to a lamellar phase ($L_1 \rightarrow L_\alpha$) can be found for all the salts.

3.2.3 Discussion

a) Anion Effect

The transition from clear to turbid of an aqueous X-AES solution without additive requires a transition from small micelles (6 nm) to a lamellar phase. Disc-like, rather than prolate, micelles are suggested to be close to the lamellar phase. This transition requires a reduction in aggregate curvature. As the curvature is reduced, an abrupt increase in N_{mic} occurs. A decrease in the intra-micellar curvature must occur because the inter-head-group repulsions are reduced or because the hydrophobic tails adopt more extended configurations (see section 3.1). A reduction of the inter-head-group repulsions could arise from a reduced hydration of the EO groups because of the lower water activity in the presence of concentrated electrolytes.

It is well known that various sodium salts added to a surfactant solution have a significant influence on the phase behavior.[106, 107, 113, 188]

Addition of "salting-out" (kosmotropic) electrolytes to an aqueous solution of X-AES enhances the transition from clear to turbid (lamellar phase formation). Due to electrostatic screening, the negatively charged micelles become more and more neutral. The head-group repulsion is reduced further, followed by a reduction of the aggregate curvature, and the area per molecule. All those effects lead to a faster formation of the lamellar phase at lower temperatures. The more salt is added, the more screening and less repulsion between the head-groups appears. In addition, due to the decrease in head-group repulsion, the micelles get flatter and form infinite layers of (sticky) discs, a lamellar phase. Hence, the cloud temperature decreases with increasing salt concentration and cooling is necessary to obtain clear solutions. This effect is mainly an intra-micellar effect rather than an inter-micellar effect and occurs only for "salting-out" salts.

Furthermore, the addition of a co-surfactant (NaOc) to the solution leads to a lamel-

lar phase formation; however, the cloud temperature of the surfactant is increasing. The effect is seen at the lowest level of added NaOc. X-AES and NaOc form mixed micelles, where the micelles have a larger curvature because of the very much smaller chain size of NaOc. Hence, increasing of the cloud temperature is simply due to the formation of smaller micelles.

For NaSCN (chaotropic) and SXS (hydrotrope) the cloud temperature decreases at first, followed by a sharp increase at higher salt concentrations. The decrease at low concentrations is synonymous with the phase transition already described before. Electrostatic screening leads to a reduction of the head-group repulsion followed by a lamellar phase formation. At a certain salt concentration, an inversion of the slope appears for those salts (Figure 3.20). A transition from a micellar (L_1) to a turbid solution with large droplets (L_1') is observed. Chaotropes have a low charge density and a less tightly bound hydration shell, which results in a higher association with non-polar surfaces and in this case at the surfactant water interface (the micelle). In addition, hydrotropes adsorb on the surface of the micelle. Both of these result in an increasing head-group area and an increased micelle curvature. Therefore, smaller micelles with a larger head-group are obtained. Before the addition of salt, strong inter-micellar repulsion exists between the micelles. After the addition of salt, the micelles become smaller and the repulsions are reduced. However, the phase separation of a micellar solution requires the presence of an inter-micellar attractive force. The origin of this is at present unknown.

In a last step, all the mentioned electrolytes were added to a solution of X-AES/SXS (mole ratio R = 0.5) in water. All monovalent anions decrease the cloud temperature with a phase transition from $L_1 \rightarrow L_\alpha$. However, the slope of the clouding-curve is much flatter in comparison to the curves without SXS. As previously mentioned, SXS adsorbs on the surface of the micelles, decreases the size of the micelle and increases the head-group, the curvature, and the area per molecule of the micelle. Smaller micelles are observed being more negatively charged (due to adsorption of SXS on the micelle). More salt is necessary to screen the charge and to enhance the lamellar phase formation. Thus, the obtained curves are flatter.

All "salting-out" effects are caused by the presence of larger micelles, which is due

to a reduced head-group repulsion; first, from a reduction of the intra-micellar electrostatic repulsion and second, from a reduced hydration of the head-group.

The "salting-in" effect for NaSCN and NaOc is the same as observed in solutions without SXS.

However, all divalent anions show exactly the same behavior as NaSCN or SXS in an aqueous solution of X-AES. At low salt concentrations, divalent ions screen the charge of the negatively charged micelles and thus, decrease the cloud temperature, which is an intra-micellar interaction. At higher salt concentrations, all divalent electrolytes are "salting SXS out" from the aqueous phase into the X-AES aggregates. Therefore, SXS rather adsorbs on the micelle than remaining in the aqueous electrolyte phase. All the SXS is inside the micelles and the same effect is arising as already described for "salting-in" ions. Much more salt and higher temperatures are necessary to obtain a turbid solution. In addition, smaller droplets arise, which coalescence to larger droplets.

b) Cation Effect

The effect of cations on the phase behavior of X-AES/water and X-AES/SXS/water is not as significant as for anions. One contributing reason for this is that the cations are always mixed because the systems always contain the initial level of Na^+ counterions from X-AES/SXS. Hence, particularly for low electrolyte additions, the Na^+ ions are present in excess. Only a "salting-out" effect is observed, which follows precisely the Hofmeister series. The mechanism for the transition is the same as already mentioned for all "salting-out" anions.

After the addition of these salts to a solution of the extended surfactant and SXS (mole ratio R(X-AES/SXS) = 0.5), the slope of the curves is much flatter, again, this effect is the same as already described. However, it is notable that choline chloride, which was the least "salting-out" electrolyte in solutions without SXS, is the most "salting-out" electrolyte with SXS. The slope of the choline chloride curves in both solutions is almost exactly the same. Two possible explanations can be the reason for this effect. On the one hand, this may be because both choline and xylene sulphonate ions jointly bind to the micelles and hence, together they screen the

charge on the head-groups more effectively. On the other hand, it was already shown by Vlachy et al. that the choline ions bind strongly on the sulfate head-group.[118] Compared to this interaction, the role of SXS is of much lower importance. The phase behavior does not change with or without SXS in the system.

3.2.4   Concluding Remarks

The effect of anions on an aqueous solution of X-AES and of X-AES/SXS (mole ratio R = 0.5) in regards of their influence on the cloud temperature of X-AES was studied in detail. It was shown that in a solution without SXS, all anions behave as expected from the Hofmeister series ($Na_2SO_4 = Na_2CO_3 > Na_2HPO_4 > NaOAc > NaBu > NaCl > NaBr > NaNO_3 > NaSCN > SXS > NaOc$). A transition from a micellar solution (L_1) to a lamellar phase (L_α) was observed for all "salting-out" salts and NaOc. This is an intra-micellar interaction due to a change in micelle curvature the disc-like micelles grow larger and stick together to a lamellar phase. Furthermore, a second transition from a micellar solution (L_1) to a solution with large droplets (L_1') was obtained for all "salting-in" salts. The "salting-in" anions adsorb on the micelle and hence, decrease the size of the micelle. Smaller micelles with a larger head-group are obtained and the cloud temperature is increased.

However, adding anions to an aqueous solution of X-AES/SXS shows a dramatically change in the order of the anions. All divalent "salting-out" anions change their behavior towards a "salting-in" salt ($NaOAc > NaBu > NaCl > NaBr > NaNO_3 > Na_2SO_4 = Na_2CO_3 = Na_2HPO_4 > NaSCN > NaOc$). This effect was explained by the fact that all divalent ions tend to "salt-out" the remaining SXS ions in the aqueous solution and hence, push these molecules inside the micelles. The resulting effect is then similar to the effect of "salting-in" ions.

The effect of cations on the solubility of X-AES follows the Hofmeister series (KCl > CsCl > NaCl > choline chloride > LiCl). All added cations were "salting-out". However, in solution with SXS, the effect is not as pronounced as for anions. All salts increase their slope of the cloud temperature curve, except choline chloride (choline chloride > KCl > CsCl > NaCl > LiCl).

3.3 Effect of Salts on the Phase Behavior and the Stability of Nano-Emulsions with Rapeseed Oil and an Extended Surfactant

3.3.1 Introduction

As previously mentioned in Chapter 1, it is more difficult to solubilize triglycerides into microemulsions than hydrocarbons or alkyl mono-esters. The reason for these difficulties is the complex structure of the triglyceride molecule in comparison to lower molecular weight oils. Triglycerides are esters of fatty acids combined with glycerol. The long and bulky alkyl chains lead to a highly hydrophobic molecule, while the ester regions cause high polarity. The combination of both results in a poor solubilization of these substances by surfactants (see Section 1.3).

The effect of salts on the solubility of triglycerides in water with extended surfactants and the stability of the resulting nano-emulsions has never been investigated in detail. Nano-emulsions are transparent or translucent systems with a particle size between 20 and 200 nm. In contrast to microemulsions, nano-emulsions are non equilibrium systems with highly kinetic stability. Consequently, these systems are not formed spontaneously and have the tendency to separate into the constituent phases.

In this section of the thesis, different types of phase diagrams will be discussed showing the efficiency of the extended surfactant X-AES (Figure 2.1) to mix water and triglycerides. A system with the anionic surfactant X-AES, a hydrotrope (sodium xylene sulfonate, SXS, Figure 2.2), and rapeseed oil in water was studied. Since those components do not form any kind of nano-emulsions without the addition of electrolytes, different kind of salts (NaCl, NaSCN, NaOAc, Na_2SO_4, $NaNO_3$, KCl, CsCl and choline chloride) were added in different concentrations and phase diagrams were recorded. These diagrams and the nano-emulsion stability will be discussed with respect to the Hofmeister series.[114, 115] The different phases appearing with increasing temperature were characterized using conductivity measurements and optical microscopy. In addition, dynamic light scattering experi-

ments gave information about the stability of the nano-emulsions. Finally, the phase transition mechanism will be discussed.

3.3.2 Results

The effect of different salts on the formation of nano-emulsions was studied by changing the concentration of either the anion of various sodium salts or the cation of different chloride salts as a function of the temperature.

A) Effect of Anions on the Formation of Nano-Emulsions

a) Phase Diagrams

The phase diagrams of the sodium salt/surfactant/SXS/water/rapeseed oil systems as a function of temperature are shown in Figure 3.28. The chosen sodium salts were Na_2SO_4 (Figure 3.28a), NaOAc (Figure 3.28b), NaCl (Figure 3.28c), $NaNO_3$ (Figure 3.28d), and NaSCN (Figure 3.28e). Two different types of phase diagrams were observed.

The first type of phase diagram shows two clear domains with increasing temperature and was observed for NaOAc, NaCl, and $NaNO_3$. The first clear region appears for a large temperature (starting from 0.0 °C) and salt concentration range. By increasing the temperature of the clear samples, a transition to a birefringent phase occurs and the solutions become turbid (cloud temperature, observed with crossed polars). This cloud temperature decreases with increasing salt concentration, which is expected for "salting-out" salts from the Hofmeister series and is in agreement with previously described results on the effect of salts on a X-AES/water/hydrotrope solution without triglycerides (Section 3.2). Further increase of the temperature leads to a second clear domain at higher temperatures. This clear area exists only for a small temperature and a reduced salt concentration range, compared to the first domain. Again, the temperature for the appearance and disappearance of the clear solutions decreases with increasing salt concentration (NaOAc, NaCl, and $NaNO_3$, Figure 3.28 b-d). At high temperatures, above the second clear region, a birefringent phase is formed again.

It is worth to mention that the topology of those three phase diagrams looks very
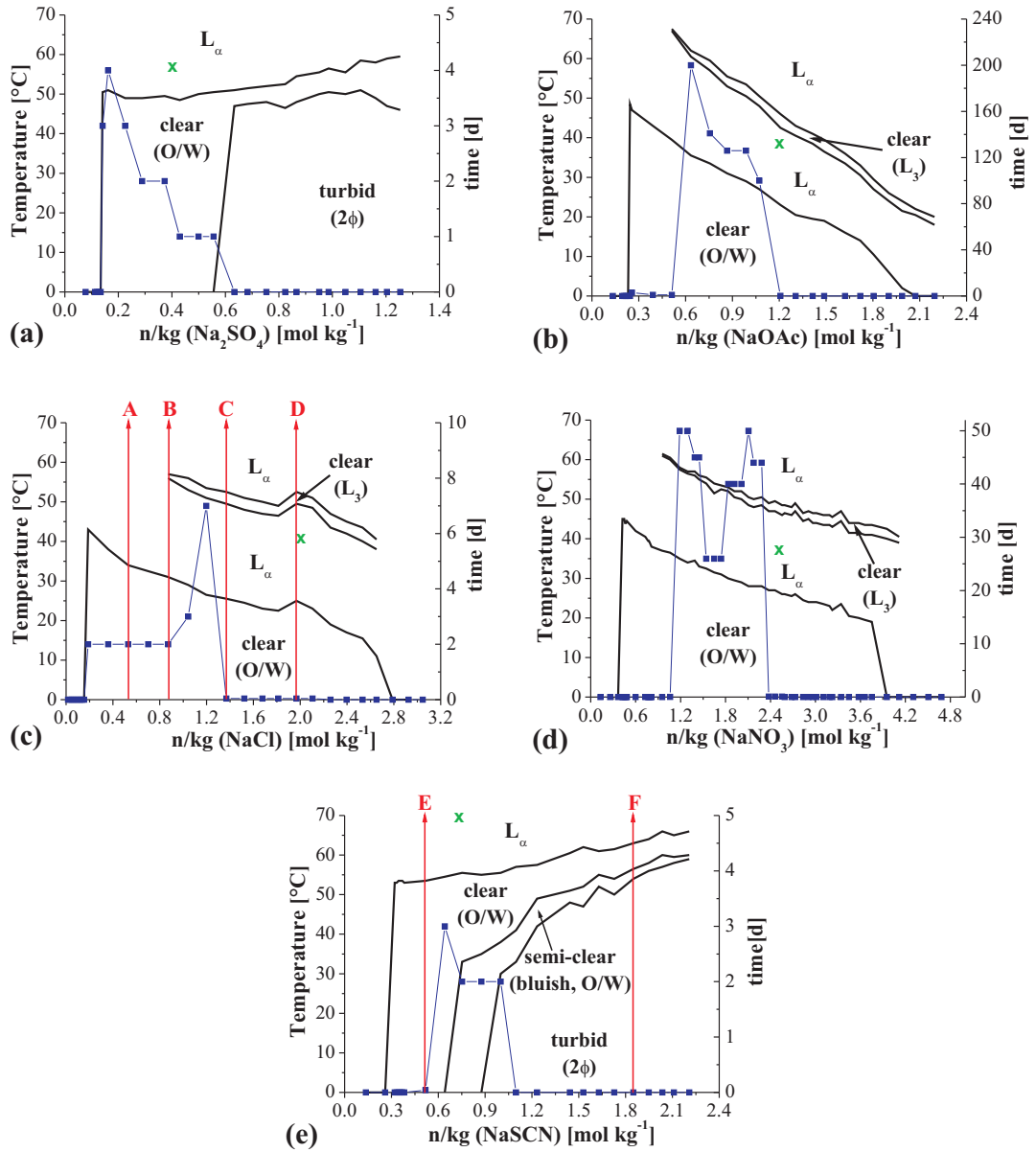
Figure 3.28: Phase diagrams of the sodium salt/surfactant/SXS/water/rapeseed oil systems as a function of temperature [°C]. (■) gives the time stability of the nano-emulsions in days [d] at 21.0 °C. The starting formulations, without additional salt, consisted of 62.5 wt% water, 18.0 wt% X-AES, 5.5 wt% SXS, 14.0 wt% rapeseed oil. (a) Na_2SO_4, (b) NaOAc, (c) NaCl, (d) $NaNO_3$, (e) NaSCN. The clear, semi-clear (bluish), liquid crystalline, and turbid regions are shown in the diagram. The red arrows (A-F) give the chosen paths for conductivity measurements. The green x symbolizes the composition and temperature for microscopy images shown in Figure 3.29.

similar. The minimum quantity of salt, to obtain a clear solution at 0.0 °C, is between 0.13-0.26 mol/kg for NaOAc, 0.15-0.19 mol/kg for NaCl, and 0.36-0.48 mol/kg

for $NaNO_3$. The maximum temperature at which clear solutions are obtained (first clear region) is reached at 47.0, 43.0 and 44.5 °C for NaOAc, NaCl and $NaNO_3$, respectively. However, the slope of the cloud temperature of the three different salts is negative and increases in the order of NaOAc (-23.4 °C kg/mol), NaCl (-10.1 °C kg/mol), $NaNO_3$ (-6.8 °C kg/mol), which is in agreement with the Hofmeister series. The extent of the second clear domain as a function of temperature is largely reduced in comparison to the first clear area. The minimum salt concentration required to observe this area is 0.51, 0.87 and 0.95 mol/kg for NaOAc, NaCl and $NaNO_3$, respectively. This is higher than for the first clear region. The slopes of the lower and the upper boundary of the second clear domain are similar and almost parallel to the slope of the upper boundary of the first domain.

The second type of phase diagrams shows only one clear domain over the whole temperature and salt concentration range and was observed for the "salting-in" salt NaSCN and for the most "salting-out" divalent electrolyte Na_2SO_4 (Figure 3.28a and e). The behavior of NaSCN is in agreement with the Hofmeister series. However, the phase diagram of Na_2SO_4 should be more similar to the ones described above (Figure 3.28c-d). This different behavior is due to the presence of SXS and was already described and explained in the last Section 3.2.

The phase diagrams obtained in the presence of Na_2SO_4 (Figure 3.28a) and NaSCN (Figure 3.28e) show similar topologies. However, in comparison to the previous described diagrams (Figure 3.28b-d), the main topology is completely different. Increasing the temperature from 0.0 to 70.0 °C, only one clear region was observed. Focusing on this region, the minimum salt concentration to obtain a clear solution at 0.0 °C is between 0.08-0.16 mol/kg for Na_2SO_4 and 0.25-0.38 mol/kg for NaSCN. The maximum temperature, at which these solutions appear clear, is reached at 51.0 and 53.0 °C for Na_2SO_4 and NaSCN, respectively. Hence, these temperatures are higher than for the other three sodium salts. The slope of the upper boundary is positive for the two electrolytes and a value of 10.1 °C kg/mol for Na_2SO_4 and 7.6 °C kg/mol for NaSCN can be determined. However, the extent of the clear region is reduced in comparison to the previously described phase diagrams.

Solutions with a Na_2SO_4 concentration above 0.56 mol/kg appear turbid at 0.0 °C,

become clear above 45.0 °C, and turn turbid again at higher temperatures.

For NaSCN, a semi-clear (very bluish) area was observed between 0.64 and 0.88 mol/kg, which becomes completely clear above 30.0 °C. Solutions with concentrations over 0.88 mol/kg appear turbid at 0.0 °C, fade into a semi-clear (very bluish) area above 30.0 °C and then into a clear area over 35.0 °C. A turbid solution is obtained at high temperatures, above the clear region. The temperatures for these changes increase with increasing NaSCN concentrations. The turbid NaSCN and Na_2SO_4 samples at high temperatures show birefringence using crossed polars.

In addition, the same compositions as used for the phase diagram with NaCl (Figure 3.28c) were prepared with olive oil instead of rapeseed oil on the one hand, and with sodium cumene sulfonate (SCS, Figure 1.7) instead of SXS on the other hand. The resulting phase diagrams are shown in the Appendix (Figure 3.42 and Figure 3.43). However, no significant difference in comparison to the phase diagram in Figure 3.28c was observed and therefore, the phase diagrams will not be discussed in detail.

b) Optical Microscopy

Optical microscopy as a function of temperature was used to get more information on the different structures within the clear and turbid regions of the phase diagram. Images of different salts at various temperatures are shown in Figure 3.29 and are symbolized with a green x in Figure 3.28.

Two clear regions were observed for NaOAc, NaCl, and $NaNO_3$ using optical microscopy. A few droplets were seen within the first clear region (> 5 μm). These droplets are suggested to be oil-droplets in equilibrium with a micellar solution (O/W nano-emulsion). Increasing the temperature, the solutions turn turbid and a lamellar phase is observed, which was clearly identified using crossed polars (Figure 3.29b-d). This lamellar phase disappears with the appearance of the second clear domain within the phase diagram. Again, a few small droplets can be seen under the microscope (> 5 μm). Further increase of the temperature leads to a turbid solution, which also shows birefringence (lamellar phase).

Only one clear region is observed for NaSCN and Na_2SO_4 at low temperatures and
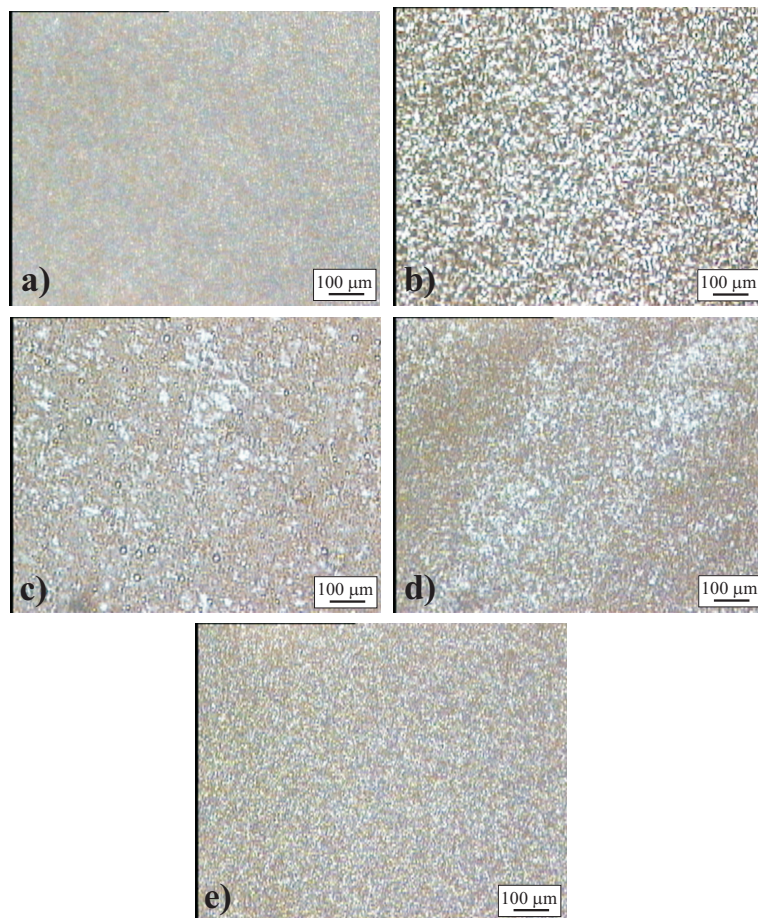
Figure 3.29: Optical microscopy images of a sodium salt/surfactant/SXS/water/rapeseed oil mixtures (symbolized with a green x in Figure 3.28). (a) 0.43 mol/kg Na_2SO_4 at 57.0 °C (lamellar phase, L_α); (b) 1.21 mol/kg NaOAc at 39.0 °C (lamellar phase, L_α); (c) 2.10 mol/kg NaCl at 42.0 °C (lamellar phase, L_α); (d) 2.46 mol/kg $NaNO_3$ at 38.0 °C (lamellar phase, L_α); (e) 0.75 mol/kg NaSCN at 70.0 °C (lamellar phase, L_α).

lower salt concentrations. This clear region also shows a few droplets (> 5 μm, again oil-droplets in a O/W nano-emulsion). At higher salt concentrations and low temperatures, a bluish or turbid solution is observed showing large droplets under the microscope (> 20 μm). Depending on the temperature and the salt concentration, less (bluish region) or more and larger (turbid region) droplets were obtained. Increasing the temperature of these samples, the droplets disappear and a clear region including a few smaller droplets (> 5 μm) is observed. Above the clear region, the solutions turn turbid and a lamellar phase is obtained under the microscope using crossed polarizers. It is important to mention that more light was necessary

to observe the lamellar phase, in comparison to the other three salts described above.

c) Conductivity
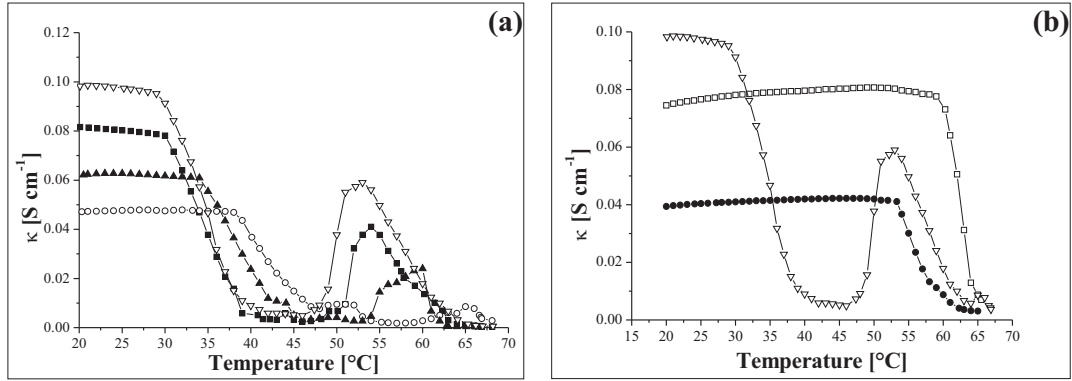
Figure 3.30: Specific conductivity [S/cm] as a function of temperature [°C]. (a) Comparison of different NaCl concentrations: (○) 0.53 mol/kg (path A in Figure 3.28c), (▲) 0.87 mol/kg (path B in Figure 3.28c), (■) 1.37 mol/kg (path C in Figure 3.28c), and (▽) 1.97 mol/kg (path D in Figure 3.28c). (b) Comparison of NaSCN and NaCl: (▽) 1.97 mol/kg NaCl (path D in Figure 3.28c), (●) 0.52 mol/kg NaSCN (path E in Figure 3.28e), (□) and 1.85 mol/kg NaSCN (path F in Figure 3.28e).

Temperature dependent conductivity measurements were performed for samples with different NaCl (path A-D in Figure 3.28c) or NaSCN (path E and F in Figure 3.28e) concentrations. A comparison of the conductivity data at different NaCl concentrations is shown in Figure 3.30a. Varying NaSCN concentrations together with the highest NaCl concentration are plotted in Figure 3.30b. The temperature was constantly increased during the measurements starting from 20.0 °C up to 68.0 °C.

As expected, the conductivity increases with increasing NaCl concentration (Figure 3.30a). Two maxima are observed for the nano-emulsions with NaCl. The first maximum is a plateau which appears between 20.0-35.0 °C for 0.53 mol/kg (path A in Figure 3.28c, (○) in Figure 3.30a), 20.0-31.0 °C for 0.87 mol/kg (path B in Figure 3.28c, (▲) in Figure 3.30a), 20.0-36.0 °C for 1.37 mol/kg (path C in

Figure 3.28c, (■) in Figure 3.30a), and 20.0-26.0 °C for 1.97 mol/kg (path D in Figure 3.28c, (▽) in Figure 3.30a). This plateau region equals to the first clear region in the phase diagram (see Figure 3.28c). An O/W nano-emulsion (with excess oil) is observed in this region. The high conductivity arises from the water-rich phase containing the total salt concentration. Increasing the temperature, the conductivity decreases (Figure 3.30a), which is in agreement with the appearance of the (turbid) lamellar phase in the phase diagram (Figure 3.28c). It is well known that the conductivity within a lamellar phase decreases due to the presence of the surfactant layers. A lamellar phase does not consist of one infinite connected channel from one end to the other, especially not with this surfactant, which shows a very disordered lamellar phase (see Section 3.1).

Above 60.0 °C for 0.53 mol/kg, 53.0 °C for 0.87 mol/kg, 46.0 °C for 1.37 mol/kg and 1.97 mol/kg NaCl, the conductivity increases again. This increase is not pronounced for the lowest NaCl concentration, but rather sharp for the highest NaCl concentration. Furthermore, it appears in a region of the phase diagram (Figure 3.28c) where the samples start to become less viscous and clear again. The conductivity increase results in a maximum at 66.0 °C for 0.53 mol/kg, 57.5 °C for 0.87 mol/kg, 53.5 °C for 1.37 mol/kg, and 52.5 °C for 1.97 mol/kg and appears within the second clear region of the phase diagram. Due to the relatively high conductivity in this region and the very low oil content, a W/O nano-emulsion (with excess water) can be excluded. A L_3 phase with a bicontinuous structure can be expected for this clear region. In a bicontinuous L_3 structure a connected system is present and therefore, the conductivity increases in comparison to the L_α phase. However, the conductivity of the L_3 phase is lower than observed for the O/W nano-emulsion at lower temperatures. This is due to the fact that charge carriers have a higher probability to move freely in a water continuous than in a bicontinuous phase. Further increase of the temperature results in a decrease of the conductivity, which is consistent with the formation of the second L_α phase above the L_3 phase.

A comparison between two NaSCN (E and F in Figure 3.28e, (●) and (□) in Figure 3.30b) and the highest NaCl (D in Figure 3.28c, (▽) in Figure 3.30b) concentration was made. The topology of the conductivity versus temperature curve

of the two salts is completely different. Only one large plateau is obtained for both NaSCN concentrations. When comparing the conductivity results of the two NaSCN concentrations, no major differences were observed. The conductivity increases slightly with increasing temperature in both cases from 39.4-42.0 mS/cm for 0.52 mol/kg NaSCN (within the clear region in the phase diagram, Figure 3.28e) and from 74.5-80.7 mS/cm for 1.85 mol/kg NaSCN (within the turbid region passing through the clear region in the phase diagram, Figure 3.28e). After reaching the mentioned maximum (clear solutions obtained for both concentrations, Figure 3.28e), the conductivity decreases with further increase of the temperature. This decrease is consistent with the formation of a lamellar phase at high temperatures (path E and F in Figure 3.28e).

Due to the high starting conductivity at 20.0 °C, which increases with increasing temperature, a water continuous phase (O/W nano-emulsion with excess oil) is expected within the clear region for the 0.52 mol/kg NaSCN solution. In addition, also for the 1.85 mol/kg NaSCN solution high starting conductivity was observed. Thus, a water continuous structure, containing the complete salt concentration, coexisting with an excess oil phase is assumed. The coexisting excess oil phase leads to a turbid solution at low temperatures.

d) Stability of the Nano-Emulsions and Microscopy

The stability of the nano-emulsion in days [d] at 21.0 °C was determined and is displayed in Figure 3.28 indicated with a (■). The corresponding y-axis for the stability is shown on the right side of the phase diagrams.

It was demonstrated that most of the solutions were not stable for longer than a few hours or seven days (one week), depending on the composition. This is an evidence for rather a "macro-emulsion" or an unstable nano-emulsion than a microemulsion and was the case for Na_2SO_4 (Figure 3.28a), NaCl (Figure 3.28c), and NaSCN (Figure 3.28e). In addition, the stability of the solutions containing lower and higher NaOAc (Figure 3.28b) and $NaNO_3$ (Figure 3.28d) concentrations was also below one week. However, samples were observed with high nano-emulsion stabilities as well. This was the case for NaOAc (0.60-1.10 mol/kg) and $NaNO_3$ (1.05-2.30 mol/kg).
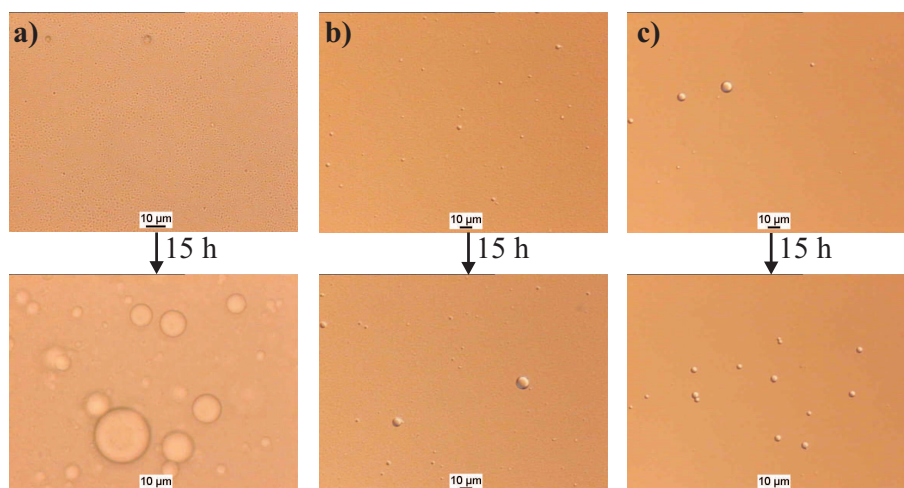
Figure 3.31: Optical microscopy images of a 0.53 (a), 0.87 (b), and 1.20 (c) mol/kg NaCl solution recorded directly after mixing the solutions (upper pictures) and after 15 hours (lower pictures).

These solutions remained clear between approximately 50 days for $NaNO_3$ and 200 days for NaOAc. Furthermore, the stability of the nano-emulsions was determined by optical microscopy. Images of a 0.53, 0.87, and 1.20 mol/kg NaCl solution before and after 15 hours are shown in Figure 3.31a-c. Small droplets were observed within the nano-emulsions, which unfortunately cannot be seen in these images, but were clearly identified using the highest resolution of the microscope. These droplets have an approximate diameter of about 200-500 nm. In addition, larger droplets with a diameter between 1 and 10 μm were observed and are shown in Figure 3.31b (top). The samples were left over night and examined again with the microscope after 15 hours (Figure 3.31, bottom). As seen in Figure 3.31a-c (bottom) the number of the small droplets has increased for all three NaCl concentrations. These results are in agreement with the time stability/instability of the nano-emulsions shown in Figure 3.28c (■). In addition, the droplets grew larger for the 0.53 mol/kg NaCl solution (Figure 3.31a) and have an approximate diameter of 5-30 μm, which is also consistent with the relatively low stability of this solution (below two days, Figure 3.28c (■)).

Additionally, it was discovered that the size of the aggregates and the stability of the solutions depends strongly on the number of heating (to 70.0 °C) and cooling (to 20.0 °C) cycles of the nano-emulsions. The nano-emulsions are only formed after

at least one heating and cooling step. This result is in agreement with the phase inversion temperature method (PIT) introduced by Shinoda and Saito.[86] Furthermore, a second heating and cooling cycle improved the stability of, e.g. the highest stable samples in Figure 3.28, from a few hours to a few days. While a third cycle improved the stability of the same samples from several days to months. According to results from the literature, the emulsification process takes place within the bicontinuous L_3 phase. By rapidly cooling the samples, the L_3 phase is disturbed due to an increased hydration of the EO groups. Therefore, the curvature changes and droplets are formed. In addition, it was shown that nano-emulsions are only formed if all the oil is solubilized inside the L_3 phase.[78, 189–191] However, due to the slow kinetics of the X-AES surfactant(Section 3.1), more heating and cooling cycles were necessary to obtain long stable nano-emulsions.

Additionally, no noticeable difference between different mixing orders was observed. All the experimental results mentioned here were repeated several times and are all reproducible.

e) Radius vs. Stability

In addition to the time stability and optical microscopy measurements, dynamic light scattering (DLS) was performed for a better comparison of the results. The obtained radius (R_H) only gives information about the trend with different NaCl concentrations and not the absolute size because the polydispersions index was always above 0.5.

Figure 3.32 ($\bigcirc$) shows R_H as a function of the salt concentration and the time stability ($\blacksquare$, Figure 3.28c and 3.32) of the solution. R_H was found to decrease with increasing NaCl concentration, until a minimum of the droplet size is reached at a NaCl concentration of 1.20 mol/kg. Further increase of the NaCl concentration leads to an increase of R_H again. The obtained R_H values are in agreement with the stability of the solutions. While R_H decreases, the stability of the solutions increases. At the minimum radius (1.20 mol/kg NaCl) a maximum of time stability arises (7 days). The radius increases and the stability of the nano-emulsions decreases again with higher salt concentrations. The solutions appear, as expected,
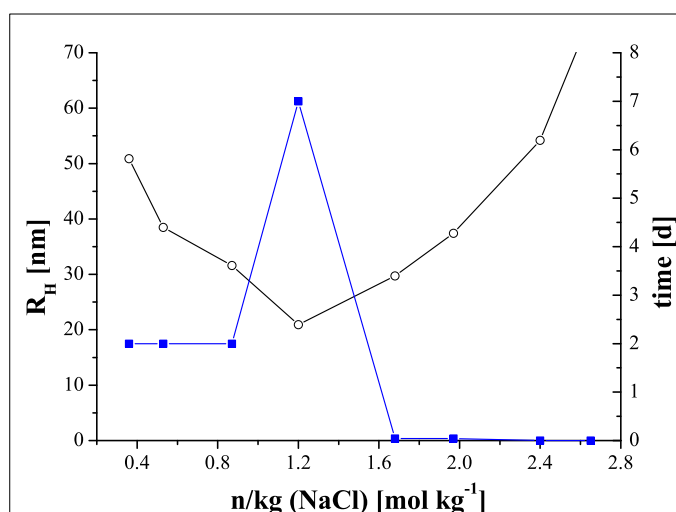
Figure 3.32: Average hydrodynamic radius, R_H, of the nano-droplets as a function of different NaCl concentrations (○). The size of the nano-emulsions is given in nm. (■) shows the stability of the solutions with the time (from Figure 3.28c).

more stable with smaller droplet sizes.

B) Effect of Cations on the Formation of Nano-Emulsions

a) Phase Diagrams

Figure 3.33 shows the phase diagrams of the chloride salt/surfactant/SXS/water/ rapeseed oil systems as a function of temperature. The chosen chloride salts were CsCl (Figure 3.33a), KCl (Figure 3.33b), NaCl (Figure 3.33c), and choline chloride (Figure 3.33d). For all chloride salts, only one type of phase diagram was observed. The obtained pattern is similar to the phase diagrams obtained for the "salting-out" sodium salts in Figure 3.28b-d. Two clear regions were observed for CsCl, KCl, and NaCl, while only one clear region was visually seen for choline chloride. However, the topology of the four phase diagrams is the same. The first clear domain seen for all cationic systems appears, as described for the anions, over a large concentration and temperature range. At a certain temperature, a transition to a (turbid) lamellar phase arises. This lamellar phase transition decreases with increasing salt concentration as expected from the Hofmeister series and is consistent with the results obtained in the previous Section 3.2. At higher temperatures, a second transition
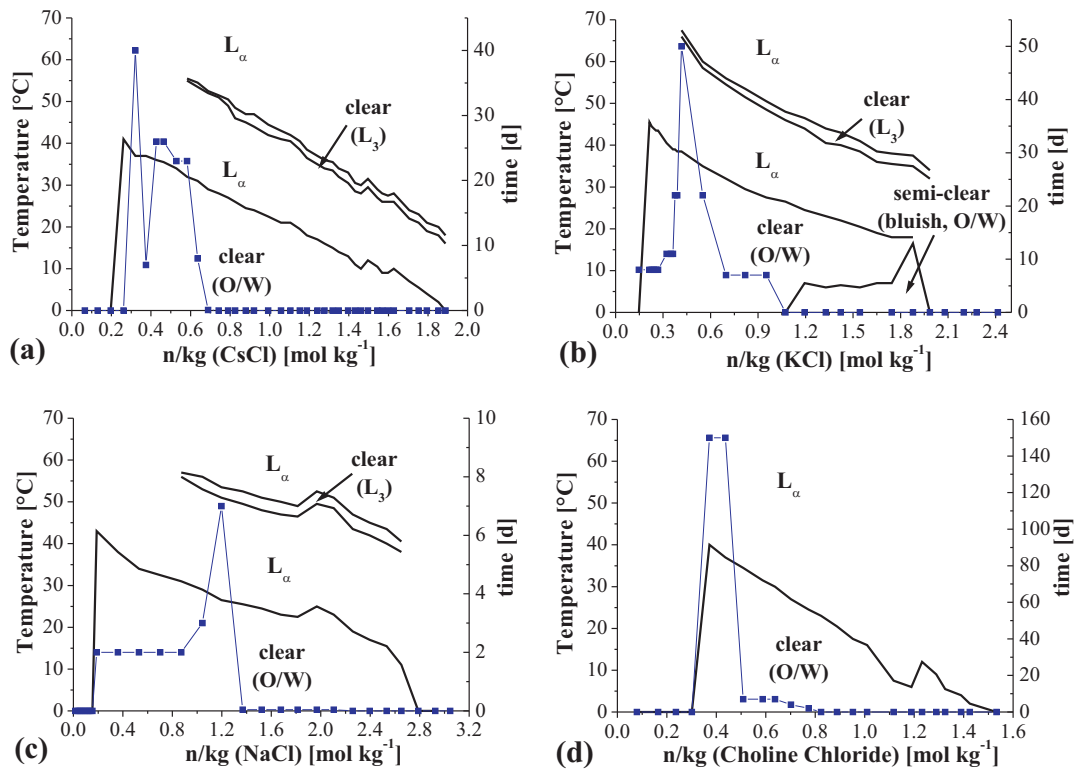
Figure 3.33: Phase diagrams of the sodium salt/surfactant/SXS/water/rapeseed oil system as a function of temperature [°C]. (■) gives the time stability of the nano-emulsions in days [d] at 21.0 °C. The starting formulations, without additional salt, consisted of 62.5 wt% water, 18.0 wt% X-AES, 5.5 wt% SXS, 14.0 wt% rapeseed oil. (a) CsCl, (b) KCl, (c) NaCl, (d) choline chloride. The clear, semi-clear (bluish), liquid crystalline, and turbid regions are shown in the diagram.

from a lamellar phase to a clear region (L_3) appears for CsCl, KCl, and NaCl. This transition temperature decreases with increasing salt concentration. The area of the second clear region is, as previously described for the anions, much smaller than the first clear region. At highest temperature, a transition from the second clear domain to a lamellar phase is observed once more. For choline chloride, the second clear region in the phase diagram could not be detected by visual observations.

The minimum quantity of salt to obtain a clear solution is between 0.20-0.26 mol/kg for CsCl, 0.15-0.32 mol/kg for KCl, 0.15-0.19 mol/kg for NaCl and 0.30-0.37 mol/kg for choline chloride (Figure 3.33a-d). The maximum temperature for the first clear domain (O/W with oil droplets) is 41.0 °C for CsCl, 40.5 °C for KCl, 43.0 °C for NaCl, and 40.0 °C for choline chloride. Hence, no significant difference between the

four salts is observed. The slope of the upper boundary of the first clear region in
the diagram is negative for all cations and increases from CsCl (-23.0 °C kg/mol) to
KCl (-14.6 °C kg/mol) to NaCl (-10.1 °C kg/mol) and decreases again for choline
chloride (-36.0 °C kg/mol). For CsCl, KCl, and NaCl a second clear region (bicon-
tinuous L_3) is observed above the first lamellar phase. In this case, the minimum of
necessary salt concentration to reach this clear region is 0.58, 0.41 and 0.87 mol/kg
for CsCl, KCl, and NaCl, respectively. The slope of the lower and the upper bound-
ary is equal to the slope of the upper boundary of the first clear domain. The second
clear area was not visually observed for choline chloride. For KCl, a semi-clear (very
bluish) area was obtained between 1.07 and 1.99 mol/kg. This area fades into the
large clear domain at elevated temperatures.

b) Stability of the Nano-Emulsions

The stability of the nano-emulsions in days [d] at 21.0 °C was also determined for
the cationic systems. The results are indicated with a (■) in Figure 3.33. The cor-
responding y-axis for the stability is shown on the right side of the phase diagrams.
Except for NaCl, all the samples had at least one concentration which was stable
for more than 40 days (e.g. 0.32 mol/kg CsCl and 0.42 mol/kg KCl). The highest
emulsion stability was observed for choline chloride with about 150 days for sam-
ples between 0.35 and 0.45 mol/kg. For the cations as well, it is worth to mention
that the stability of the nano-emulsions can be increased with increasing heating
and cooling cycles. The more often the solutions were heated the more stable the
samples appeared (as described for the anions).

3.3.3   Discussion

Two clear regions and two lamellar phase transitions were observed for all monova-
lent "salting-out" sodium salts as well as for all chloride salts.
With increasing temperature, various phase transitions were detected. A positive
spontaneous curvature is observed at low temperatures forming oil-swollen micelles
(head-groups in the water and the tails inside the micelle core filled with rape-
seed oil), which might coexists with an excess oil phase. "Salting-out" electrolytes

decrease the micelle curvature because of electrostatic screening of the negatively charged micelles. This effect was already described in the last Section 3.2. The area per head-group is reduced and the micelles get flatter and form infinite layers of (sticky) discs, a lamellar phase with water filled holes. This effect arises at the first phase transition from clear to turbid (L_α phase transition). Increasing the temperature leads to a further decrease of the micelle curvature (spontaneous curvature is close to zero) and a L_3 phase arises from the lamellar phase. This bicontinuous L_3 phase consists of polydisperse aggregates of the "V_2" structure (Section 3.1), where the aggregates are continuously fusing and breaking apart. Further increasing the temperature leads to a third reduction of the curvature and a second lamellar phase arises. In this case, the total amount of water is placed between the hydrophilic head-groups and all the oil is located between the hydrophobic tails. The detected phase transitions represent a common route for the formation of nano-emulsions and were already described in the literature.[78, 80, 87, 192]

A further change in the phase diagram arises with increasing salt concentration. As more salt was added to the solutions, more screening and less repulsion between the head-groups appeared and thus, the phase transition temperatures decrease. Therefore, cooling is necessary to obtain clear solutions at high salt concentrations. Depending on the nature and the amount of salt, more or less oil is solubilized within the micelles and thus, less or more excess oil is dispersed as droplets in the solution. Furthermore, depending on the amount of oil remaining in the solution and the size of the excess oil droplets, the nano-emulsions are more or less stable. For choline chloride, the second clear region (bicontinuous L_3) at high temperatures was not detected by visual observations. More investigations are necessary to elucidate, if this is a real effect or due to fast heating or to a very narrow temperature range.

Only one clear region was observed for the divalent "salting-out" electrolyte Na_2SO_4 and the "salting-in" electrolyte NaSCN, which turns into a lamellar phase at high temperatures. Two different routes can be described for these two salts.

On the one hand, a transition from a clear to a turbid solution can be found with increasing salt concentration. In addition, for intermediate NaSCN concentration bluish solutions were obtained between the clear and turbid region.

NaSCN has a high association with non-polar surfaces and thus, with the micelles. Additionally, the solutions contain SXS, which adsorbs on the surface of the micelles as well. These two effects lead to smaller micelles with an increased head-group area and an increased micelle curvature. Within the clear region at low salt concentrations, an oil swollen micellar solution (O/W nano-emulsion) coexisting with small amounts of excess oil is observed. Increasing the salt concentration, the micelles get smaller, which results in a loss of oil from the micelle interior into the bulk (more excess oil, bluish solutions). At high NaSCN concentrations, the micelle become even smaller and almost all the oil is displaced in the excess phase, resulting in a turbid solution. As already mentioned in Section 3.2, in solutions with SXS, Na_2SO_4 behaves more like a "salting-in" than a "salting-out" electrolyte. It was demonstrated that all divalent ions tend to "salt-out" the remaining SXS ions in the aqueous solution and hence, push the SXS molecules inside the micelles. This results in a similar effect as described for NaSCN. Due to smaller micelles with increasing salt concentration, less oil is arranged inside the micelles, while more excess oil is in the bulk. Thus, turbid solutions are obtained with increasing salt concentration.

On the second hand, a transition from a clear solution (low salt concentrations) or from a turbid to a clear solution (high salt concentrations), to a lamellar phase was observed at high temperature. A reduction in aggregate curvature occurs with increasing temperature. It arises from the increased repulsion between the hydrophobic groups with increasing temperature, which is increased due to the presence of the oil. This effect is more pronounced than the expected effect of NaSCN or Na_2SO_4 with increasing temperature (see Section 3.2). However, more measurements are necessary to confirm this assumption.

Furthermore, it was discovered that the nano-emulsions were only formed after heating the samples above the phase inversion temperature and rapidly cooling down again (PIT method, [86]). The stability of the solutions depends strongly on the number of heating and cooling cycles. The more often the samples were heated and cooled the more stable the solutions appeared. As described above, nano-emulsion formation takes place within the bicontinuous L_3 phase. For stable solutions, all the oil needs to be solubilized within this phase. According to the slow kinetics of the

used extended surfactants, more heating and cooling cycles are necessary to achieve long term stable emulsions. Ostwald ripening, which arises from the polydispersity in the solution and the difference in solubility between small and large droplets, or coalescence are the possible mechanism for the instability of the nano-emulsions. Sedimentation or creaming can be excluded because the Brownian motion and the diffusion rates within a nano-emulsion are higher than the sedimentation/creaming rate induced by the gravity force.[78, 80, 189–191]

3.3.4 Concluding Remarks

The effect of various anions and cations on the formation of nano-emulsions with triglycerides was investigated. A strong influence of the ions on the formation, the phase behavior, and the stability of the nano-emulsions was observed. Depending on the salt, a decrease (for NaOAc, NaCl, NaNO$_3$, CsCl, KCl, and choline chloride) or an increase (for Na$_2$SO$_4$ and NaSCN) of the cloud temperature arises, which is similar to the effect observed for solutions without rapeseed oil (see section 3.2).

Two clear regions were obtained for all salts decreasing the cloud temperatures. An O/W nano-emulsion with excess oil is expected, which turns into a lamellar phase, into a L$_3$, and finally into a lamellar phase with increasing temperature. An intra-micellar interaction is the reason for this behavior. Due to a change in micelle curvature, the micelles grow larger and stick together forming a lamellar phase. At higher temperatures, the curvature decreases more (spontaneous curvature equal to zero) resulting in the appearance of the L$_3$ phase. Finally, a lamellar phase was formed again, due to a third decrease in curvature. For all "salting-in" and divalent anions, only one clear region consisting of oil swollen micelles (O/W nano-emulsion) coexisting with excess oil was observed. With increasing concentration, the micelles get smaller and more oil is displaced in the excess phase. By increasing the temperature, a lamellar phase transition occurs. This is due to a reduction of the micelle curvature, which is an effect of the additional oil in the system.

In addition, it was demonstrated that the stability of the nano-emulsions can be increased with increasing numbers of heating and cooling cycles. The more often the samples are heated and cooled the more stable the solutions appear. Coalescence

or creaming are the main mechanism expected for the instability. Furthermore, the stability of the solutions does not depend on the order of mixing the ingredients.

3.4 Solubilization of High Amounts of Triglycerides in Water Using an Extended Surfactant by the Phase Inversion Temperature

3.4.1 Introduction

In the previous Section 3.3, the effect of salts on the phase behavior and the stability of nano-emulsions was discussed. It has been demonstrated that the stability of the solutions can be increased, depending on the nature of the salt, its concentration, and the number of heating and cooling cycles. The obtained information from the last Section was applied for the preparation of nano-emulsions containing high amounts of rapeseed oil. As already mentioned in the Fundamentals Section 1.1 and 1.3, it is more difficult to solubilize high amounts of vegetable oils into microemulsions than lower molecular weight oils.

It has already been shown that extended surfactants are the most promising candidates to solubilize high amounts of triglycerides or vegetable oils in the continuous aqueous phase of microemulsions, requiring low surfactant concentrations. Due to the unique structure of the extended surfactants, containing hydrophilic and lipophilic linkers, they exhibit the ability to stretch further into the oil and the water phase and enhance the solubility of oil in water.[4–7, 10, 11, 13, 25–27]

In this last Section of the thesis, the preparation and characterization of solutions containing high amounts of rapeseed oil, water, and low concentrations of the chosen extended surfactant X-AES (C_{12-14}-$(PO)_{16}$-$(EO)_2$-SO_4Na, Figure 2.1) will be presented. The oil to water mass ratio was always 1:1 and the oil (or water) to surfactant mass ratio was always kept at 1:0.3. Due to the fact that these components do not form any kind of nano-emulsion without additives, various salts (NaCl, $NaNO_3$, and NaSCN) in different concentrations were added to the solutions and phase diagrams as a function of temperature were recorded.

In addition, the influence of the hydrotrope SXS on the phase behavior was investigated. The initial solutions (without addition of salt) have a mass ratio of 1:1 water to oil, 0.3:1 surfactant to oil (or water), and 0.05:1 hydrotrope to surfactant.

Again, phase diagrams as a function of temperature and added salt concentration were determined. All nano-emulsions were prepared by the phase inversion temperature (PIT) method and the results will be discussed in regards of this method. The structures of the different regions were analyzed using optical microscopy, conductivity measurements, and ^{23}Na/^{2}H-nuclear magnetic resonance (NMR). The phase transition mechanism and the stability of the nano-emulsions will be discussed in detail.

3.4.2 Results

A) Phase Behavior without SXS

a) Phase Diagrams

The phase diagrams of the sodium salt/surfactant/water/rapeseed oil systems as a function of temperature are shown in Figure 3.34.

The different phases occurring for the samples containing NaCl are shown in Figure 3.34a. Turbid solutions are observed for samples below 0.37 mol/kg NaCl at lower temperatures (starting from 0.0 °C), whereas, a very bluish and highly viscous phase is obtained for solutions between 0.20 and 0.37 mol/kg with increasing temperature or between 0.37 and 0.71 mol/kg NaCl at 0.0 °C. All samples between 0.20 and 0.71 mol/kg turn into a birefringent phase at higher temperatures (seen with crossed polarizers), while samples between 0.71 and 1.06 mol/kg appear already birefringent at 0.0 °C. A phase transition arises for all solutions between 0.20 and 1.06 mol/kg NaCl from the anisotropic phase into a bluish (almost clear) and less viscous phase at elevated temperature. This bluish and less viscous phase remains stable until 80.0 °C. The phase transition temperature for the appearance and disappearance of the birefringent phase decreases with increasing salt concentration and is in agreement with previously described results (Section 3.2 and 3.3). In addition, it is important to mention that the birefringent phase is very clear at the boarders (phase transitions, indicated with a dotted line in Figure 3.34a) and almost turbid (very bluish) in the middle of the phase. All samples above 1.06 mol/kg NaCl appear turbid over the whole temperature range.
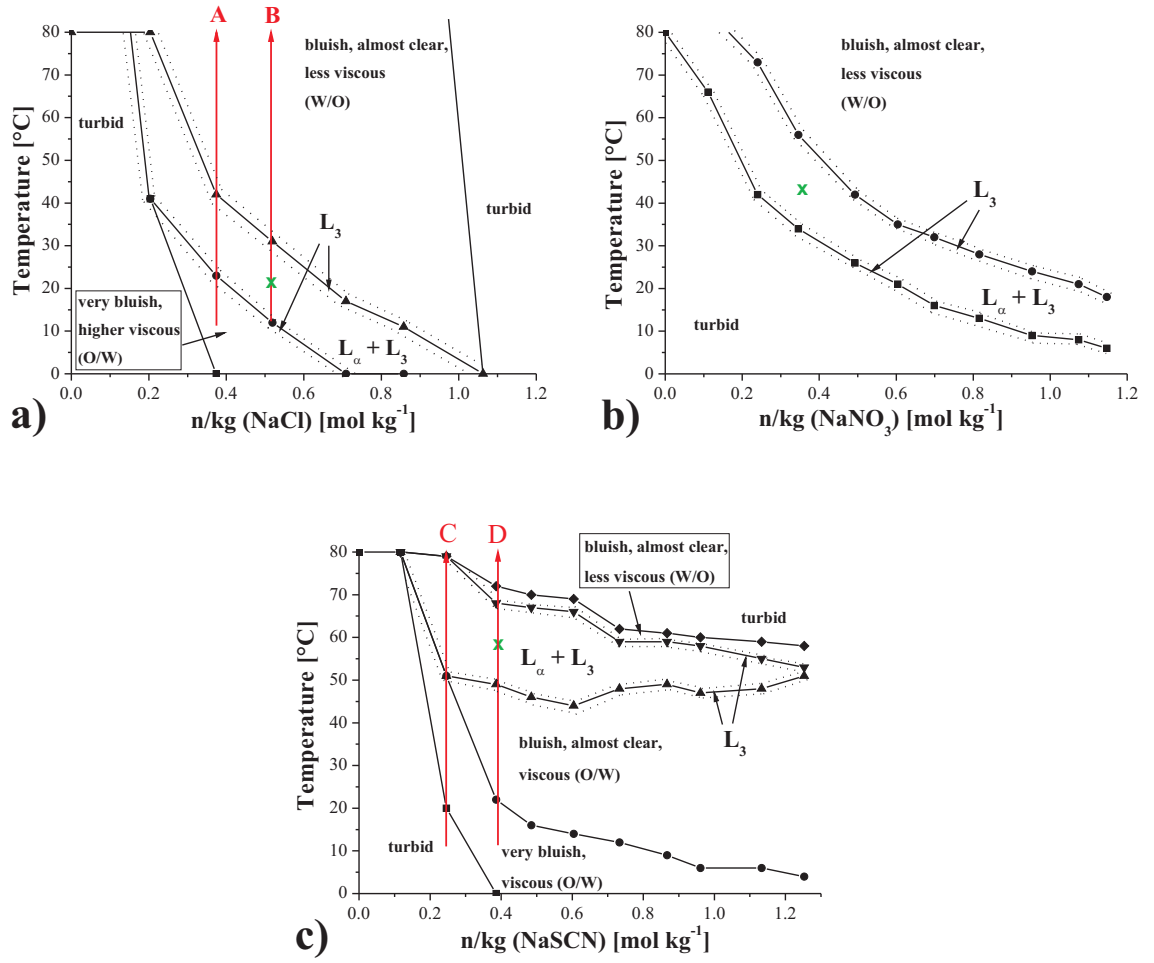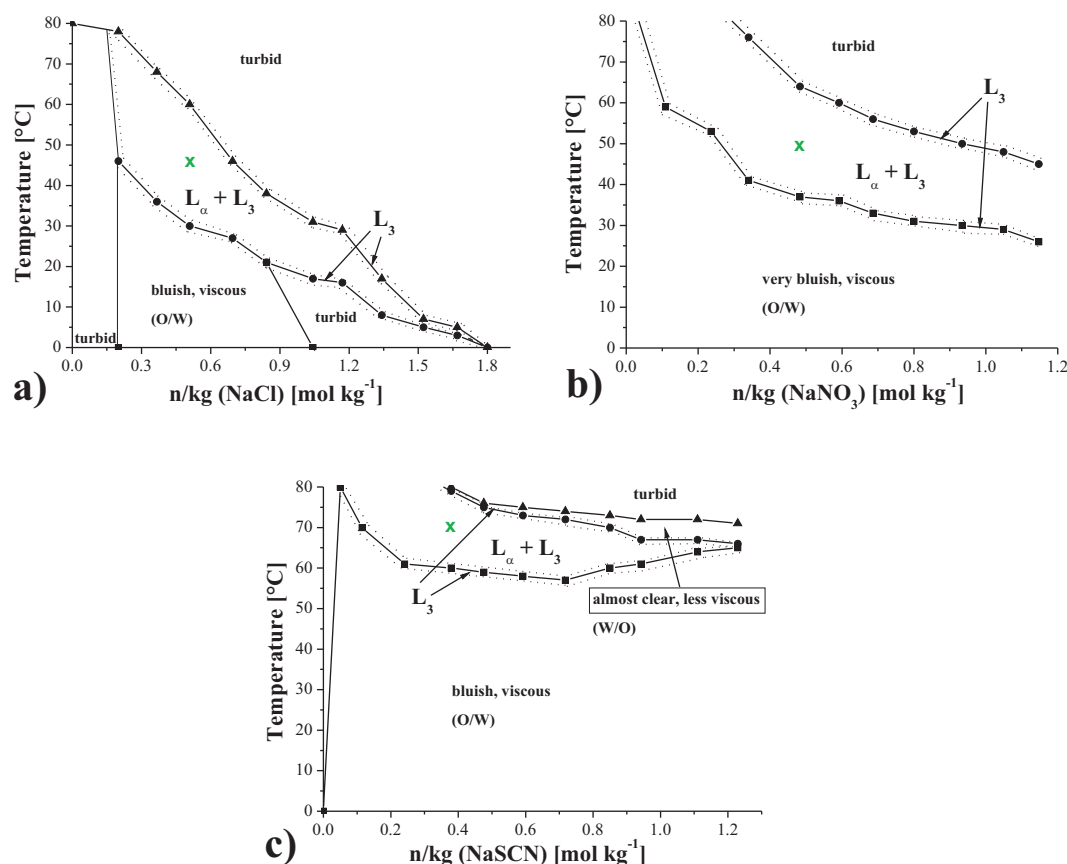
Figure 3.34: Phase diagrams of the sodium salt/surfactant/water/rapeseed oil system as a function of temperature [°C]. The starting formulations, without additional salt consisted of 44.0 wt% water, 43.0 wt% rapeseed oil, and 12.5 wt% X-AES. (a) NaCl, (b) $NaNO_3$, (c) NaSCN. The clear, semi-clear (bluish), liquid crystalline, and turbid regions are shown in the diagram. The red arrows (A-D) give the chosen paths for conductivity measurements. The green x symbolizes the composition and temperature for microscopy images shown in Figure 3.35. The dotted line represents the appearance of the L_3 phase observed from optical microscopy measurements. The phase boundary is not precisely determined.

The temperature versus salt concentration diagram for $NaNO_3$ is shown in Figure 3.34b. A turbid region is observed for all samples up to a concentration of 1.15 mol/kg $NaNO_3$ at low temperatures. This turbid region turns into a birefringent phase, and finally into a bluish (almost clear) and less viscous phase at

elevated temperatures. Again, the phase transition temperatures for both the appearance and disappearance of the anisotropic phase decrease with increasing salt concentration. This is consistent with the results discussed in Section 3.2 and 3.3. In addition, as described for NaCl, the birefringent phase is very clear at the boundaries (indicated with a dotted line in Figure 3.34b) and turbid (very bluish) in the middle of the region.

Figure 3.34c represents the results obtained for the salt NaSCN. The topology of this phase diagram is different from the one observed for NaCl or NaNO$_3$. All samples below 0.12 mol/kg NaSCN remain turbid over the whole temperature range. In addition, samples between 0.12 and 0.25 mol/kg NaSCN are turbid at 0.0 °C. A very bluish and highly viscous phase arises for solutions between 0.12 and 0.39 mol/kg NaSCN with increasing temperature and for samples between 0.39 and 1.25 mol/kg NaSCN already at 0.0 °C. At elevated temperatures, this very bluish phase turns into an almost clear region (less bluish, monophasic) and finally into a birefringent phase. Within the anisotropic phase the samples are clear at the boarders (indicated with a dotted line in Figure 3.34c) and very bluish in the middle of the phase. The temperature for the appearance and disappearance of the anisotropic phase is decreasing at low salt concentrations, as seen for NaCl or NaNO$_3$, and increasing at intermediate/high salt concentration. Again, this effect is expected from the Hofmeister series and was already discussed in the previous Sections 3.2 and 3.3. At high temperatures, the birefringence disappears and clear (less viscous) solutions are obtained for a narrow temperature range, which fade into a turbid phase.

It is important to mention that clear/bluish monophasic solutions are obtained for all systems despite the high rapeseed oil and low surfactant concentrations.

b) Optical Microscopy

Optical microscopy measurements as a function of temperature were performed to obtain more information on the different structures within the turbid, very bluish, bluish, and almost clear regions of the phase diagrams.

In the first (very bluish and highly viscous) area at lower temperatures, small droplets between 1 and 10 μm are observed for all three sodium salts. Depend-
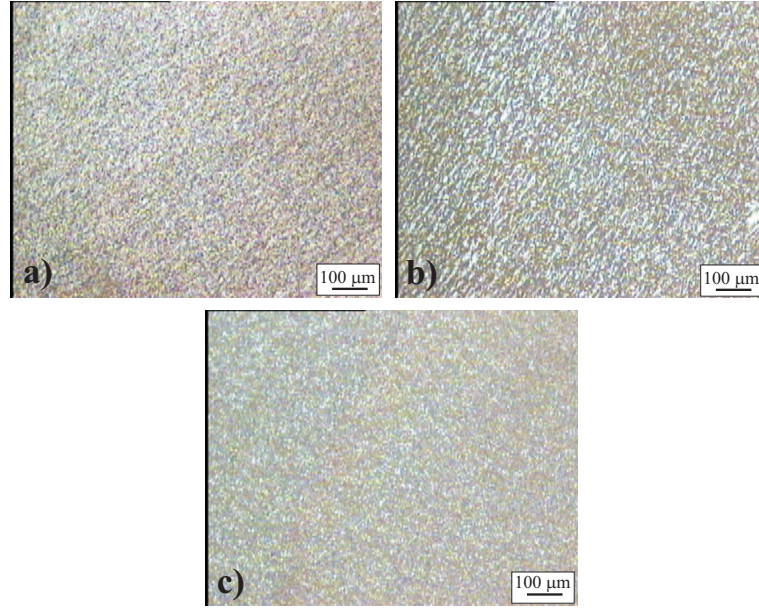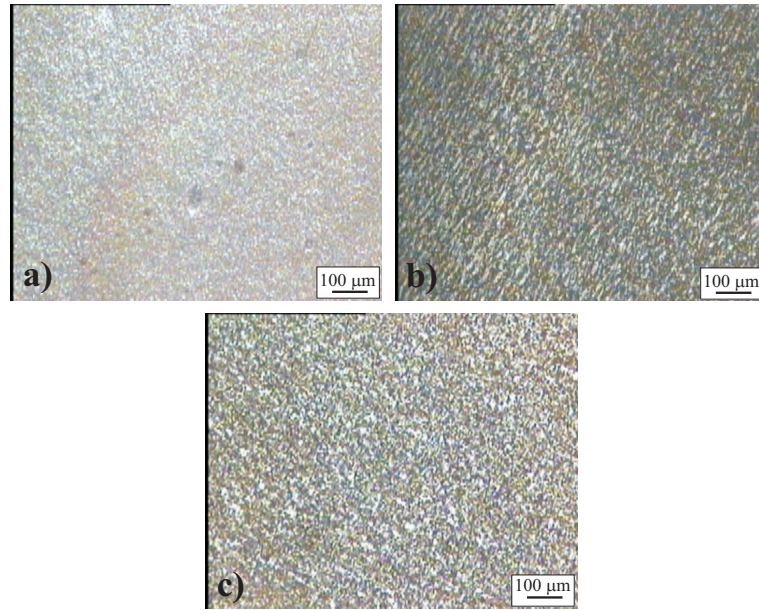
Figure 3.35: Optical microscopy images of a sodium salt/surfactant/water/rapeseed oil mixtures (symbolized with a green x in Figure 3.34). (a) 0.52 mol/kg NaCl solution at 22.0 °C (lamellar phase, L_α); (b) 0.37 mol/kg $NaNO_3$ solution at 43.0 °C (lamellar phase, L_α); (c) 0.39 mol/kg NaSCN solution at 59.0 °C (lamellar phase, L_α).

ing on the concentration and the temperature, more (very bluish samples) or less (almost clear, less bluish samples) droplets can be seen under the microscope. This result is in agreement with an O/W nano-emulsion with excess oil (droplets).

Increasing the temperature, a flashing/sparkling was observed for all samples after slightly pushing the samples. This effect occurs at the lower and upper boundary of the birefringent phase (dotted line in Figure 3.34a-c). This behavior is well-known for an isotropic bicontinuous L_3 phase. Due to the performed shear strain by slightly pushing the sample, an ordered anisotropic state arises for a short moment. This results in the mentioned flash seen under the microscope with crossed polarizers. In the middle of the anisotropic region, a lamellar phase is observed for all three salts, which was clearly identified.[39, 40] Beside the common "oily streaks", "Maltese crosses" were observed within the samples. Images for the three salts at different temperatures are shown in Figure 3.35 and symbolized with a green x in the phase diagram (Figure 3.34a-c). In addition, small droplets between 1 and 10 μm appear again within the second bluish (almost clear) and less viscous region at higher temperature above the birefringent phase (Figure 3.34a-c). This result is consistent with

a W/O nano-emulsion with excess water (droplets).

c) Conductivity
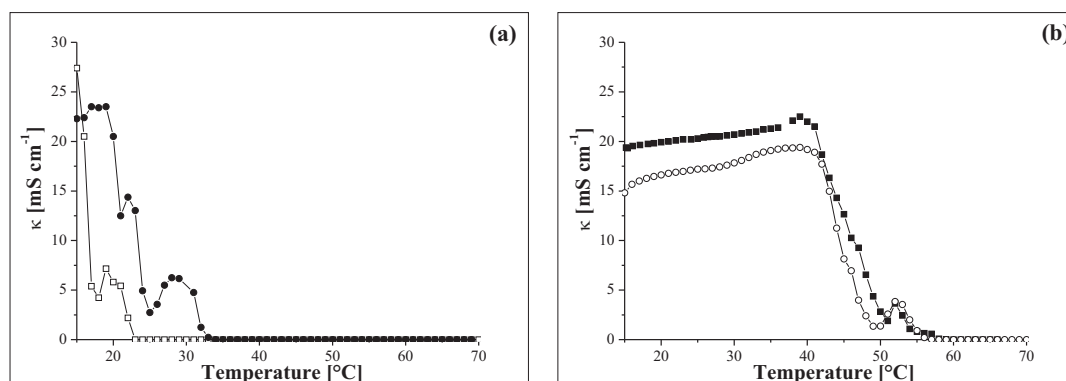
Figure 3.36: Specific conductivity [mS/cm] as a function of temperature [°C]. (a) Comparison of two different NaCl concentrations: (●) 0.37 mol/kg NaCl (path A in Figure 3.34a), (□) 0.52 mol/kg NaCl (path B in Figure 3.34a). (b) Comparison of two different NaSCN concentrations: (○) 0.25 mol/kg NaSCN (path C in Figure 3.34c), (■) 0.39 mol/kg NaSCN (path D in Figure 3.34c).

Temperature dependent conductivity measurements were performed for two different NaCl (path A and B in Figure 3.34a) and NaSCN (path C and D in Figure 3.34c) concentrations and the results are shown in Figure 3.36a and b. The temperature was constantly increased during the measurements starting from 15.0 to 70.0 °C. As expected, the starting conductivity increases with increasing electrolyte concentration for both salts. A small plateau region is observed for 0.37 mol/kg NaCl (● in Figure 3.36a) at 24.0 mS/m. This plateau is concordant with the first very bluish region in the phase diagram and an O/W nano-emulsion (with excess oil) can be expected. As described for the conductivity results of NaCl in the last Section 3.3, the high conductivity arises from the water-rich phase containing the total salt concentration. Increasing the temperature to 20.0 °C the conductivity decreases to 12.5 mS/m, followed by a slight increase at 22.0 °C to 14.4 mS/m. This is in accordance with the lower boundary of the birefringent phase in the phase diagram

(Figure 3.34a) and the flashing observed under the microscope. A L_3 phase is the expected structure. As mentioned in Section 3.3, in a bicontinuous L_3 structure a connected system is present and conductivity is observed. However, due to the fact that charge carriers have a higher probability to move freely in a water continuous than in a bicontinuous phase, the conductivity of the L_3 phase is lower than for the O/W nano-emulsion. Increasing the temperature further, the conductivity decreases again and a minimum (2.7 mS/m) is observed at 26.0 °C, which is consistent with the formation of the L_α phase. Afterwards, the conductivity increases again, until a maximum of 6.3 mS/m is achieved at 30.0 °C. This is due to the formation of a L_3 phase again at the upper boundary of the birefringent phase. At higher temperatures the conductivity decreases to a value of approx. 0 mS/m and no rise was observed anymore. This result is in agreement with the second clear region in the phase diagram (Figure 3.34a). Due to the formation of a W/O nano-emulsion, the complete water phase including the salt is enclosed inside the micelles and therefore, the conductivity is close to 0 mS/m.

The obtained conductivity at 15.0 °C of the 0.52 mol/kg NaCl solution already decreases with a small increase of temperature ($\square$ in Figure 3.36a). This decline is consistent with the lamellar phase, which is already formed at 15.0 °C (see Figure 3.34a). Increasing the temperature further, the conductivity rises slightly followed by a sharp decrease. This is in agreement with the formation of the L_3 phase at the upper boarder of the birefringent phase (Figure 3.34a). At higher temperatures, the conductivity decreases to a value below the detection limit and a W/O nano-emulsion (with excess water) is obtained.

The topology of the conductivity versus temperature curve of the two NaSCN concentrations is very similar. However, the shape also differs from the curve obtained for both NaCl concentrations. The relatively high conductivity at 15.0 °C increases with increasing temperature from 14.9 to 19.4 mS/m for 0.25 mol/kg NaSCN ($\bigcirc$ in Figure 3.36b) and from 19.4 to 22.5 mS/m for 0.39 mol/kg NaSCN ($\blacksquare$ in Figure 3.36a). An O/W nano-emulsion (with excess oil) is expected in this temperature range and is consistent with the clear region in the phase diagram (Figure 3.34c). At higher temperatures, the conductivity decreases until 50.0 °C to

1.4 and 1.9 mS/m for 0.25 and 0.39 mol/kg NaSCN, respectively. This decline is followed by an increase resulting in a maximum at 52.0 °C to 3.8 mS/m for both concentrations. Again, this result is consistent with the formation of a L_3 phase at the lower boundary of the birefringent phase. At elevated temperatures, a lamellar phase is formed, which results in a decline of the conductivity. The second formation of a L_3 phase at the upper boundary was not observed. Difficulties in heating the samples above 70.0 °C appeared due to uncontrolled evaporation of the water phase.

It is important to mention that temperature shifts (3-5.0 °C) can occur between the results obtained for the phase diagrams and from conductivity measurements, which is due to small differences in the preparations of the solutions. Only small changes in concentrations of the various components can drastically change the phase transition temperatures.

d) NMR Measurements

To confirm the lamellar phase (Figure 3.34c and Figure 3.35a), NMR studies of a
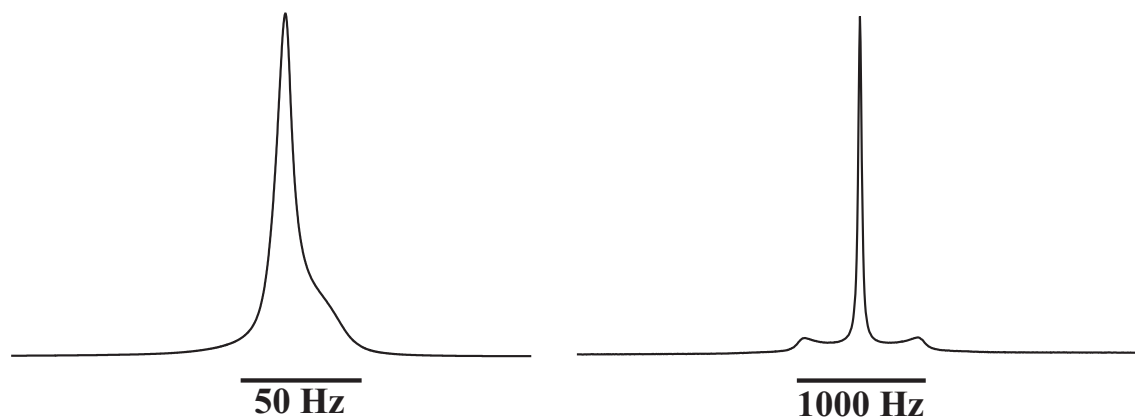
Figure 3.37: (a) Deuterium and (b) Sodium quadrupole splitting of a 0.52 mol/kg NaCl solution at 22.0 °C indicated with a green x in the phase diagram Figure 3.34c.

0.52 mol/kg NaCl solution at 22.0 °C phase were performed using deuterium (^{2}H) and sodium (^{23}Na) resonances. The observed spectra for the ^{2}H- and ^{23}Na-NMR measurements are shown in Figure 3.37a and b.

Only a single, but very broad peak is obtained from the ^{2}H-NMR measurements (see Figure 3.37a). A well resolved quadrupole splitting (doublet) was not observed.

However, an indication of a shoulder can be seen in the spectra. Thus, a mesophase together with an isotropic solution is present. This leads to the assumption that a L_3 phase is coexisting with a lamellar phase, as expected from the described results above. However, the obtained lamellar phase is very disordered, which is consistent with the disordered lamellar phase described for the binary surfactant-water system (Section 3.1). The lamellar phase in this case, should be more disordered due to the high amounts of oil in this solution as well as the coexistence of the L_3 phase. In addition, a well resolved doublet was observed from the ^{23}Na-NMR measurements (see Figure 3.37b). However, the obtained quadrupole splitting is 534.37 Hz and therefore, more than six times smaller than the quadrupole splittings observed in the binary system (Section 3.1). Again, a very disordered lamellar phase together with a L_3 phase is the expected structure.

e) Stability of the Nano-Emulsions

Sample number	Order of mixing
Sample 1	oil + X-AES + water + NaCl
Sample 2	oil + NaCl + X-AES + water
Sample 3	X-AES + water + oil + NaCl
Sample 4	X-AES + water + NaCl + oil
sample 5	NaCl + oil + X-AES + water
Sample 6	NaCl + X-AES + water + oil

Table 3.3: Orders of mixing to verify, if the stability of the nanoemulsions depends thereof.

To obtain information about the stability of the nano-emulsions and if the stability depends on the order of mixing, various samples containing 0.37 mol/kg NaCl in different mixing orders were prepared (Table 3.3). Photographs of the six solutions were taken every day in the first two weeks and afterward, once a week. The solutions were not stirred during the measurements. The results of the stability of the solutions before and after four weeks are shown in Figure 3.38a and b. After the preparation, all the samples (1-6) appeared bluish at room temperature and no difference between the order of mixing was obtained (Figure 3.38a). The samples were still bluish/clear after four weeks and once more, no difference in the mixing
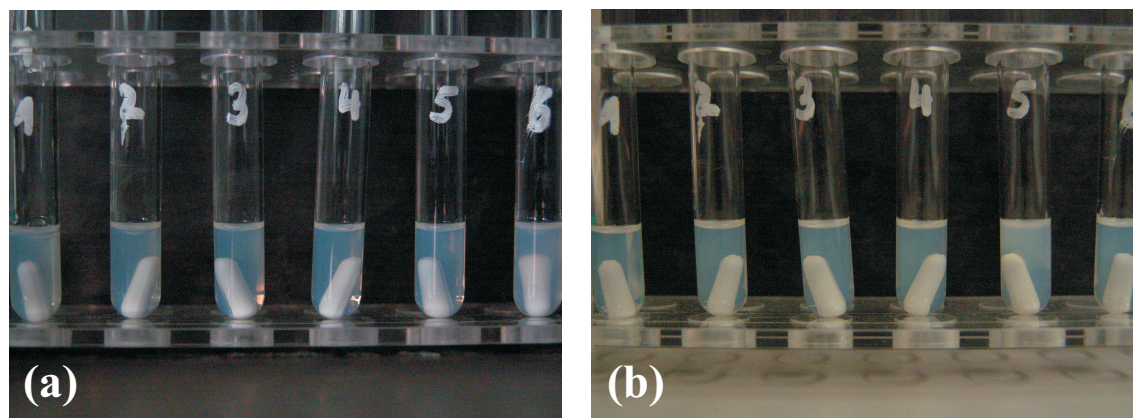
Figure 3.38: Photographs of a nano-emulsion with 0.37 mol/kg NaCl. The numbers 1 to 6 indicate solutions prepared in different orders. a) before and b) after four weeks. The solutions were not stirred during the stability measurements.

order was observed. After five weeks turbid solutions appeared or phase separation occurred. This result demonstrates that the stability of the nano-emulsions does not depend on the order of mixing. In addition, it needs to be mentioned that stable solutions ($\cong$ one months) were obtained despite the high rapeseed oil and the low surfactant content (surfactant to rapeseed oil ratio 0.3:1).

  Additionally, the stability of the solutions depends strongly on the number of heating (up to 80.0 °C) and cooling (down to 0.0 °C) cycles applied to the nano-emulsions during the preparation. As observed for previously described results (Section 3.3), the nano-emulsions are only formed after at least one heating and cooling step. This is in agreement with the phase inversion temperature method (PIT).[86] Additionally, the more often the solutions were heated up (to 80.0 °C) and cooled back down (to 0.0 °C) the more stable the solutions were. As mentioned in the last Section 3.3, the emulsification takes place within the bicontinuous L_3 phase. Nano-emulsions are formed by rapidly cooling the solutions, which leads to an increased hydration of the EO groups and a change in curvature. This results in the formation of small droplets.[78, 189–191] Due to the high amounts of rapeseed oil and the slow kinetics of X-AES, more heating and cooling cycles are necessary to obtain long term stable emulsions.

B) Phase Behavior with SXS

a) Phase Diagrams

Figure 3.39: Phase diagrams of the salt/SXS/surfactant/water/rapeseed oil system as a function of temperature [°C]. The starting formulations, without additional salt consisted of 43.0 wt% water, 42.0 wt% rapeseed oil, 2.0 wt% SXS, and 12.5 wt% X-AES. (a) NaCl, (b) NaNO$_3$, (c) NaSCN. The clear, semi-clear (bluish), liquid crystalline, and turbid regions are shown in the diagram. The green x symbolizes the composition and temperature for microscopy images shown in Figure 3.40. The dotted line represents the appearance of the L$_3$ phase observed from optical microscopy measurements. The phase boundary is not precisely determined.

Phase diagrams of the same sodium salt/surfactant/water/rapeseed oil systems as described before, but with additional 2 wt% SXS, as function of temperature are shown in Figure 3.39. The water to oil mass ratio is always 1:1, 0.3:1 for surfactant to oil (or water), and 0.05:1 for hydrotrope to surfactant. The topology of the phase

diagrams is similar to the one observed for the solutions without SXS.

The phase diagram for the solutions containing various concentrations of NaCl is shown in Figure 3.39a. All the solutions below 0.20 mol/kg NaCl appear turbid over the whole temperature range. In addition, a turbid solution is obtained for samples between 0.84 and 1.80 mol/kg at low temperatures. However, a very bluish and viscous region is observed for intermediate NaCl concentrations between 0.20 and 0.84 mol/kg at 0.0 °C. Increasing the temperature, the very bluish samples at intermediate concentrations or the turbid solutions at high concentrations turn into a birefringent phase. As expected from previous results, the phase transition temperature for the appearance and disappearance of the anisotropic phase decreases with increasing NaCl concentration. Additionally, it is higher than for the solutions without SXS. Also for these solutions, the birefringent phase is very clear at the upper and lower boundary (indicated with a dotted line in Figure 3.39a) and turbid in the middle of the phase. At elevated temperatures, above the birefringent phase, a turbid solution is observed for NaCl concentrations between 0.2 and 1.80 mol/kg. A clear and less viscous phase as found for the solutions without SXS was not obtained in this case.

The temperature versus salt concentration diagram of $NaNO_3$ with SXS is shown in Figure 3.39b. Very bluish, but monophasic solutions occur over the whole concentration range at low temperatures starting from 0.0 °C. This behavior is different in comparison to the samples without SXS, where turbid solutions appeared at low temperatures. At elevated temperatures a birefringent phase occurs, which is broader and appears at higher temperatures than seen for the solutions without SXS. Again, the transition temperatures decrease with increasing salt concentration. Clear solutions are obtained at the boarders of the anisotropic region (indicated with a dotted line in Figure 3.39b, while a turbid solution occurs within the middle of the phase. The birefringent phase extends over 80.0 °C for solutions between 0.11 and 0.34 mol/kg $NaNO_3$, whereas turbid solutions occur for concentrations between 0.34 and 1.15 mol/kg $NaNO_3$, above the birefringent phase.

A bluish and viscous region is observed for NaSCN over the whole concentration range and a large temperature range (starting from 0.0 °C, Figure 3.39c). At el-

evated temperatures, higher than observed for the solutions without SXS, a bire-fringent phase arises. This phase is clear at the boarders (indicated with a dotted line in Figure 3.39c and turbid in the middle of the region. The phase transition temperatures decrease at low salt concentrations and increases at higher concentrations. This is in agreement with previously described results in Section 3.2 and 3.3. Increasing the temperature further, a clear and less viscous phase appears for a very small temperature range, followed by a turbid region.

Again, it is important to mention that monophasic solutions are obtained for all three salts despite the high oil and low surfactant concentration.

b) Optical Microscopy

Figure 3.40: Optical microscopy images of a sodium salt/surfactant/hydrotrope/water/rapeseed oil mixtures (symbolized with a green x in Figure 3.39). (a) 0.51 mol/kg NaCl solution at 46.0 °C (lamellar phase, L_α); (b) 0.48 mol/kg NaNO$_3$ solution at 49.0 °C (lamellar phase, L_α); (c) 0.38 mol/kg NaSCN solution at 70.0 °C (lamellar phase, L_α).

Optical microscopy measurements were performed to obtain the different phases occurring within the phase diagram. As observed for the solutions without SXS, only a few droplets can be seen for all the samples in the first clear region at low temperatures. More and larger droplets are seen for very bluish samples, while less

and smaller droplets were observed for bluish (almost clear) solutions. An O/W
nano-emulsion with excess oil can be expected within this region. At the lower and
upper boundary of the birefringent phase, the same flashing/sparkling was observed
as obtained for the solutions without SXS, which is consistent with the formation of
a L_3 phase (indicated with a dotted line in Figure 3.39. In addition, a lamellar phase
was clearly identified in the middle of the birefringent phase. Images of this phase
for all three salts are shown in Figure 3.40a-c. Increasing the temperature further, a
clear region was observed for NaSCN concentrations from 0.38 to 1.23 mol/kg. Due
to the isotropic structure of this clear region, it appears dark under the microscope
and only a few small droplets can be identified. This is in agreement with a W/O
nano-emulsion with excess water. All NaCl and $NaNO_3$ solutions are turbid at ele-
vated temperatures above the birefringent phase (Figure 3.39a-c) and large droplets
were observed under the microscope.

c) NMR Measurements
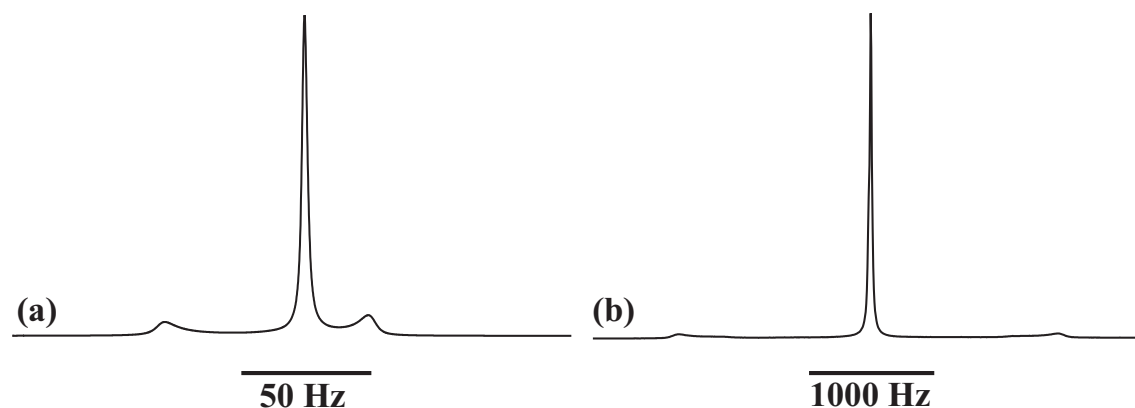
Figure 3.41: (a) Deuterium and (b) Sodium quadrupole splitting of a 0.51 mol/kg NaCl solution
with SXS at 46.0 °C indicated with a green x in the phase diagram Figure 3.34c.

NMR studies of a 0.51 mol/kg NaCl solution including SXS were performed at
46.0 °C using deuterium (^{2}H) and sodium (^{23}Na) resonances. The obtained spectra
are illustrated in Figure 3.41a and b.
A well resolved doublet is observed for the ^{2}H-NMR measurement (see Figure 3.41a).
However, a single peak is obtained as well, indicating the existence of a isotropic

solution within the mesophase. The observed quadrupole splitting is 8.93 Hz and thus, much smaller than the splittings observed for the binary surfactant-water system. A very disordered lamellar phase combined with a L_3 phase is the expected structure.

Similar results were obtained from the ^{23}Na-NMR measurements. A well resolved doublet is observed (see Figure 3.41b). Again, the quadrupole splitting is much smaller than found for the binary surfactant water system (2953.12 Hz). This result leads to the assumption that a lamellar phase coexists with a L_3 phase.

3.4.3   Discussion

Two main phase transitions occur for all three salts with and without the addition of the hydrotrope. The first transition arises from a turbid or very bluish solution to a lamellar phase (coexisting with a L_3 phase) passing through a L_3 phase at low temperatures. A second transition arises at elevated temperatures from the lamellar phase (coexisting with the L_3 phase) passing through a L_3 phase again to a less bluish almost clear and less viscous phase (without SXS), or to a turbid region (with SXS). In addition, a less bluish (almost clear) and less viscous area is observed for NaSCN below and above the birefringent phase, with and without the addition of SXS.

The following phase transition mechanism is expected for the samples with NaCl and NaNO$_3$, with and without the addition of SXS. A positive spontaneous curvature is observed at low temperatures forming oil swollen micelles with an excess oil phase (O/W nano-emulsion). Depending on how much oil is solubilized inside the micelles and how much oil is displace in the excess phase, the solutions remain more or less bluish or turbid. By increasing the temperature, "salting-out" electrolytes (NaCl and NaNO$_3$) decrease the (spontaneous) aggregate curvature (see Section 3.2 and 3.3) and reduce the area per molecule due to electrostatic screening. Therefore, the micelles get flatter and a L_3 phase is observed followed by a lamellar phase (coexisting with a L_3 phase) and a L_3 phase again. A phase inversion occurs at elevated temperatures due to a further decrease of the (spontaneous) micelle curva-

ture. Thus, a W/O nanoemulsions, consisting of water swollen micelles with excess water is formed. Again, depending on the amount of water solubilized inside the reverse micelles and the amount of excess water, the solutions appear more or less bluish or even turbid.

The lamellar phase arises at higher temperatures in solutions with the hydrotrope due to the fact that SXS acts as a "salting-in" additive and therefore, decreases the size of the micelles. As already mentioned in Section 3.2, SXS adsorbs on the surface of the micelles, decreases the size of the micelle, and increases the head-group, the curvature, and the area per molecule of the aggregates. Consequently, smaller micelles are observed being more negatively charged due to the adsorption of SXS on the micelle. More salt is needed to screen the charge and to enhance the lamellar phase formation. Thus, the observed transition curves are flatter and occur at higher temperatures. Currently, small angle X-ray scattering measurements are performed for solutions with and without SXS, to confirm the lamellar phase and to obtain more details about the structure of the aggregates.

A similar phase transition mechanism appears for NaSCN. At low temperatures an oil swollen micellar solution occurs with excess oil (O/W nano-emulsion). Increasing the temperature, a birefringent phase arises, as described for the other two salts. At low salt concentrations, the same phase transition mechanism holds due to electrostatic screening. This results in a decrease of the phase transition temperature; similar results were obtained in Section 3.2. However, at intermediate/high salt concentrations the transition temperatures increase again. This is due to the fact that "salting-in" ions, like NaSCN, have a higher association with non-polar surfaces and thus, with the micelles. The size of the micelles decreases (with increasing temperature) together with an increasing head-group area and an increased (spontaneous) micelle curvature. Therefore, smaller micelles with a larger head-group are obtained. This effect does not only explain the higher transition temperatures for the formation of the lamellar phase, but also the formation of a less bluish and less viscous phase below and above the birefringent phase. The smaller the micelles, the clearer the solutions appear. However, in contrast to the effect of NaSCN described in the last two sections (3.2 and 3.3), a lamellar phase (coexisting with a

L_3 phase) occurs passing trough a single L_3 phase at the boarders. As described for the NaSCN solutions in the last Section 3.3, a reduction in aggregate curvature occurs with increasing temperature. It arises from the increased repulsion between the hydrophobic groups with increasing temperature. This effect is increased due to the high amounts of the oil present in the system. Again, the phase transition temperatures appear at higher temperatures for solutions with SXS. The same explanation holds as described above for the solutions with NaCl and NaSCN.

The phase behavior for all three salts with increasing temperature is similar to results from the literature. Izquierdo *et al.* studied the phase behavior of nano-emulsions using the PIT method. A phase transition mechanism was decribed from oil-swollen micelles (O/W nano-emulsion) with an excess oil phase (positive spontaneous curvature), passing through a bicontinuous L_3 phase (spontaneous curvature almost zero), a lamellar phase (coexisting with a bicontinuous L_3 phase), a L_3 phase again, resulting in water swollen micelles (W/O nano-emulsion, negative spontaneous curvature) with increasing temperature.[87, 192]

In addition, it was demonstrated that the nano-emulsions were only formed after heating the samples above the phase inversion temperature and rapidly cooling down again (PIT method, [86]). The stability of the solutions depends strongly on the number of heating and cooling cycles. The more often the samples were heated and cooled the more stable the solutions appeared. As previously described, nano-emulsion formation occurs within the bicontinuous L_3 phase. For stable solutions, all the oil must be solubilized within this phase. However, due to the slow kinetics of the used extended surfactants and the high amounts of rapeseed oil in the system, more heating and cooling cycles are necessary to achieve long term stable emulsions. Ostwald ripening or coalescence are the main mechanism for the instability of the nano-emulsions (already described in Section 1.4 and 3.3).[78, 80, 189–191]

Additionally, it was shown by Solans *et al.* that the droplet size of the nanoemulsions and the polydispersions index increases with an increasing oil concentration or a decreasing surfactant concentration.[78] Therefore, bluish rather than clear solutions are obtained with these systems due to the high amounts of rapeseed oil and low surfactant concentrations.

However, it is important to mention that monophasic solutions are obtained for all three salts despite the high oil and low surfactant concentration.

3.4.4 Concluding Remarks

The effect of three anions (NaCl, NaNO$_3$ and NaSCN) on the formation of nano-emulsions containing high amounts of triglycerides and low concentrations of surfactant was investigated. A strong influence of the ions on the formation, the phase behavior, and the stability of the nano-emulsions was observed. Depending on the salt, a decrease (for NaCl and NaNO$_3$) or an increase (for Na$_2$SO$_4$, NaSCN) of the phase transition temperatures arises. An O/W nano-emulsion with excess oil was obtained at low temperatures. In addition, depending on the amount of displaced oil in the bulk, bluish or turbid solutions were observed. Increasing the temperature, a lamellar phase coexisting with a L$_3$ phase was formed. At the lower and upper boundary of the lamellar phase, a single L$_3$ phase occurred. Finally, a W/O nano-emulsion with excess water was observed at high temperatures temperature. Depending on the amount of displaced water within the excess phase, bluish or turbid solutions were observed.

In addition, it was demonstrated that the stability of the nano-emulsions can be increased with increasing numbers of heating and cooling cycles. The more often the samples are heated and cooled the more stable the solutions appear. Coalescence or creaming are the main mechanism for the instability. The stability of the solutions does not depend on the order of mixing the ingredients. In addition, due to the high amounts of rapeseed oil and the low concentrations of surfactant, bluish rather than clear solutions were observed. However, it was demonstrated that X-AES is an excellent surfactant for the formation of nano-emulsions with high amounts of rapeseed oil.

Summary

In this thesis, the extended surfactant X-AES (C_{12-14}-$(PO)_{16}$-$(EO)_2$-SO_4Na) was used for the formation of nano-emulsions, including a high content of vegetable oil. First, the binary surfactant-water system was characterized over the whole concentration range. The following six different phases were observed: a micellar (L_1), a hexagonal (H_1), a lamellar (L_α), a bicontinuous cubic (V_2), a reverse hexagonal (H_2), and an isotropic liquid phase (L_2) containing solid particles (S). The structure of the normal and reverse micelles was determined using various techniques, which gave consistent results. A size range between 5 and 10 nm is obtained for the normal micelles and between 0.6 and 1.5 nm for the reverse micelles. This is notably smaller than the size of the normal micelles. In addition, an attempt was made to determine the CMC of X-AES by surface tension measurement. The obtained experimental CMC was too high in comparison to the calculated values. It was concluded that the determination of the CMC by surface tension measurements must be handled with caution and should always be supported by Langmuir trough measurements. Additionally, the structure and origin of the solid particles were identified. It could be shown that these particles can be easily removed from the surfactant by washing the dried X-AES with acetone.

Four liquid crystal phases are formed in the X-AES-water system. A phase transition from a micellar phase to a hexagonal phase appeared at low temperatures by increasing the concentration. Furthermore, it was demonstrated that the hexagonal phase consists of rod-like micelles, which are more disordered than in conventional surfactants. In addition, a L_1 phase is always present within the H_1 phase. A second phase transition was found by increasing the temperature above the cloud point of the surfactant. In this case, a transition from micelles to a lamellar phase appeared.

Also, for the L_α phase a L_1 phase is always present at lower surfactant concentrations. The lamellar phase appears over a large concentration and temperature range. Again, a disordered state can be found proving that the hydrophobic tails are linked into each other and highly folded. The relatively high area per molecule leads to the inference that there must be a strong influence of the alkyl chains on the negative curvature of the micelles. In addition, the bicontinuous cubic phase and its cell parameters were identified. The unusual space group $I4_132$ was found to be the most likely symmetry of the bicontinuous cubic phase. The reverse hexagonal phase and its aggregate parameters were also determined. A comparison between the extended surfactant and common anionic surfactant SDS, LAS, and SLES was made and concluded that the hydrophilic/lipophilic linkers have a strong influence on the phase behavior of the extended surfactant.

Secondly, the effect of various salts on the cloud point of an aqueous solution of X-AES and X-AES/SXS (mole ratio R = 0.5) was investigated. In a solution without SXS, all anions behave as expected from the Hofmeister series ($Na_2SO_4 = Na_2CO_3 > Na_2HPO_4 > NaOAc > NaBu > NaCl > NaBr > NaNO_3 > NaSCN > SXS > NaOc$). A transition from a micellar solution (L_1) to a lamellar phase (L_α) was observed for all "salting-out" salts and NaOc. This effect can be explained as an intra-micellar interaction. Due to a change in micelle curvature the disc-like micelles grow larger and stick together to a lamellar phase. A second transition from a micellar solution (L_1) to a solution with large droplets (L_1') appeared for all "salting-in" electrolytes. These ions adsorb on the micelle and thus, decrease the size of the micelle, which results in an increased cloud temperature. The addition of anions to an aqueous solution of X-AES/SXS exhibited a drastic change in the order of the anions. All divalent "salting-out" anions change their behavior towards a "salting-in" salt (NaOAc > NaBu > NaCl > NaBr > $NaNO_3 > Na_2SO_4 = Na_2CO_3 = Na_2HPO_4 > NaSCN > NaOc$). It seems that all divalent ions tend to salt out the remaining SXS ions in the aqueous solution and hence, push these molecules inside the micelles. The resulting effect is then similar to the effect of "salting-in" ions. The influence of cations on the solubility of X-AES also follows the Hofmeister series (KCl > CsCl > NaCl > choline chloride > LiCl). All added cations were "salting-out". However, in

solution with SXS, the effect is not as pronounced as for anions. All salts increase the slope of the cloud temperature curve, except choline chloride (choline chloride > KCl > CsCl > NaCl > LiCl).

In addition, the effect of various anions and cations on the formation of nano-emulsions with triglycerides was also investigated. A strong influence of the ions on the formation, the phase behavior, and the stability of the nano-emulsions was observed. Depending on the salt, a decrease (for NaOAc, NaCl, NaNO$_3$, CsCl, KCl, and choline chloride) or an increase (for Na$_2$SO$_4$, NaSCN) of the cloud temperature arises, which is similar to the effect observed for solutions without rapeseed oil. Two clear regions were obtained for all salts, which decrease the cloud temperatures. An O/W nano-emulsion with excess oil was expected at lower temperatures, which turns into a lamellar phase, into a L$_3$ phase, and finally into a lamellar phase again with increasing temperature. Due to a change in micelle curvature, the micelles grow larger and stick together forming a lamellar phase. At higher temperatures, the curvature decreases more (spontaneous curvature equal to zero) resulting in the appearance of the L$_3$ phase. Finally, a lamellar phase was formed again, due to a third decrease in curvature. For all "salting-in" and divalent anions, only one clear region consisting of oil swollen micelles (O/W nano-emulsion) coexisting with excess oil was observed. With increasing concentration, the micelles get smaller and more oil is displaced in the excess phase. By increasing the temperature, a lamellar phase transition occurs. This is due to a reduction of the micelle curvature, which is an effect of the additional oil in the system.

In the end, nano-emulsions with a high content of triglyceride and small amounts of surfactant were prepared and studied in detail. Therefore, the effect of three anions (NaCl, NaNO$_3$ and NaSCN) on the formation of nano-emulsions containing high amounts of triglycerides and low concentrations of surfactant was investigated. Depending on the salt, a decrease (for NaCl and NaNO$_3$) or an increase (for Na$_2$SO$_4$, NaSCN) of the phase transition temperatures arises, as seen for the low oil content systems. An O/W nano-emulsion with excess oil was obtained at low temperatures. Depending on the amount of displaced oil in the bulk, bluish or turbid solutions were observed. Increasing the temperature, a lamellar phase coexisting with a L$_3$

phase was formed. At the lower and upper boundary of the lamellar phase, a single L_3 phase occurred. Finally, a W/O nano-emulsion with excess water was observed at high temperatures temperature. Once more, depending on the amount of excess water, bluish or turbid solutions were observed.

It was demonstrated that the stability of all (low and high oil content) nano-emulsions at room temperature can be increased with increasing numbers of heating and cooling cycles. Coalescence or Ostwald ripening are the possible mechanism for the instability. The stability of the solutions does not depend on the order of mixing the ingredients. In addition, due to the high amounts of rapeseed oil and the low concentrations of surfactant, bluish rather than clear solutions were observed. However, it was demonstrated that X-AES is an excellent surfactant for the formation of nano-emulsions with high amounts of rapeseed oil.

The primary objective for this thesis was achieved. A formulation with a desired surfactant to oil ratio of 1:2 was found. Moreover, the ratio can be increased up to 1:3 surfactant to oil.

To conclude, the chosen extended surfactant was an excellent candidate to solubilize high amounts of triglycerides in water using small concentrations of active. In the future, it would be of interest to perform experiments with its analogue containing a carboxylate head-group instead of a sulfate. It was already shown by Arpornpong *et al.* that ethoxy carboxylate extended surfactants are more promising than the sulfate extended surfactants.[193] In addition, it is known that these kind of surfactants are retained in the environment due to the low biodegradability. Therefore, an extended surfactant containing green and sustainable lipophilic and hydrophilic linkers could be investigated. The extended surfactant was shown to exhibit properties, which could be of great interest for many applications. Especially on the field of solubilization, the surfactant has proven to be an excellent candidate. In the industrial field, it could be used for oil recovery, household products, cleaning supplies, or washing detergency.

Appendix
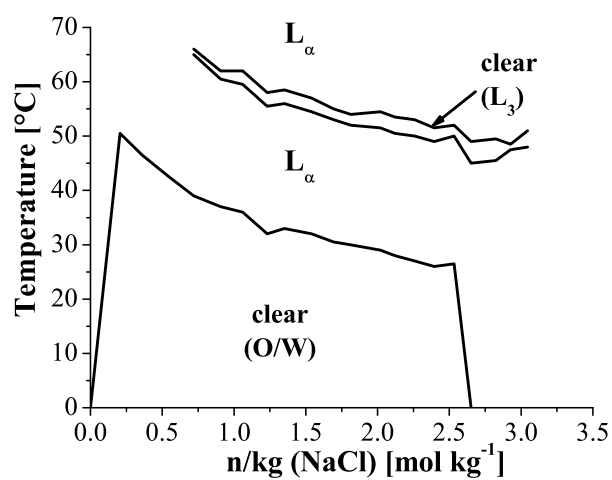
Figure 3.42: Phase diagrams of the NaCl/surfactant/SXS/water/olive oil system as a function of temperature [°C]. The starting formulations, without additional salt, consisted of 62.5 wt% water, 18.0 wt% X-AES, 5.5 wt% SXS, 14.0 wt% olive oil. The clear, semi-clear (bluish), liquid crystalline, and turbid regions are shown in the diagram.
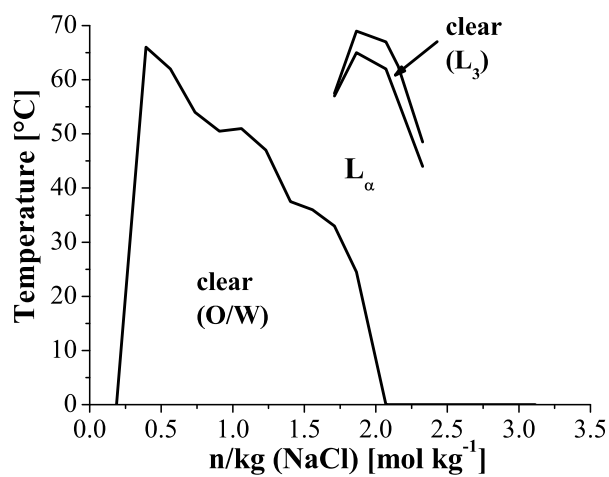
Figure 3.43: Phase diagrams of the NaCl/surfactant/SCS/water/rapeseed oil system as a function of temperature [°C]. The starting formulations, without additional salt, consisted of 62.5 wt% water, 18.0 wt% X-AES, 5.5 wt% SCS, 14.0 wt% rapessed oil. The clear, semi-clear (bluish), liquid crystalline, and turbid regions are shown in the diagram.

List of Figures

List of Tables

List of Publications

Published:

1-N. Vlachy, A.F. Arteaga, A. Klaus, D. Touraud, M. Drechsler and W. Kunz, Influence of Additives and Cation Chain Length on the Kinetic Stability of Supersaturated Catanionic Systems, *Colloids Surf. A* **2009**, 338, 135-141.

2-A. Klaus, G. J. T. Tiddy, D. Touraud, A. Schramm, G. Sthler, M. Drechsler, W. Kunz, Phase Behavior of an Extended Surfactant in Water and a Detailed Characterization of the Dilute and Semi-Dilute Phases, *Langmuir* **2010**, 26, 5435-5443.

3-A. Klaus, G. J. T. Tiddy, D. Touraud, A. Schramm, G. Sthler, W. Kunz, Phase Behavior of an Extended Surfactant in Water and a Detailed Characterization of the Concentrated Phases, *Langmuir* **2010**, 26, 16871-16883.

Submitted:

4-A. Klaus, C. Fajolles, M. Bauer, J.-M. Mallet, J. Daillant, Amphiphilic Behavior and Membrane Solubility of a Dicholesteryl Cyclodextrine, *Langmuir* **2010**.

5-A. Klaus, G. J. T. Tiddy, R. Rachel, A. P. Trinh, E. Maurer, D. Touraud, W. Kunz, Hydrotrope Induced Inversion of Salt Effects on the Cloud Point of an Extended Surfactant, *Langmuir* **2010**.

In preparation:

6-A. Klaus, G. J. T. Tiddy, C. Solans, R. Rachel, D. Touraud, W. Kunz, Effect of salts on the phase behavior and the stability of nano-emulsions with rapeseed oil

and an extended surfactant.

7-A. Klaus, G. J. T. Tiddy, I. Grillo, M. Tomsic, H. Garcia, A. Harrar, E. Maurer, D. Touraud, W. Kunz, Solubility of High Amounts of Triglycerides in Water Using an Extended Surfactant.

8-A. Harrar, O. Zech, A. Klaus, P. Bauduin, W. Kunz, Influence of Surfactant Hydrophobicity on the Phase Behavior of Non-Aqueous Microemulsions.

9-E. Maurer, A. Klaus, W. Kunz, Lidocain Carboxylates - A New Class of Pharmaceutically Active, Surfactant-Like Ionic Liquids.

Bibliography

[1] Winsor, P. A. *Transactions of the Faraday Society* **1948**, *44*, 376–398.

[2] Blakeway, J. M. *Eur. Pat. Appl.* **1988**, *CODEN: EPXXDW EP 261351 A2*.

[3] Graciaa, A.; Lachaise, J.; Cucuphat, C.; Bourrel, M.; Salager, J. L. *Langmuir* **1993**, *9*, 669–672.

[4] Salager, J. L.; Antón, R. E.; Sabatini, D. A.; Harwell, J. H.; Acosta, E. J.; Tolosa, L. I. *J. Surfactants Deterg.* **2005**, *8*, 3–21.

[5] Graciaa, A.; Lachaise, J.; Cucuphat, C.; Bourrel, M.; L., S. J. *Langmuir* **1993**, *9*, 3371–3374.

[6] Uchiyama, H.; Acosta, E.; Tran, S.; Sabatini, D. A.; Harwell, J. H. *Ind. Eng. Chem. Res.* **2000**, *39*, 2704–2708.

[7] Acosta, E.; Uchiyama, H.; Sabatini, D. A.; Harwell, J. H. *J. Surfact. Deterg.* **2002**, *5*, 151–157.

[8] Acosta, E.; Tran, S.; Uchiyama, H.; Sabatini, D. A.; Harwell, J. H. *Environ. Sci. Technol.* **2002**, *36*, 4618–4624.

[9] Acosta, E.; Harwell, J. H.; Sabatini, D. A. *J. Colloid Interface Sci.* **2004**, *274*, 652–664.

[10] Miñana Perez, M.; Graciaa, A.; Lachaise, J.; Salager, J. L. *Colloid Surf., A* **1995**, *100*, 217–224.

[11] Do, L. D.; Witthayapanyanon, A.; Harwell, J. H.; Sabatini, D. A. *J. Surfactants Deterg.* **2009**, *12*, 91–99.

[12] Tanthakit, P.; Ratchatawetchakul, P.; Chavadej, S.; Scamehorn, J. F.; Sabatini, D. A.; Tongcumpou, C. *J. Surfactants Deterg.* **2010**, *13*, 485–495.

[13] Phan, T. T.; Witthayapanyanon, A.; Harwell, J. H.; Sabatini, D. A. *J. Surfactants Deterg.* **2010**, *13*, 313–319.

[14] Holmberg, K., Jönsson, B., Kronberg, B., Lindman, B., Eds. *Surfactants and Polymers in Aqueous Solution 2nd edition*; John Wiley & Sons Ltd, Chichester, 2003.

[15] Rosen, M. J., Ed. *Surfactants and Interfacial Phenomena*; John Wiley & Sons Inc., New Jersey, 2004.

[16] Evans, D. F., Wennerström, H., Eds. *The Colloidal Domain, 2nd edition*; Wiley-VCH, Weinheim, 1999.

[17] Holmberg, K., Ed. *Handbook of Applied Surfaces and Colloid Chemistry, Volume 1-2*; John Whiley & Sons Ltd., Chichester, 2002.

[18] Kjellander, R. *J. Chem. Soc., Faraday Trans. 2* **1982**, *78*, 2025–2042.

[19] Wärnheim, T.; Bokström, J.; Williams, Y. *Colloid Polym. Sci.* **1988**, *266*, 562–565.

[20] Goel, S. K. *J. Colloid Interface Sci.* **1999**, *212*, 604–606.

[21] Koshy, L.; Saiyad, A. H.; Rakshit, A. K. *Colloid Polym. Sci.* **1996**, *274*, 582–587.

[22] Yu, Z.-J.; Xu, G. *J. Phys. Chem.* **1989**, *93*, 7441–7445.

[23] Warr, G. G.; Zemb, T. N.; Drifford, M. *J. Phys. Chem* **1990**, *94*, 3086–3092.

[24] Buckingham, S. A.; Garvey, C. J.; Warr, G. G. *J. Phys. Chem.* **1993**, *97*, 10236–10244.

[25] Witthayapanyanon, A.; Acosta, E. J.; Harwell, J. H.; Sabatini, D. A. *J. Surfactants Deterg.* **2006**, *9*, 331–339.

[26] Witthayapanyanon, A.; Harwell, J. H.; Sabatini, D. A. *J. Colloid Interface Sci.* **2008**, *325*, 259–266.

[27] Witthayapanyanon, A.; Phan, T. T.; Heitmann, T. C.; Harwell, J. H.; Sabatini, D. A. *J. Surfactants Deterg.* **2010**, *13*, 127–134.

[28] Miñana Perez, M.; Graciaa, A.; Lachaise, J.; Salager, J. L. *Progress Colloid Polymer Science* **1995**, *98*, 177–179.

[29] Forgiarini, A. M.; Scorzza, C.; Velásquez, J.; Vejar, F.; Zambrano, E.; Salager, J. L. *J. Surfactants Deterg.* **2010**, *13*, 451–458.

[30] Velásquez, J.; Scorzza, C.; Vejar, F.; Forgiarini, A. M.; Antón, R. E.; Salager, J. L. *J. Surfactants Deterg.* **2010**, *13*, 69–73.

[31] Salager, J. L.; Morgan, J. C.; Schechter, R. S.; Wade, W. H.; Vasquez, E. *Soc. Petrol. Eng. J.* **1979**, *19*, 107–115.

[32] Salager, J. L.; Bourrel, M.; Schechter, R. S.; Wade, W. H. *Soc. Petrol. Eng. J.* **1979**, *19*, 271–278.

[33] Phan, T. T.; Harwell, J. H.; Sabatini, D. A. *J. Surfactants Deterg.* **2010**, *13*, 189–194.

[34] Maibaum, L.; Dinner, A. R.; Chandler, D. *J. Phys. Chem.* **2004**, *108*, 6778–6781.

[35] Kronberg, B.; Costas, M.; Silveston, R. *Pure & Appl. Chem.* **1995**, *67*, 897–902.

[36] Kronberg, B.; Costas, M.; Silveston, R. *J. Dispersion Sci. Technol.* **1994**, *15*, 333–351.

[37] Isrealachvili, J. N.; Mitchell, D. J.; Ninham, B. W. *J. Chem. Soc., Faraday Trans. 2* **1976**, *72*, 1525–1568.

[38] Isrealachvili, J. N.; Mitchell, D. J.; Ninham, B. W. *Biochim. Biophys. Acta* **1977**, *470*, 185–201.

[39] Rosevear, F. B. *J. Am. Oil Chem. Soc.* **1954**, *31*, 628–639.

[40] Rosevear, F. B. *J. Soc. Cosmet. Chem.* **1968**, *19*, 581–594.

[41] Luzzati, V.; Reiss-Husson, F.; Rivas, E.; Krzywicki, T. G. *Ann. NY Acad. Sci.* **1966**, *137*, 409–413.

[42] Luzzati, V.; Reiss-Husson, F. *J. Cell Biol.* **1962**, *12*, 207–219.

[43] Luzatti, V.; Spegt, P. A. *Nature* **1967**, *215*, 701–704.

[44] Luzzati, V.; Tardieu, A.; Krzywicki, T. G.; Rivas, E.; Reiss-Husson, F. *Nature* **1968**, *220*, 485–488.

[45] Fontell, K. *Colloid Polym. Sci.* **1990**, *268*, 264–285.

[46] Saludjian, P.; Reiss-Husson, F. *Proc. Natl. Acad. Sci.* **1980**, *77*, 6991–6995.

[47] Sakya, P.; Seddon, J. M.; Templer, R. H.; Mirkin, R. J.; Tiddy, G. J. T. *Langmuir* **1997**, *13*, 3706–3714.

[48] Burns, R. L. *J. Surfactants Deterg.* **1999**, *2*, 13–16.

[49] Varade, D.; Bahadur, P. *J. Surfactants Deterg.* **2004**, *7*, 257–259.

[50] Neuberg, C. *J. Chem. Soc., Abstracts* **1916**, *110*, 555.

[51] Roy, B. K.; Moulik, S. P. *Curr. Sci.* **2003**, *85*, 1148–1155.

[52] Balasubramanian, D.; Srinivas, V.; Gaikar, V. G.; Sharma, M. M. *J. Phys. Chem.* **1989**, *93*, 3865–3870.

[53] da Silva, R. C.; Spitzer, M.; da Silva, L. H. M.; Loh, W. *Thermochim. Acta* **1999**, *328*, 161–167.

[54] Durand, M.; Zhu, Y.; Molinier, V.; Féron, T.; Aubry, J.-M. *J. Surfactants Deterg.* **2009**, *12*, 371–378.

[55] Myers, D., Ed. *Surfactants and Science Technology, 3rd edition*; John Wiley & Sons Inc., New Jersey, 2006.

[56] Akoh, C. C., Min, D. B., Eds. *Food Lipids: Chemistry, Nutrition, and Biotechnology, 2nd edition*; Marcel Dekker Inc., New York, 2002.

[57] Aparicio, R.; Aparicio-Ruiz, R. *J. Chromatogr. A* **2000**, *881*, 93–104.

[58] Hamilton, R. J. *Pestic. Sci.* **1993**, *37*, 141–146.

[59] Evans, C. D.; McConnell, d. G.; List, G. R.; Scholfield, C. R. *J. Am. Oil Chem. Soc.* **1969**, *46*, 421–424.

[60] Kamal-Eldin, A.; Andersson, R. *J. Am. Oil Chem. Soc.* **1997**, *74*, 375–380.

[61] Xenakis, A.; Papadimitriou, V.; Sotiroudis, T. G. *Curr. Opin. Colloid Interface Sci.* **2010**, *15*, 55–60.

[62] Yamasaki, R.; Ichihara, K. *Bull. Chem. Soc. Jpn.* **1936**, *11*, 114–117.

[63] Yunusov, O. K.; Kadirov, Y. *Chem. Nat. Compd.* **1999**, *35*, 98.

[64] Alander, J.; Wärnheim, T. *J. Am. Oil Chem. Soc.* **1989**, *66*, 1656–1660.

[65] Alander, J.; Wärnheim, T. *J. Am. Oil Chem. Soc.* **1989**, *66*, 1661–1665.

[66] Joubran, R. F.; Cornell, D. G.; Parris, N. *Colloid Surf., A* **1993**, *80*, 153–160.

[67] Raman, I. A.; Suhaimi, H.; Tiddy, G. J. T. *Adv. Colloid Interface Sci.* **2003**, *106*, 109–127.

[68] Raman, I. A.; Suhaimi, H.; Tiddy, G. J. T. *J. Oil Palm Research* **2003**, *15*, 60–62.

[69] N, K.; Sanders, M. D.; Szekeres, E.; Scostas, E. J.; Faller, J. F.; Mentlik, T.; Fisher, L. B.; Nicoll, G.; Sabatini, D. A.; Scamehorn, J. F. *J. Cosmet. Sci.* **2006**, *55*, 309–325.

[70] Friberg, S.; Rydhag, L. *J. Am. Oil Chem. Soc.* **1971**, *48*, 113–115.

[71] Schramm, L. L., Ed. *Emulsions, Foams, and Suspensions*; Wiley-VCH, Weinheim, 2005.

[72] Petesev, D., Ed. *Emulsions: Structure, Stability and Interactions*; Elsevier, London, 2004.

[73] Fingas, M.; Fieldhouse, B. *J. Hazard. Mater.* **2004**, *107*, 37–50.

[74] Ozawa, K.; Solans, C.; Kunieda, H. *J. Colloid Interface Sci.* **1997**, *188*, 275–281.

[75] Morais, J. M.; Rocha-Filho, P. A.; Burgess, D. J. *Langmuir* **2009**, *25*, 7954–7961.

[76] Schmidts, T.; Dobler, D.; Nissing, C.; Runkel, F. *J. Colloid Interface Sci.* **2009**, *338*, 184–192.

[77] Schmidts, T.; Dobler, D.; Guldan, A.-C.; Paulus, N.; Runkel, F. *Colloid Surf., A* **2010**, *372*, 48–54.

[78] Solans, C.; Izquierdo, P.; Nolla, J.; Azemar, N.; Garcia-Celma, M. J. *Curr. Opin. Colloid Interface Sci.* **2005**, *10*, 102–110.

[79] El-Aasser, M. S.; Sudol, E. D. *J. Coat. Technol. Res.* **2004**, *1*, 20–31.

[80] Tadros, T.; Izquierdo, P.; Esquena, J.; Solans, C. *Adv. Colloid Interface Sci.* **2004**, *108–109*, 303–318.

[81] Antonietti, M.; Landfester, K. *Prog. Polym. Sci.* **2002**, *27*, 689–757.

[82] Sonneville-Aubrun, O.; Simonnet, J.-T.; L'Alloret, F. *Adv. Colloid Interface Sci.* **2004**, *108–109*, 145–149.

[83] Porras, M.; Solans, C.; Gonzáles, C.; Martíez, A.; Guinart, A.; Guiérrez, J. M. *Colloid Surf., A* **2004**, *249*, 115–118.

[84] Sadurní, N.; Solans, C.; Azemar, N.; García-Celma, M. J. *Eur. J. Pharm. Sci.* **2005**, *26*, 438–445.

[85] Usón, N.; Garcia, M. J.; Solans, C. *Colloid Surf., A* **2004**, *250*, 415–421.

[86] Shinoda, K.; Saito, J. *J. Colloid Interface Sci.* **1968**, *26*, 70–74.

[87] Izquierdo, P.; Feng, J.; Esquena, J.; Tadros, T. F.; Dederen, J. C.; Garcia, M. J.; Azemar, N.; Solans, C. *J. Colloid Interface Sci.* **2005**, *285*, 388–394.

[88] Hoar, T. P.; Schulman, J. H. *Nature* **1943**, *152*, 102–103.

[89] Schulman, J. H.; Stoeckenius, W.; Prince, L. M. *J. Phys. Chem.* **1959**, *63*, 1677–1680.

[90] Danielsson, I.; Lindman, B. *Colloid Surf.* **1981**, *3*, 391–392.

[91] Paul, B. K.; Moulik, S. P. *J. Dispersion Sci. Technol.* **1997**, *18*, 301–367.

[92] Prince, L. M., Ed. *Microemulsions: Theory and Practice*; Academic Press, 1977.

[93] Guo, R. *J. Dispersion Sci. Technol.* **1995**, *16*, 373–390.

[94] Rees, G. D.; Robinson, B. H. *Adv. Mater.* **1993**, *5*, 608–619.

[95] Paul, B. K.; Moulik, S. P. *Curr. Sci.* **2001**, *80*, 990–1001.

[96] Lawrence, M. J.; Rees, G. D. *Adv. Drug Delivery Rev.* **2000**, *45*, 89–121.

[97] Fanun, M. *Colloid Polym. Sci.* **2009**, *287*, 899–910.

[98] von Corswant, C.; Engstrm, S.; Söderman, O. *Langmuir* **1997**, *13*, 5061–5070.

[99] von Corswant, C.; Söderman, O. *Langmuir* **1998**, *14*, 3506–3511.

[100] Garti, N.; Clement, V.; Fanun, M.; Leser, M. E. *J. Agri. Food. Chem.* **2000**, *48*, 3945–3956.

[101] Kunz, W. *Curr. Opin. Colloid Interface Sci.* **2010**, *15*, 34–39.

[102] Korolev, N.; Lyubartsev, A. P.; Rupprecht, A.; Nordenskiöld, L. *Biophys. J.* **1999**, *77*, 2736–2749.

[103] Lybrand, T. P.; McCammon, J. A.; Wipff, G. *Proc. Natl. Acad. Sci.* **1986**, *83*, 833–835.

[104] Jordan, P. C. *Biophys. J.* **1990**, *58*, 1133–1156.

[105] Kropman, M. F. *Science* **2001**, *291*, 2118–2120.

[106] Leontidis, E. *Curr. Opin. Colloid Interface Sci.* **2002**, *7*, 81–91.

[107] Ataman, M. *Colloid Polym. Sci.* **1987**, *265*, 19–25.

[108] Florin, E.; Kjellander, R.; Eriksson, J. C. *J. Chem. Soc., Faraday Trans. 1* **1984**, *80*, 2889–2910.

[109] Holtzscherer, C.; Candau, F. *J. Colloid Interface Sci.* **1988**, *125*, 97–110.

[110] Carale, T. R.; Pham, Q. T.; Blankschtein, D. *Langmuir* **1994**, *10*, 109–121.

[111] Patel, K.; Bharatiya, B.; Kadam, Y.; Bahadur, P. *J. Surfactants Deterg.* **2010**, *13*, 89–95.

[112] Vlachy, N.; Drechsler, M.; Verbavatz, J.-M.; Touraud, D.; Kunz, W. *J. Colloid Interface Sci.* **2008**, *319*, 542–548.

[113] Kunz, W., Ed. *Specific Ion Effects*; World Scientific Publishing Co. Pte. Ltd., 2010.

[114] Hofmeister, F. *Arch. Exptl. Pathol. Pharmakol.* **1888**, *24*, 247–260.

[115] Kunz, W.; Henle, J.; Ninham, B. W. *Curr. Opin. Colloid Interface Sci.* **2004**, *9*, 19–37.

[116] Collins, K. D. *Methods* **2004**, *34*, 300–311.

[117] Collins, K. D. *Biophys. Chem.* **2006**, *119*, 271–281.

[118] Vlachy, N.; Jagoda-Cwiklik, B.; Vcha, R.; Touraud, D.; Jungwirth, P.; Kunz, W. *Adv. Colloid Interface Sci.* **2009**, *146*, 42–47.

[119] Schwierz, N.; Horinek, D.; Netz, R. *Langmuir* **2010**, *26*, 7370–7379.

[120] Jungwirth, P.; Winter, B. *Annu. Rev. Phys. Chem.* **2008**, *59*, 343–366.

[121] Murphy, D. B., Ed. *Fundamentals of Light Microscopy and Electronic Imaging*; Wiley-Liss. Inc., 2001.

[122] Lawrence, A. S. C. *Mol. Cryst. Liq. Cryst.* **1969**, *7*, 1–57.

[123] Egerton, R. F., Ed. *Physical Principles of Electron Microscopy*; Springer Science+Business Media, Inc., 2005.

[124] Bozzola, J. J., Russell, L. D., Eds. *Electron Microscopy 2nd edition*; Jones and Bartlett Publishers, Inc., 1999.

[125] Miller, D. D.; Bellare, J. R.; Evans, D. F.; Talmon, Y.; Ninham, B. W. *J. Phys. Chem.* **1987**, *91*, 674–685.

[126] Ponsinet, V.; Talmon, Y. *Langmuir* **1997**, *13*, 7287–7292.

[127] Saibil, H. R. *Acta Cryst. D* **2000**, *56*, 1215–1222.

[128] Lin, Z.; Davis, H. T.; Scriven, L. E. *Langmuir* **1996**, *12*, 5489–5493.

[129] J., U.; Yamada, E. *J. Electron Microsc.* **1980**, *29*, 376–382.

[130] Jahn, W.; Strey, R. *J. Phys. Chem.* **1988**, *92*, 2294–2301.

[131] Lindner, P., Zemb, T., Eds. *Neutrons, X-Ray and Light. Scattering Methods Applied to Soft Condensed Matter*; Elsevier Science B. V., Amsterdam, 2002.

[132] Borsali, R., Pecora, R., Eds. *Soft Matter Characterization*; Springer Science+Business Media, LLC, 2008.

[133] Brown, W., Ed. *Light Scattering: Principles and Development*; Oxford University Press inc., New York, 1996.

[134] Lehner, D.; Kellner, G.; Schnablegger, H.; Glatter, O. *J. Colloid Interface Sci.* **1998**, *201*, 34–47.

[135] Shioi, A.; Harada, M.; Tanabe, M. *J. Phys. Chem.* **1995**, *99*, 4750–4756.

[136] Bergström, L. M.; Bastardo, L. A.; Garamus, V. M. *J. Phys. Chem.* **2005**, *109*, 12387–12393.

[137] Finsey, R. *Adv. Colloid Interface Sci.* **1994**, *52*, 79–143.

[138] Wagner, J.; Hrtl, W.; Hempelmann, R. *Langmuir* **2000**, *16*, 4080–4085.

[139] Bernheim-Groswasser, A.; Wachtel, E.; Y., T. *Langmuir* **2000**, *16*, 4131–4140.

[140] Glatter, O., Kratky, O., Eds. *Small Angle X-Ray Scattering*; Academic Press Inc., London Ltd., 1982.

[141] Dianoux, A.-J., Lander, G., Eds. *Neutron Data Booklet*; Institute Laue-Langevin, Neutrons for Science, 2001.

[142] Zech, O.; Bauduin, P.; Palatzky, P.; Touraud, D.; Kunz, W. *Energy Environ. Sci.* **2010**, *3*, 846–851.

[143] Fanun, M. *J. Dispersion Sci. Technol.* **2009**, *30*, 115–123.

[144] Tabor, R. F.; Eastoe, J.; Grillo, I. *Soft Matter* **2009**, *5*, 2125–2129.

[145] Luzzati, V. In *Biological Membranes*; Chapman, D., Ed.; Academic Press: London and New York, 1968.

[146] Freiberger, N.; Glatter, O. *J. Phys. Chem.* **2006**, *110*, 14719–14727.

[147] Rabi, I. I.; Zacharias, J. R.; Millman, S.; Kusch, P. *Physical Reviews* **1938**, *53*, 318.

[148] Webb, G. A., Ed. *Nuclear Magnetic Resonance Vol. 34*; The Royal Society of Chemistry, 2005.

[149] Jacobsen, N. E., Ed. *NMR Spectroscopy Explained*; John Wiley & Sons Inc., New Jersey, 2007.

[150] Weast, R. C., Ed. *Handbook of Chemistry and Physics*; CRC Press, Inc., 1974.

[151] Johannson, A.; Lindman, B. In *Liquid Crystals and Plastic Crystals, Vol. 2.*; Gray, G. W., Winsor, P. A., Eds.; Ellis Harwood, Chichester, 1974.

[152] Tiddy, G. J. T.; Walsh, M. F.; Wyn-Jones, E. *J. Chem. Soc., Faraday Trans. 1* **1982**, *78*, 389–401.

[153] Wennerström, H.; Lindblom, G.; Lindman, B. *Chem. Scr.* **1974**, *6*, 97.

[154] Tiddy, G. J. T.; Lindblom, G.; Lindman, B. *J. Chem. Soc., Faraday Trans. 1* **1978**, *74*, 1290–1300.

[155] Lindblom, G.; Lindman, B.; Tiddy, G. J. T. *J. Am. Chem. Soc.* **1978**, *100*, 2299–2903.

[156] Leigh, I. D.; McDonald, M. P.; Wood, R. M.; Tiddy, G. J. T.; Trevethan, M. A. *J. Chem. Soc., Faraday Trans. 1* **1981**, *77*, 2867–2876.

[157] Rendall, K.; Tiddy, G. J. T.; Trevethan, M. A. *J. Chem. Soc., Faraday Trans. 1* **1983**, *79*, 637–649.

[158] Rendall, K.; Tiddy, G. J. T. *J. Chem. Soc., Faraday Trans. 1* **1984**, *80*, 3339–3357.

[159] Huang, T. C.; Toraya, H.; Blanton, T. N.; Wu, Y. *J. Appl. Cryst.* **1993**, *23*, 180–184.

[160] Blanton, T. N.; Barnes, C. L.; Lelental, M. *J. Appl. Cryst.* **2000**, *33*, 17–173.

[161] Rogers, J.; Winsor, P. A. *J. Colloid Interface Sci.* **1969**, *30*, 247–257.

[162] Cui, X.; Mao, S.; Liu, M.; Yuan, H.; Du, Y. *Langmuir* **2008**, *24*, 10771–10775.

[163] Staples, E. J.; Tiddy, G. J. T. *J. Chem. Soc., Faraday Trans. 1* **1978**, *74*, 2530–2541.

[164] Mely, B.; Charvolin, J.; Keller, P. *Chem. Phys. Lipids* **1975**, *15*, 161–173.

[165] Wärnheim, T.; Henriksson, U.; Malmvik, A.-C.; Bergenstahl, B. *Liq. Cryst.* **1988**, *3*, 791–795.

[166] Schindler, H.; Seelig, J. *J. Biochemistry* **1975**, *14*, 2283–2287.

[167] Böttcher, C. J. F., Brodewijk, P., Eds. *Theory of Electric Polarization, Vol. 2.*; Elsevier, Amsterdam, 1978.

[168] Knight, P.; Wyn-Jones, E.; Tiddy, G. J. T. *J. Phys. Chem.* **1985**, *89*, 3447–3449.

[169] Small, D. M. *Pure Appl. Chem.* **1981**, *53*, 2095–2103.

[170] Tanford, C. *J. Phys. Chem.* **1972**, *76*, 3020 3024.

[171] Silva, P.; Mauro, A.; Mansur, C. *Journal of Applied polymer Science* **2009**, *113*, 392–399.

[172] Lim, H.; Kassim, A.; Huang, N.; Yarmo, M. A. *J. Surfactants Deterg.* **2009**, *12*, 355–362.

[173] Carvell, M.; Hall, D. G.; Lyle, I. G.; Tiddy, G. J. T. *Faraday Discuss. Chem. Soc.* **1986**, *81*, 223–237.

[174] Funari, S. S.; Holmes, M. C.; Tiddy, G. J. T. *J. Phys. Chem.* **1992**, *96*, 11029–11038.

[175] Wilson, A. J. C., Ed. *International Tables for Crystallography, Vol. C*; Kluwer Academic Publishers, Dordrecht, Netherlands, 1992.

[176] Epps, T. H.; Cochran, E. W.; Bailey, T. S.; Waletzko, R. S.; Hardy, C. M.; Bates, F. S. *Macromolecules* **2004**, *37*, 8325–8341.

[177] Piotto, S. *Origins Life Evol. B* **2004**, *34*, 123–132.

[178] Yang, H.; Erford, K.; Kiserow, D. J.; McGown, L. B. *J. Colloid Interface Sci.* **2003**, *262*, 531–535.

[179] Alexandridis, P.; Andersson, K. *J. Phys. Chem. B* **1997**, *101*, 8103–8111.

[180] Kékicheff, P.; Grabielle-Madelmont, C.; Ollivon, M. *J. Colloid Interface Sci.* **1989**, *131*, 112–132.

[181] Kékicheff, P. *J. Colloid Interface Sci.* **1989**, *131*, 133–152.

[182] Richards, C.; Tiddy, G. J. T.; Casey, S. *Langmuir* **2007**, *23*, 467–474.

[183] von Rybinski, W.; Hill, K. *Angew. Chem. Int. Ed.* **1998**, *37*, 1328–1345.

[184] Gelbart, W. M.; McMullen, W. E.; Masters, A.; Ben-Shaul, A. *Langmuir* **1985**, *1*, 101–103.

[185] Kozlov, M. M.; Helfrich, W. *Langmuir* **1992**, *8*, 2792–2797.

[186] Zana, R. *Adv. Colloid Interface Sci.* **1995**, *57*, 1–64.

[187] Bauduin, P.; Renoncourt, A.; Kopf, A.; Touraud, D.; Kunz, W. *Langmuir* **2005**, *21*, 6769–6775.

[188] Bauduin, P.; Wattebled, L.; Touraud, D.; Kunz, W. *Z. Phys. Chem.* **2004**, *21*, 631641.

[189] Friberg, S.; Solans, C. *J. Colloid Interface Sci.* **1978**, *66*, 367–368.

[190] Wadle, A.; Förster, T.; von Rybinski, W. *Colloid Surf., A* **1993**, *76*, 51–57.

[191] Morales, D.; Gutiérrez, J. M.; García-Celma, M. J.; Solans, Y. C. *Langmuir* **2003**, *19*, 7196–7200.

[192] Izquierdo, P.; Esquena, J.; Tadros, T. F.; Dederen, J. C.; Feng, J.; Garcia-Celma, M. J.; Azemar, N.; Solans, C. *Langmuir* **2004**, *20*, 6594–6598.

[193] Arpornpong, N.; Charoensaeng, A.; Sabatini, D. A.; Khaodhiar, S. *J. Surfact. Deterg.* **2010**, *13*, 305–311.

Regensburg, den 02.02.2011

Angelika Klaus